UNIVERSITY OF LONDON THESIS

Degree PhD Year 2008 Name of Author ARVANTIS, Costas D.

This thesis comes within category D.

☑ This copy has been deposited in the Library of University College London

☐ This copy has been deposited in the Senate House Library, Senate House, Malet Street, London WC1E 7HU.

Errata

Page 5 line 25 instead of "perfusion", read "quantitative contrast enhanced"
Page 17 line 9 add "blood" before the flow
Page 17 line 22 instead of "along with" add "with emphasis on"
Page 18 line 23 instead of "beast" read "breast"
Page 19 line 213 instead of "conventionally" read "conventional"
Page 18 line 23 instead of "beast" read "breast"
Page 22 line 3 instead of "transmits" read "transmission"
Page 18 Eq. 1.3 do not read the term (E) in the denominator
Page 29 line 5 instead of "bellow" read "below"
Page 30 line 11 instead of "Eq 1.4" read "Eq 1.5"
Page 34 line 21 instead of "scinillator" read "scintillator"
Page 39 line 8 instead of "perfusion" read "quantitative contrast enhanced"
Page 39 line 12 instead of "200 um" read "200 μm"
Page 39 line 14 instead of "perfusion" read "quantitative contrast enhanced"
Page 39 line 14 instead of "perfusion" read "quantitative contrast enhanced"
Page 46 line 16 instead of "W Zhao" read "Zhao W"
Page 47 line 2 instead of "should be" read "should have been"
Page 47 line 10 instead of "in CsI:Tl" read "such as CsI:Tl"
Page 48 line 10 instead of "is" read "can be"
Page 51 line 3 instead of "Sift" read "shift"
Page 47 line 10 instead of "in CsI:Tl" read "such as CsI:Tl"
Page 53 line 13 Eq. 3.1 instead of "FT" read "T"
Page 61 line 10 instead of "cut-of" read "cut-off"
Page 66 line 2 instead of "ergotic" read "ergodic"
Page 53 line 13 Eq. 3.27 remove the bar from the "σ"
Page 53 line 13 Eq. 3.28 read "α_n" instead of "α_q"
Page 70 line 7 instead of "add" read "adds"
Page 73 line 7 instead of "dark current transfer" read "dark current curve"
Page 93 line 13 instead of "there any" read "there are any"
Page 97 line 3 instead of "scinillator" read "scintillator"
Page 107 Figure 4.27 instead of "slop" read "slope"
Page 108 Figure 4.28 x-axis instead of "frequancy" read "frequency"
Page 112 line 5 instead of "Figure 3.44" read "Figure 3.43"
Page 113 line 9 instead of "flour" read "floor"
Page 114 line 19 instead of "worthy a" read "is worthy of"
Page 126 line 19 instead of "perfusion" read "contrast enhanced"
Page 131 line 8 instead of "perfusion" read "quantitative contrast enhanced"
Page 131 line 12 do not read "not"
Page 135 line 6 instead of "ad" read "and"
Page 114 line 19 do not read "with the of"
Page 147 line 18 instead of "20%" read "18%"
Page 148line 10 instead of "10^{3}" read "10^{-3}"
Page 157 line 21 instead of "m/cm^2" read "mg/cm^2"
Page 159 line 16 instead of "up-take" read "responce"
Page 162 line 3 instead of "perfusion" read "quantitative contrast enhanced"

Quantitative contrast enhanced mammography and evaluation of scientific CMOS active pixels sensors for medical imaging

By

COSTAS D. ARVANITIS

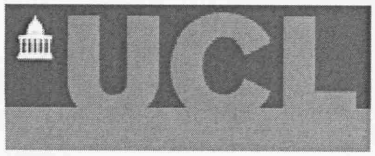

A THESIS SUBMITTED TO THE UNIVERSITY OF LONDON
FOR THE DEGREE OF DOCTOR OF PHILOSOPHY

DEPARTMENT OF MEDICAL PHYSICS AND BIOENGINEERING
UNIVERSITY COLLEGE LONDON

ProQuest LLC
789 East Eisenhower Parkway
P.O. Box 1346
Ann Arbor, MI 48106-1346

I Costas Arvanitis confirm that the work presented in this thesis is my own. Where information has been derived from other sources, I confirm that this has been indicated in the thesis

Signature……..

Abstract

Quantitative contrast enhanced mammography based on a dual energy approach aims to extract quantitative and temporal information of the tumour enhancement after administration of vascular contrast media. This information can be used to indirectly measure the tumour microvessel density and the blood flow of abnormally "leaky" breast tumours. A theoretical framework and optimisation of critical parameters essential for the development of quantitative contrast enhanced mammography is presented here. Using the dual energy approach, measurement of iodine projected thickness can be performed. Temporal variations in the measured thickness can be effectively used to measure the kinetics of the contrast medium using an experimental phantom.

For the extraction of the temporal information a limited number of low dose images (~0.2 mGy) are required in order to keep the patient dose at the same levels as conventional mammography. At the exposure levels currently available, active matrix flat panel imagers (AMFPIs) are limited. A novel active pixel flat panel imager (APFPIs) based on scientific complementary metal oxide semiconductor (CMOS) active pixel sensor (APS) can potentially realise a high performance detector that suits this application. A thorough description of the electro-optical performance of two CMOS APS and the signal and noise properties of these imagers is also presented in this study. The signal and noise properties of the X-ray imagers has been quantified in the mammographic energy range using the modulation transfer function (MTF), the noise power spectra (NPS) and the detective quantum efficiency (DQE). The resulting X-ray imagers offer high sensitivity, low noise, and comparable resolution (MTF=0.1 at 9.5 cycles/mm) with respect to other digital mammographic units. The combined outcome of the above performance resulted in a quantum limited detector at 0.23 μC/kg detector entrance exposure with DQE, at zero frequency equal to 0.5 (DQE (0)=0.50).

The development of quantitative contrast enhanced mammography has been experimentally evaluated here, using a currently available amorphous silicon based active matrix flat panel imager (AMFPIs), which was used as a reference detector, and the active pixel flat panel imager (APFPIs) based on CMOS technology, which had the best performance from those evaluated. The quantitative contrast enhanced

mammography has been optimised using analytical simulations. The results suggest that active pixel flat panel imagers can be used for the development of quantitative contrast enhanced mammography, although higher pixel sizes and elimination of fixed pattern noise appeared to be very important for the accurate measurement of the projected thickness. The presence of scattered radiation is the only factor that degrades the measurement of the iodine projected thickness and should be removed effectively before any analysis of the energy pair images.

Contents

Chapter 3

Detector performance and image quality metrics

Chapter 4

Electro-optical and X-ray performance evaluation of the imager

Chapter 5

Development of quantitative contrast enhanced mammography

Chapter 6

System integration and consideration of its clinical potential

Acknowledgements

I wish to express my appreciation to Professor Robert Speller for his support and for giving me valuable advice over the course of this project, without which this study would not have been completed.

My gratitude goes to Dr Gary Royle for his suggestions and instructions, let alone his excellent sense humour which was a catalyst in many situations. I would also like to thank my colleague Sarah Bohindiek; working with her during the last two years of my PhD has been more than enjoyable and helpful. My gratitude goes also to Dr Alessandro Olivo for the endless stimulating scientific discussions.

Special thanks go to Dr Helen Southwood for her contribution to the final appearance of this work and for helping me to improve my English language skills. I am also grateful to Toshiki Nishibayashi for providing me with information and hints while solving various technical problems associated with digital detectors especially during the first period of my PhD. Many thanks to Dr Silvia Pani and Dr Christian Venanzi for their help in IDL language. I would also like to thank Dr Renato Turcheta for helping me understand the characterization techniques and his invaluable comments regarding the CMOS APS.

I am particularly indebted to Dr. Marinos Metaxas for his warm welcome to the radiation physics group from the very first moment. My very special thanks go to Petros Marinos for his true friendship and support in numerous difficulties associated with everyday life in London.

I am also thankful to the Greek State Scholarships Foundation for providing me with the Scholarship and to the RC-UK Basic Technology Multidimensional Integrated Intelligent Imaging (MI-3) programme for providing me with the opportunity to develop my professional career and the members of the consortium for their support and collaboration.

Most importantly, I want to deeply thank my parents for their continuous support and love.

List of publications

C. D. Arvanitis, S. E. Bohndiek, G. Royle, A. Blue, H. X. Liang, A. Clark, M. Prydderch, R. Turchetta and R. Speller "Empirical electro-optical and X-ray performance evaluation of CMOS active pixels sensor for low dose, high resolution X-ray imaging" accepted Medical Physics (accepted 2007).

C. D. Arvanitis, G. Royle, and R. Speller "Dual energy contrast enhanced breast imaging optimization using contrast to noise ratio" SPIE Medical Imaging pp. 65102Y (Feb. 2007).

S. Bohndiek, C. D. Arvanitis, G. Segneri, C. Venanzi, G. Royle, A. Clark, J. Crooks, R. Halsall, M. Key-Charriere, S. Martin, M. Prydderch, R. Turchetta, A. Blue, V. O'Shea and R. Speller "Optical and X-ray Characterization of Two Novel CMOS Image Sensors" SPIE Photonics West OPTO pp. 647113 (Jan. 2007).

C. D. Arvanitis, S. Bohndiek, G. Segneri, C. Venanzi, G. Royle, A. Clark, J. Crooks, R. Halsall, M. Key-Charriere, S. Martin, M. Prydderch, R. Turchetta and R. Speller "A Novel Active Pixel Sensor With On-Pixel Analog-to-Digital Converter for Mammography" IEEE MIC pp. 3576-3580 (Oct. 2006).

List of figures

Chapter 1

Chapter 2

Chapter 3

Chapter 4

Chapter 5

List of Tables

Chapter 2

Chapter 3

Chapter 4

Chapter 5

Chapter 1

Introduction

Medical imaging can be looked at from two different perspectives, the medical and the physical. The medical point of view is application-driven and involves finding the best way of tackling a medical problem through imaging, i.e. either to answer a diagnostic question, or to facilitate a therapy. The requirements depend on the medical problem: which organs have to be imaged, which details have to be made visible, the size of the part of the body to be visualized, how to deal with the problem of motion if any, and so forth. Additional functional information such as perfusion or flow rate can be combined with anatomical information into one image so as to enrich the image content. The physical point of view is technology-driven. Feasibility is determined by the existing radiation sources, the materials and detectors available for absorbing and converting the radiation used, and the computing power required to process and, where applicable, to acquire or reconstruct data in real-time.

In this work, the interest from the medical point of view is in examining whether it is feasible to extract prognostic and diagnostic information related with the process of breast tumour formation and growth by indirectly measuring breast tumour neovascularization (formation of new vessels) using vascular contrast agents. From the physical point of view the aim is to investigate if the recent technological advances in CMOS active pixel sensors can help to increase the efficacy of conventional mammography and facilitate the development of advanced mammographic approaches. The state of mammography is reviewed below along with recent findings that suggest that mammography requires further developments.

In the past few decades conventional screen film combinations (Sabel M. *et al* 1996) and more recently digital mammography (Lewin J M. *et al* 2002) have been utilized for the detection of breast tumours. Although, mammography has superior performance as compared with other modalities (US, MRI, etc) it has some shortfalls, such as low resolution (Yaffe M J *et al* 2000), poor visualization of dense breasts (Nunes F L S *et al* 2002) and many repeated examinations (Sabel M *et al* 1996). Those limits diminish its

effectiveness when tumour size is small (< 4 mm), and in dense breasts. Additionally, it does not provide adequate information for tissue characterization such as differentiation between benign and malignant tumours resulting in an increased number of false biopsies. There is an anticipation that some of the above limitations of mammography can be compensated for with the introduction of new digital detectors with improved signal and noise transfer properties. However, the small difference in the attenuation coefficients of breast tumours, glandular and adipose tissue (Johns P C *et al* 1987) sets a fundamental limit on the visualisation of breast tumours. Thus, new or advanced imaging approaches are necessary in order to enhance the visibility of tumours in the breast cluttered background.

Some of the advanced imaging approaches proposed so far include dual energy imaging for microcalcifications detection (Kappadath S C *et al* 2003), breast tomosynthesis (Wu T *et al* 2003), and breast CT (Boone J M *et al* 2001 and Chen B *et al* 2002). All the above approaches are trying to utilise the small differences in attenuation coefficients mentioned above. An emerging advanced imaging approach which has demonstrated encouraging results in the detection of breast tumours is contrast enhanced breast imaging. Additionally, this imaging approach can help with monitoring new therapeutic options that attempt to confine tumour *angiogenesis*. There is speculation that the isolation of breast tumour enhanced signals will assist to increase the effectiveness of cancer treatment and possibly support the development of personalized medicine.

Breast tumour *angiogenesis* describes the formation of new blood vessels within tumours as a result of genetic mutations within the tumour cell (Folkman J *et al* 1987 and Folkman J e*t al* 1989). Beast tumour microvessel density (on average 80 microvessels per square millimetre Dromain C *et al* 2006) is associated with an increase in blood flow or perfusion (Omar W S *et al* 1997). Thus the formation of new microvessels can be monitored by the use of vascular contrast agents as the strength of the enhancement, associated with the pixel (or voxel) value, can describe the extent of the neovascularization. Spatial and temporal measurements of the vascular contrast agent can help to overcome some of the limitations of conventional mammography.

Both breast MR imaging and digital X-ray mammography have been used for the isolation of contrast medium enhanced signal. Using either modality it has been shown

that prognostic and diagnostic information about breast tumour growth and formation can be provided. Neither imaging approach has achieved optimum performance. However, the assessment of the maximum intensity of the enhancement, the grade of uptake and wash out (Kuhl C K *et al* 2000) of those agents, are used in MR imaging to differentiate between benign and malignant tumours. A rapid uptake and wash-out of the contrast agent is considered to be a strong indicator of malignancy. "Rim-like" enhancement, tumour morphological features and sometimes repeat examinations, are employed to reduce false negative decisions (Boets C *et al* 1994 and Kuhl C K *et al* 2000)

In X-ray breast imaging, early studies using computed tomography (Chang C H J *et al* 1981) and digital subtraction angiography (Watt C *et al* 1985) systems showed that identification of tumours in dense breasts and the differentiation between benign and malignant tumours respectively is possible after administration of iodinated vascular contrast agents. However, the diagnostic accuracy of those approaches was insufficient, primarily due to limitations of the systems used at that time and the resulting high patient dose. The improved sensitivity of currently available full field digital mammography systems (Pisano E T *et al* 2005) has led to the renewed interest of performing iodine based contrast enhanced mammography. Recent studies employing temporal subtraction (Jong R A *et al* 2003, and Dromain C *et al* 2006) and dual energy techniques (Lewin J M *et al* 2003) have shown ~83% specificity, while the acquisition parameters in the latter were not optimum. This score of specificity is well above the ~74% currently available from conventionally mammography (Pisano E D *et al* 2005).

The above studies and MR studies in particular, have shown that both contrast agent kinetics measurements and visualization of tumour morphology are crucial. This is because tumour enhancement varies to a great extent among different tumour types and in particular for ductal carcinoma in situ (DCIS) and invasive ductal carcinoma where it may be below any reasonable enhancement thresholds. Thus optimization in the acquisition parameters and the associated trade-offs with temporal and spatial resolution is needed.

Both MR and X-ray breast imaging have discrete advantages and limitations and it is still unclear which of the above modalities will be able to perform contrast enhanced measurements most efficiently. The main advantage of MR breast imaging is that it does

not use ionising radiation and the three dimensional (3-D) information provided, facilitates the assessment of tumour enhancement without being obscured by super-imposed breast tissue structures. However, the high cost and the limited access to MR machines are important limitations for its widespread availability. In addition, a compromise between spatial and temporal resolution is inevitable in MR imaging, potentially increasing the number of repeated examinations.

On the contrary, in X-ray breast imaging, apart from the wide spread availability of the flat panel imagers, high resolution and high frame rates are readily available. Assessment of tumour enhancement can be performed by projecting the 3-D distribution of iodine onto the 2-D detector plane. Isolation of the iodine and measurement of its projected thickness can be accomplished by employing dual energy imaging approaches. Although the temporal subtraction approach in principle can be used with the same efficacy, high patient motion artifacts during the examination make it very difficult to effectively isolate the iodine from breast cluttered background and hence the assessment of the contrast medium kinetics. This is not a limitation in a dual energy approach since the acquisition in rapid sequence of the low- and high- energy images, while the breast is compressed, is used for the isolation of iodine, leading to the elimination of patient motion artifacts. The temporal variation in the iodine projected thickness can be effectively used to measure the kinetics of contrast agent in the breast tumour. Quantitative contrast enhanced mammography aims for a transformation of the conventional mammography from a qualitative imaging approach (with image quality as the key quality parameter) into a flexible quantitative imaging technique, allowing automated procedures for calibrated, reproducible measurements (with accuracy and precision as key quality parameters). In order to achieve the above goal theoretical analysis, optimized conditions and practical aspects regarding its implementation under clinical conditions will be provided.

In the recent past dual energy imaging has been applied in the breast (Kappadath S.C *et al* 2003) and conventional digital mammography units have been modified to accommodate the requirements of this technique. However, until now it has been used for imaging static structures and in particular for the isolation of tumours and microcalcifications in the breast. Although the currently available full field digital

mammography systems can be used for this purpose in similar manner, there are some significant shortfalls of this detector technology that have the potential to undermine the development of quantitative contrast enhanced mammography.

In particular, in dynamic studies, such as contrast enhanced mammography, a number of frames have to be acquired, limiting the exposure per frame to a fraction of the standard mammographic exposure. This level of exposure approaches fluoroscopic operation where the detection quantum efficiency of active matrix flat panel imagers (AMFPIs) is limited (Zhao W *et al* 1997 and Antonuk L E *et al* 2000). In addition AMFPIs at high frame rates show an excess of read noise (Jee K-W *et al* 2003), detector image lag, ghosting and baseline drifts (Siewerdsen J H *et al* 1999 and Bloomquist A K *et al* 2006). Elimination of detector image lag, ghosting and baseline drifts are crucial in order to extract quantitative information from the series of images. Furthermore, the need to keep the patient dose at the same levels as conventional mammography pushes for high detector quantum efficiency at higher energies. For indirect detection, increased sensitivity in the blue region of the visible spectrum is important for good spectral matching with high light yield scintillators, while maintaining low read noise for good signal to noise ratio are essential.

For the wide spread availability of this imaging approach it is very important to keep the digital system cost low. Thus a detector that will be able to incorporate different modes of operation and satisfy the requirements of both conventional and quantitative contrast enhanced mammography should be considered.

In conventional digital mammography, recent studies indicate (Yamada T *et al* 2003) that the detection and characterisation of microcalcifications can be improved with smaller effective pixel sizes than 70-100 μm that is currently available. Although the results are not conclusive, there is a need to examine the performance of full field digital detectors with pixel size of 50 μm and below. AMFPIs at pixel sizes below 70 μm are very difficult to build since the high additive electronic noise and the small fill factor reduce the signal to noise ratio below levels essential for the detection of fine details on the mammogram. Recently, a high resolution X-ray imager for digital mammography (Suryanarayanan S *et al* 2005) based on a CCD developed for crystallography has been proposed. For X-ray imaging, CCDs are susceptible to radiation damage (Janesick J *et al*

2001) but a thick demagnification fiber optic taper (FOT) can be used to eliminate the direct hits on the detector. However, the light propagated through the demagnification FOT requires specific light propagation conditions as transmits through the FOT increases the quantum sink (Williams M B *et al* 1999).In addition, CCDs are serial devices, which means that all the charge has to pass through the same sense node before read out. For large area formats this limits the frame rate of the sensor since for higher readout speeds the noise in CCDs becomes unacceptably high (Janesick J *et al* 2002). This limitation causes a bottleneck in large area CCD detectors, possibly restricting these devices to static imaging in order to maintain low read out noise.

Although in recent years significant progress has been made in a-Si detectors (El-Mohri Y *et al* 2006) and in other technologies (Bloomquist A K *et al* 2006), the challenge for researchers is to offer a digital detector that fills the needs that are not covered by existing technology.

The recent advances in the performance of monolithic complementary metal oxide semiconductor (CMOS) active pixel sensors (APS) have the potential to bring this technology to the forefront of diagnostic radiology. CMOS image sensors benefit from a high level of integration due to the fact that they are fabricated in a standard CMOS process. CMOS active pixel sensors offer very fast image acquisition due to column parallel read out (Fossum E R *et al* 1997 and Krymski A I *et al* 2003). At high speed, the noise level is better than for CCD image sensors (Janesick J *et al* 2002). Increased sensitivity in the blue part of the spectrum (Lulé T *et al* 2000) and higher fill factor for constant pixel size (Wong H *et al* 2000) can be achieved as CMOS technology shrinks. Radiation tolerant sensors have already been presented (Said E S *et al* 2001, Bogaerts J *et al* 2003 and Velthuis J J 2005) and large sensors (Meynants G *et al* 2003), up to 8 inch wafer scale (Scheffer D *et al* 2007), can today be produced by using 'stitching', a technique that allows creating seamless devices, which are larger than the CMOS process reticle, i.e. about 2cmx2cm.

Full field digital mammography and quantitative contrast enhanced mammography can benefit directly from the currently available technology of CMOS active pixel sensors. For X-ray detection CMOS APS can optically coupled with phosphors to form a high performance indirect X-ray imager. The resultant X-ray imagers are named CMOS

active pixel flat panel imagers (APFPIs) in order to emphasize the difference in the read out with active matrix flat panel imagers (AMFPIs) that are currently used in clinical practice. Using this technology we expect to achieve:

a. High sensitivity due high quantum efficiency of the CMOS APS sensor and the good spectral matching with high light yield CsI:Tl phosphors (Van Eijk C W E *et al* 2002).
b. Low noise detector, because active pixel sensors (APS) offer superior noise performance as compared with AMFPIs.
c. Improved resolution with respect to other digital systems, and possibly comparable to screen film mammography, due to the small pixel pitch (25 um x 25 um) of the sensor and the columnar structure of the CsI:Tl phosphor.
d. The combined outcome of the above improvements will result in a quantum limited detector at very low exposures (<0.5 μC/kg) with high detection quantum efficiency.

A thorough description of the electro-optical performance of the CMOS APS and the signal and noise properties of the CMOS APS is presented. In order to fully explore the benefits of this technology three different CMOS APS with different properties were evaluated. The signal and noise properties of the resulted indirect X-ray imagers have been quantified in the mammography energy range using observer-independent performance variables (OIPVs). Such established objective criteria to quantify signal and noise transfer of the imaging system are the modulation transfer function (MTF), the noise power spectra (NPS) and the resultant signal to noise performance from the detective quantum efficiency (DQE).

Dual Energy Imaging

1.1 Overview

In the remainder of this chapter the theoretical framework that describes the properties of dual energy imaging is presented. Within this framework analytical expressions are derived for the isolation of iodinated contrast agents. Quantitative assessment along with the requirements to develop contrast enhanced mammography based on dual energy imaging is given. The effect of scatter radiation in the formation of material selective images is determined analytically. Finally, a description of the methodology developed for the optimisation of critical parameters of dual energy k-edge breast imaging is provided.

1.2 Dual energy k-edge breast imaging

Dual energy imaging, where separate low- and high-energy images permits formation of material selective images, has been used in the past in digital radiography. The principles of dual energy imaging have been extensively discussed in the literature (Alvarez R E and Mascovski A 1976, Brody W R *et al* 1981, Lehman L A *et al* 1981, Johns P C and Jaffe M J 1985, Boone J M *et al* 1990 and Lemacks M R *et al* 2002) along with its practical aspects (Ergun D L *et al* 1990, Brettle D S and Cowen A R 1994 and Kappadath S C and Show C C 2005). In mammography dual energy imaging has been primarily focused on the isolation of microcalcifications in the mammogram as microcalcifications may be obscured by overlapping tissue structures with increased complexity. These structures in mammograms are formed due to the presence of adipose tissue, glandular tissue, ducts, vessels and soft tissue masses in the breast.

It has been shown (Lemacks M R *et al* 2002) that the imaging of a compressed breast could be considered as a two material imaging problem, for example, the calcification thickness and the breast composition expressed as the ratio of adipose to glandular tissue. Estimation of vascular iodinated contrast medium thickness can be achieved in a similar way with two energy beams that straddle the iodine k-edge. The k-edge approach is preferable as it provides a higher resultant iodine contrast compared to non k-edge iodine imaging (Riederer S J *et al* 1981). Recent studies using this approach have been performed using full field digital mammography units (Lewin J M *at al* 2003, Baldelli P

et al 2005 and Carton A-K *et al* 2007); however they were limited either from the hardware of the systems used or the post processing of the images. The lack of optimized conditions was evident in the above studies although reasonable isolation of iodine has been achieved.

For the evaluation of the clinical potential of this technique some certain criteria have to be satisfied. These include: (i) assessment of spectral pair and mean glandular dose (ii) effective isolation of iodinated contrast medium from breast cluttered background, (iii) absolute signal enhancement measurements irrespective of breast composition, breast thickness, photon fluence and modality used, and (iv) vascular contrast medium kinetics measurements. The analytical expressions presented here are used to maximize the discrimination capability of the dual energy breast imaging in the estimation of the iodine projected thicknesses.

Consider two different energy beams one with low (below k-edge of iodine) and one with high (above k-edge of iodine) energy incident on the breast. The low T_b^l and high T_b^h energy image signals per energy fluence absorbed by a detector when the two beams are transmitted through a breast composed of adipose tissue of thickness of t_a, glandular tissue of thickness of t_g, and iodine with thickness of t_i (mg/cm^2) (Fig. 1.1) can be expressed as:

$$T_b^j = \int \frac{\Phi_o^j(E)}{dE} \cdot E \cdot \alpha_{pix}^2 \cdot e^{-\left(\mu_a^j t_a + \mu_g^j t_g + \mu_i^j t_i\right)} \cdot \eta_D(E) \cdot \overline{G}_D(E) \cdot dE, (j = l, h) \quad (1.1)$$

where $\frac{\Phi_o^j(E)}{dE}$ is the photon fluence spectrum, E is the X-ray photon energy α_{pix} is the pixel size assuming 100% fill factor (expressed in mm) $\eta_D(E)$ is the detector quantum efficiency, and $\overline{G}_D(E)$ is the detector mean gain and represents the signal generated per deposited energy on the detector. The mass attenuation coefficients of the adipose tissue, glandular tissue and iodine respectively expressed in cm^2/mg, are given by μ_a, μ_g and μ_i. In the above expression, the image signal was expressed as a function of the absorbed energy fluence explicitly describing the image signal formation for energy integrating

detectors. In order to keep the descriptions in a numerical form uniform illumination, a spatially invariant detector and no scatter radiation reaching the detector, is assumed.

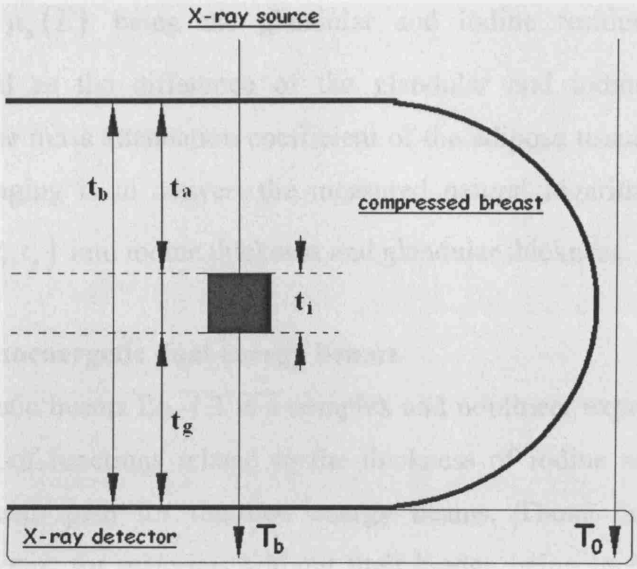

Figure 1.1. A compressed breast of thickness t_b, with a cubic iodinated area of thickness t_i, and adipose and glandular tissues of thickness t_a and t_g respectively.

If the total breast tissue thickness incorporating iodine is $t_b = t_a + t_g + t_i$, the line integral L^j of the attenuation along each beam path weighted by the detector response for the low and high energy beams can be estimated as follows:

$$L^j = \ln\left(\frac{T_0^j}{T_b^j}\right) = \ln\left(\frac{\int \frac{\Phi_o^j(E)}{dE}\cdot E\cdot \alpha_{pix}^2\, \eta_D(E)\cdot \overline{G}_D(E)\,dE}{\int \frac{\Phi_o^j(E)}{dE}\cdot E\cdot \alpha_{pix}^2\cdot e^{-\left(\mu_a^j t_a+\mu_g^j t_g+\mu_i^j t_i\right)}\cdot \eta_D(E)\cdot \overline{G}_D(E)\,dE}\right), (j=l,h) \quad (1.2)$$

The use of the image signals attenuated by 100% adipose tissue for the low and high energy beams respectively reduces the problem of three material compositions to two material compositions (Lemacks M R *et al* 2002). This can be expressed as follows:

$$I_a^j(t_i,t_g) = \frac{L_a^j}{L_b^j} = \ln\left(\frac{\int \frac{\Phi_o^j(E)}{dE}\cdot E\cdot \alpha_{pix}^2\cdot e^{-\left(\mu_a^j(E)t_b\right)}\cdot \eta_D(E)\cdot \overline{G}_D(E)\cdot dE}{\int \frac{\Phi_o^j(E)}{dE}\cdot E\cdot \alpha_{pix}^2\cdot (E) e^{-\left(\mu_a^j t_b\right)} e^{-\left(\Delta\mu_g^j(E)t_g+\Delta\mu_i^j(E)t_i\right)}\cdot \eta_D(E)\cdot \overline{G}_D(E)\cdot dE}\right), (j=l,h) \quad (1.3)$$

where L_b^j and L_a^j are the line integrals of the attenuation along each beam path from breast and adipose tissue only, with $\Delta\mu_g(E)=\mu_g(E)-\mu_a(E)$ and $\Delta\mu_i(E)=\mu_i(E)-\mu_a(E)$ being the glandular and iodine residue mass attenuation coefficient defined as the difference of the glandular and iodine mass attenuation coefficient from the mass attenuation coefficient of the adipose tissue. The goal of dual-energy iodine imaging is to convert the measured natural logarithm signal functions $I^l(t_i,t_g)$ and $I^h(t_i,t_g)$ into iodine thickness and glandular thickness.

1.2.2 Quasi-monoenergetic dual energy beams

For polyenergetic beams Eq. 1.3 is a complex and nonlinear expression that requires the determination of functions related to the thickness of iodine and glandular tissue present in the beam path for the two energy beams. Those functions have been determined in the past for materials without their k-edge being incorporated in energy range of the spectra pair, using either basis decomposition (Lehman L A *et al* 1981) or inverse mapping (Kappadath S C and Show C C 2003) techniques using a variety of nonlinear functions. However, the presence of the iodine k-edge and its resultant sharp discontinuity in the attenuation coefficient, the linear combination of the natural logarithm transformed images provides reasonable accuracy and gives physical insight in the subtraction process. In addition by appropriate filtration of the polychromatic spectra generated with conventional X-ray sources, spectra with relatively small energy variance (~10 keV FWHM) can be obtained eliminating the beam hardening effects. In order to take into account even this small energy variance in the analytical expressions the average mass attenuation coefficients of the three materials has to be used and it can be measured as follows:

$$\bar{\mu}^j=\left(\frac{\int\frac{\Phi_o^j(E)}{dE}\cdot E\cdot\mu(E)\cdot\eta_D(E)\cdot\bar{G}_D(E)\cdot dE}{\int\frac{\Phi_o^j(E)}{dE}\cdot E\,\eta_D(E)\cdot\bar{G}_D(E)\cdot dE}\right)(j=l,h) \qquad (1.4)$$

The average mass attenuation coefficients were weighted by the detector response in order to correct for its non-ideal absorption efficiency. Thus the above expression can be analytically solved to good approximation and Eq. 1.3 reduces to:

$$\bar{I}_a^j = \frac{\bar{L}_a^j}{\bar{L}_b^j} = \overline{\Delta\mu}_g^j t_g + \overline{\Delta\mu}_i^j t_i \left(j = l, h\right) \tag{1.5}$$

Expressing Eq. 1.5 in matrix form we get

$$\begin{pmatrix} \bar{I}_a^l \\ \bar{I}_a^h \end{pmatrix} = \begin{pmatrix} \overline{\Delta\mu}_g^l & \overline{\Delta\mu}_i^l \\ \overline{\Delta\mu}_g^h & \overline{\Delta\mu}_i^h \end{pmatrix} \cdot \begin{pmatrix} t_g \\ t_i \end{pmatrix} \tag{1.6}$$

A linear combination of Eqs. (1.6) produces an iodine image only:

$$\overline{\Delta I}_a = \frac{\bar{L}_a^h}{\bar{L}_b^h} - \frac{\overline{\Delta\mu}_g^h}{\overline{\Delta\mu}_g^l} \cdot \frac{\bar{L}_a^l}{\bar{L}_b^l} = -\left(\frac{\overline{\Delta\mu}_g^h}{\overline{\Delta\mu}_g^l} \overline{\Delta\mu}_i^l - \overline{\Delta\mu}_i^h \right) t_i \tag{1.7}$$

or

$$\overline{\Delta I}_a = \bar{I}_a^h - \beta_g \bar{I}_a^l = \mu_i^{eff} t_i \Leftrightarrow t_i = \frac{\overline{\Delta I}_a}{\mu_i^{eff}} \tag{1.8}$$

where, $\mu_i^{eff} = -\left(\frac{\overline{\Delta\mu}_g^h}{\overline{\Delta\mu}_g^l} \overline{\Delta\mu}_i^l - \overline{\Delta\mu}_i^h \right)$ is defined as the effective mass attenuation coefficient of iodine and $\beta_g = \frac{\overline{\Delta\mu}_g^h}{\overline{\Delta\mu}_g^l}$ is the weighting factor related with the effective suppression of the glandular tissue, and $\overline{\Delta\mu}$ denotes the effective residue mass attenuation coefficients. $\bar{L}_b$ is the natural logarithm of $\bar{T}_b$ which is the transmitted energy fluence absorbed by the detector beneath the breast and can be determined from the low and high energy images. Similarly $\bar{L}_a$ is the natural logarithm of $\bar{T}_a$ which is readily available using a reference image as the thickness of a compressed breast can be measured with high accuracy. The above equation denotes that measurement of the iodine thickness can be achieved irrespective of breast composition, breast thickness and detector material, when the two images are transformed by the natural logarithm and subtracted after proper weighting. Note that the weighting factor is defined by the ratio of the glandular effective residue mass attenuation coefficient for the low and high energy beams, which are energy dependent. From Eq. 1.7 it becomes apparent that the higher the iodine effective mass attenuation coefficient is $\left(\mu_i^{eff}\right)$ the better it is in order to differentiate small changes in the iodine projected thickness. This is very important as it will increase the sensitivity of

the iodine selective imaging providing quantitative information with higher accuracy and therefore will be less prone to observer misinterpretation and errors associated with the linear subtraction. It is evident that the μ_i^{eff} is maximized when the difference of the iodine mass attenuation coefficients in the low- and high-energy spectrum regimes is maximum. Thus two beams with mean energies immediately above and bellow the iodine k-edge can provide the required condition for high accuracy spatio-temporal iodine selective imaging.

1.2.3. Scatter in dual energy imaging

In full field selective imaging scatter radiation in the low- and high-energy images will be present and will provide erroneous measurement of the X-ray attenuation from the imaged materials, limiting the accuracy in the projected thickness measurement (Shaw C-G and Plewes D B 1987, Wagner F C *et al* 1988, Molloi S Y and Mistretta C A. 1988, Ergun D L *et al* 1990, Kappadath S C and Show C C 2005). Ideally, one would like to estimate (or reject) the scatter component in both images and prior to any post processing to subtract it on a pixel-by-pixel basis in order to provide scatter free images. The scatter can be reduced from the image using either rejection (hardware-antiscatter grids) or estimation (software-simulation) methods, or a combination of the two. In the first there is always a significant contamination of scatter radiation (~20%) and in the latter there is always an error associated with estimation process. In both images scatter radiation will have spatial (especially at the breast periphery) and energy dependence. Therefore it is necessary to understand and determine its effect on the final image as it is the most important factor that can potentially limit the accuracy in the iodine projected thickness measurement. In the presence of scatter the Eq. 1.1 can be expressed as follows:

$$T'^{j}_{b}(x,y,E) = T^{j}_{b}(x,y,E) + S^{j}_{b}(x,y,E)(j=l,h) \qquad (1.9)$$

where T' denotes the total signal per energy fluence absorbed by the detector when the two beams are transmitted through the breast and T and S denote the primary and scatter signals per energy fluence absorbed by the detector. x and y denote spatial coordinates and E is energy. The scatter radiation will be different beneath breasts with different compositions and thicknesses and will have different spectral signature at the two

different energies. It has been shown (Aus R J *et al* 1999) that the scattered spectrum with respect to primary spectrum does not change significantly at the energy ranges around the iodine k-edge. Thus to good approximation scatter can be expressed as a function of scatter-to-primary ratio (S/P) and Eq. 1.9 for a given beam path can be rewritten as follows:

$$T'^{j}_{b} = \left(1 + S/P^{j}_{b}\right) T^{j}_{b} \left(j = l, h\right) \tag{1.10}$$

Using similar arguments as above the line integrals of the attenuation along each beam path from breast can be expressed as:

$$L'^{j}_{b} = L^{j}_{b} - \ln\left(1 + S/P^{j}_{b}\right)\left(j = l, h\right) \tag{1.11}$$

Thus by taking into account Eq. 1.11 and using scatter image signals for 100% adipose tissue for the low and high energy beams respectively Eq. 1.4 will be:

$$\bar{I}'^{j}_{a} = \frac{\bar{L}'^{j}_{a} - \ln\left(1 + S/P^{j}_{a}\right)}{\bar{L}'^{j}_{b} - \ln\left(1 + S/P^{j}_{b}\right)} = \overline{\Delta\mu}^{j}_{g} t_g + \overline{\Delta\mu}^{j}_{i} t_i \left(j = l, h\right) \tag{1.12}$$

Linear combination of the above equations for the low and high energy beams will give the iodine projected thickness in the presence of scatter radiation.

$$\bar{I}^{h}_{a} - \beta_g \bar{I}^{l}_{a} = \mu^{eff}_{i} t_i + \ln\left(\frac{1 + S/P^{l}_{a}}{1 + S/P^{l}_{b}}\right)^{\beta_g} - \ln\left(\frac{1 + S/P^{h}_{a}}{1 + S/P^{h}_{b}}\right) \tag{1.13}$$

From Eq. 1.13 and by taking into account Eq. 1.8 a close analytical form describing the effect of scatter radiation in the estimation of iodine projected thickness can be expressed as follows:

$$t'_i = t_i + \ln\left(\frac{1 + S/P^{l}_{a}}{1 + S/P^{l}_{b}}\right)^{\frac{\beta_g}{\mu^{eff}_{i}}} - \ln\left(\frac{1 + S/P^{h}_{a}}{1 + S/P^{h}_{b}}\right)^{\frac{1}{\mu^{eff}_{i}}} \tag{1.14}$$

where t_i is the real iodine thickness and t'_i is the measured iodine thickness in the presence of scatter. From Eq. 1.14 it is evident that scatter radiation will introduce nonlinearities in the estimation of iodine projected thickness that will depend on the scatter-to-primary ratio (S/P) of the detected photons beneath the material to be isolated. The scatter radiation alone has low variation across the breast (Boone J M *et al* 2000) but since the iodine is the most attenuating material it will result in high S/P ratios. Thus in

the iodine selective image the S/P ratio beneath the iodine will be among the highest in the image. The higher the iodine thickness the stronger the error in its measurement will be. The same holds for thick breasts and in regions of the breast with high glandular to adipose ratios. When the S/P ratios of the breast and adipose tissue are equal then the scatter contribution is cancelled and $t_i' = t_i$. This can be the case only of very low iodine concentrations and when the breast is composed of adipose tissue. It is interesting to note that even in the case of equal intensity beams the S/P ratios cannot be considered as equal at the two different beams since the attenuation of the iodine differs significantly at the two different beams. Thus the detected S/P ratio will be different despite the fact that over the energy range of our interest the S/P ratios in the breast do not change significantly (Boone J M *et al* 2000).

In the above-mentioned formalism, spatial variations of the X-ray field and detector response are assumed that can be effectively corrected using flat fielding. As both variations are energy dependent flat fielding should be performed independently for the low- and high-energy images. In Chapter 5 a quantitative analysis of the above observations will be given.

1.2.4. Noise in dual energy imaging

Assuming that the scattered radiation can be effectively removed, then the uncertainty in the measurement of the iodine projected thickness in the final image will be equal to:

$$\sigma_{\Delta I} = \sqrt{\sigma_{L',h}^2 + \beta_g^2 \sigma_{L',l}^2 + \left(1+\beta_g^2\right)\sigma_{add}^2 + \sigma_{Res}^2} \qquad (1.15)$$

where $\sigma_{\Delta I}$ is the total r.m.s. noise in the iodine-only image, σ_L is the noise in the logarithmic transformed image, σ_{add} is the total additive electronic noise of the detector and σ_{Res} is the residual background noise and is related with uncertainty in the estimation of the glandular composition of the breast due to linear subtraction. Note that in the above equation we assume that there is no correlated noise in the final image since the two images have been acquired independently one from the other and detector nonuniformities have been effectively removed. It is interesting to note that the quantum noise due to the presence of scattered signal $\left(\sqrt{S} = \sqrt{(S/P)\times T}\right)$ in the raw low and

high-energy images will be still present even if the scattered signal in the low and high-energy images can be estimated with good accuracy and thus removed from the images (Kappadath S C and Show C C 2005). Elimination of scattered signal from the raw images will result in substantial reduction of the residual noise.

The variance in the logarithmic transformed image can be measured from the image pair as follows:

$$\sigma_L^2 = \sigma_{T'}^2\left(\frac{\partial L'}{\partial T'}\right) + \sigma_{T_0'}^2\left(\frac{\partial L'}{\partial T_0'}\right) = \left(\frac{\sigma_{T'}}{T(1+S/P)}\right)^2 + \left(\frac{\sigma_{T_0'}}{T_0(1+S/P_0)}\right)^2 \quad (1.16)$$

where $\sigma_{T'}$ and $\sigma_{T_0'}$ are the r.m.s noise of the attenuated and unattenuated signals generated in the detector in the presence of scatter radiation. In the images, the detector additive electronic noise σ_{add} will also be present. It is evident from the above expressions that the dual energy image will be noisier than the single-energy images. However, it is interesting to note that the main benefit of generating an iodine only image apart from suppressing the cluttered background is to derive enhancement thresholds and provide accurate kinetics measurements of iodinated vascular contrast agents from the breast tumours, irrespective of breast composition and thickness.

1.2.5. Image quality metrics

Based on the above expressions the signal to noise ratio (SNR) of an iodinated region of the breast can be used to estimate the theoretical limit in the detection of iodine. In the material selective imaging, assuming that the S/P ratios can be estimated with good accuracy, the SNR can be expressed as

$$SNR = \frac{t_i}{\sqrt{\sigma_{L',i,h}^2 + \beta_g^2\sigma_{L',i,l}^2 + (1+\beta_g^2)\sigma_{add}^2 + \sigma_{Res,i}^2}} \quad (1.17)$$

The SNR suggests that the smallest iodine projected thickness can be detected when the background structure has been completely suppressed for a given photon flux, while the total additive electronic noise is small as compared with other noise sources.

The signal difference to noise ratio (SDNR) can be used as alternative expression of SNR in material selective imaging. The SDNR can be estimated as follows:

$$SDNR = \frac{t_i - t_b}{\sqrt{\sigma_i^2 + \sigma_b^2}} \tag{1.18}$$

where σ_i and σ_b are total r.m.s. noise in the iodine selective image of the iodinated area and background respectively. If the background noise is neglected in the above expression and the residual signal in the iodine selective image is very small then the signal to noise ratio will be equal to signal difference to noise ratio. This relationship (SNR=SDNR) can be used to quantify the effectiveness of the subtraction employed.

Last but not least the iodine contrast to noise ratio (CNR) can be used as an image quality metric to estimate the theoretical limit in the effective visualization of iodine from unsuppressed background. The CNR in the case of glandular tissue suppression can be expressed as:

$$CNR = \frac{\frac{t_i - t_b}{t_i + t_b}}{\sqrt{\sigma^2_{L',b,h} + \beta_g^2 \sigma^2_{L',b,l} + \left(1 + \beta_g^2\right)\sigma^2_{add} + \sigma^2_{Res,b}}} \tag{1.19}$$

where t_b is the residual breast signal.

1.3 System modelling

In conventional mammography, due to the large number of combinations of parameters and detector types, evaluation and optimisation of imaging tasks is best studied through simulation (Maidment D A *et al* 1993, Fahrig R *et al* 1994, Bernhardt P *et al* 2006). In particular, in dual energy imaging, due to the use of two spectra the possible combinations are doubled, so simulation is the only way to either select the best parameters or at least to rule out the majority of the cases. As clinical experience is limited, optimisation and prediction of theoretical limits is essential for the evaluation of this imaging technique and to study the best and worst case scenarios.

Simulations in conventional and in particular in dual energy mammography include either analytical one dimensional simulations (Lemacks M R *et al* 2002), two dimensional image simulations (Boone J M *et al* 1990) or more complex three dimensional phantoms (Bliznakova K *et al* 2003) or Monte Carlo simulations (Ullman G *et al* 2005) or combination of the two (Bernhardt P *et al* 2006). In order to perform a feasibility study for the development of quantitative contrast enhanced mammography we

developed two dimensional image simulations and the evaluation of spectral pair, dose efficacy and iodine isolation has been preformed through SNR, CNR and SDNR. The iodine projected thickness measurements were expressed in mg/cm^2.

The SNR, SDNR and CNR can be used with real and simulated images, as the signal region on the images is known, the mean and the standard deviation (root-mean-square) of that region can be measured. The mean and the standard deviation of a local background averaged over the same area as the signal area could also be measured. It has been shown (Boone M J *et al* 1990) that there is no difference in the results using either the analytical expressions derived above or using simulated images that are based on the analytical expressions. In addition using simulated images provides a way to incorporate structural or spatial noise in the images.

The simulated low- and high-energy images incorporate glandular and adipose tissue. The composition of the simulated phantom was such that the two materials formed a ramp in the iodinated region in order to incorporate residual background noise in the iodine selective image. Thus the iodine and background signals and noise have been extracted from the regions incorporating different breast compositions.

Tumour angiogenesis starts when the tumour size is larger than 2 mm, so iodinated objects are large compared with the pixel size so that frequency dependent blurring effects are not considered in the simulation. Thus the spatial resolution of the simulated images was determined by the sampling. The detection efficiency in both images was determined by the absorption ratio (η_D) of the scinitllator studied and the conversion efficiency was incorporated to the mean system gain $(\overline{G}_D)$. The scintillators are assumed that they have proportional response thus the electron charge read by the detector is expressed electrons per keV deposited on the sensor. The variance of the individual gains of the system can be assumed negligible thus the mean system gain is their linear combination (see chapter 3 Eq. 3.25). Poisson noise was approximated using Gaussian distribution $(\sigma = \overline{G}_D\sqrt{T})$ as the number of detected photons was reasonably large. At present the quantum noise was only considered although detector additive electronic noise and spatial variation in the detector response and X-ray field could be accounted for. Scattered radiation has been incorporated in the simulation in order to study the

effects of scatter in the iodine projected thickness estimates and investigate the performance of scatter correction schemes. Uniform scatter distribution has been assumed. In Chapter 5 the input parameters of the simulation are provided along with the quantitative analysis.

1.4 Spectral pair optimization

The formation of the energy spectral pair is the most demanding practical aspect of dual energy imaging (Kelcz F M *et al* 1977, Chakraborty D P and Barnes G T 1989 and Kappadath S C and Show C C 2005). A methodology for the assessment of the energy spectral pair and their relative fluence based on the iodine SNR weighted by the mean glandular dose will be developed.

The energy spectra provided by an X-ray tube are poly-energetic with broad energy distributions. The use of external beam filtration in order to achieve the two quasi-mono-energetic spectra that straddle the iodine k-edge is essential so as to maximize the iodine signal (Eq. 1.7). The appropriate filter material and thickness for the selection of the optimal spectral pair requires a complex compromise involving x-ray tube heat loading, total mean glandular dose, breast thickness, iodine signal, and noise. The iodine signal-to-noise ratio as defined above has been utilized for this selection. It is evident from Eq.1.17 that when the residual background noise is minimized while the iodine signal is preserved the SNR will be maximum. In addition assuming that the glandular tissue thickness can be estimated with high accuracy $\left(\sigma_{Res} << 1 \& S/P = 0\right)$ then the uncertainty in the estimation of the iodine projected thickness will be proportional to the energy fluence deposited on the detector (Eqs. 1.15-17). If the mean glandular doses from the spectral pair are expressed in mGy/mA they can be used control the spectrum fluence in order to achieve a dose efficient scheme. The relative ratio of low to high energy beams can be determined using similar arguments.

1.4.1. Mean glandular dose dependent spectrum formation

The air Kerma at the breast entrance will be proportional to the tube current for a given spectral distribution and source to breast distance. Therefore, if the photon fluence

per unit energy provided from the tube is expressed in photons/mm^2/mA, then the mean breast entrance air Kerma per mA (mGy/mA) D^j can be measured as follows:

$$D^j = \frac{\int \Phi_0^j(E) \cdot e^{-\left(\mu_f^j t_f\right)} dE}{\int \frac{\Phi_N^j(E)}{\left(\frac{\mu_{en}(E)}{\rho}\right)_{air} \cdot E \cdot q_e \cdot 10^9} dE}, (j = l, h) \quad (1.20)$$

where $\Phi_0^j(E)$ is the X-ray photon fluence spectrum (quanta/mm^2/mA), E is the X-ray photon energy (in eV), μ_f is the mass attenuation coefficient of the filter material (cm^2/mg) t_f is the filter thickness (mg/cm^2), $(\mu_{en}(E)/\rho)_{air}$ is the mass energy absorption coefficient of the air (cm^2/mg),), q_e is the electron charge, and $\Phi_N^j(E)$ is the normalized spectrum incident on the breast. If the breast entrance air Kerma (D) and the breast entrance photon flux are known the mean glandular dose per mA $(\overline{D}_g)$ can be measured as follows (Boone J M *et al* 2002):

$$\overline{D}_g = D^j \cdot NgD_p^j = D^j \cdot \left(\frac{\int b_{t,c}(E) \cdot d_\Phi(E) \cdot \Phi_0^j(E) \cdot e^{-\left(\mu_f^j(E) t_f\right)} dE}{\int d_\Phi(E) \cdot \Phi_0^j(E) \cdot e^{-\left(\mu_f^j(E) t_f\right)} dE} \right), (j = l, h) \quad (1.21)$$

where NgD_p, is a factor the converts the entrance air Kerma to mean glandular dose for poly-energetic beams, $b_{t,c}$ is a scaling factor that takes into account breast thickness and glandular composition at each energy (expressed in mGy/mGy) and d_Φ is a factor that relates the photon fluence to air Kerma (in units of mGy per photons/mm^2/mA). A detailed description and computer-fit equations of the above factors can be found in Boone *et al* 2002.

1.4.2. Spectrum scaling

Division of a reference mean glandular dose (mGy) with the mean glandular dose per mA for a given spectrum fluence (quanta/mm^2/mA), can provide a mean glandular dose dependent scaling of the spectrum as follows:

$$F=\frac{\overline{D}_g^{ref}}{\overline{D}_g^{j}}=\overline{D}_g^{ref}\cdot\left(1.6\cdot10^{10}\cdot\frac{\int\frac{\Phi_N^j(E)}{(\mu_{en}(E)/\rho)_{air}\cdot E}dE\cdot\int d_\Phi(E)\cdot\Phi_0^j(E)\cdot e^{-(\mu_f^j(E)t_f)}dE}{\int b_{t,c}(E)\cdot d_\Phi(E)\cdot\Phi_0^j(E)\cdot e^{-(\mu_f^j(E)t_f)}dE\cdot\int\Phi_0^j(E)\cdot e^{-(\mu_f^j(E)t_f)}dE}\right)(j=l,h) \quad (1.22)$$

where, $\overline{D}_g^{ref}$ is a reference mean glandular dose used to weight the photon flux of the spectrum. The scaling factor was used to restrict the thickness of the filtration so as to achieve tolerable currents from the tube. The methodology described normalises the spectra so as the total mean glandular dose will be equivalent to predetermined value. The low and high energy spectrum flux has been assessed by studying the dependence of the SNR versus the ratio of high mean glandular dose$\left(\overline{D}_g^{h}\right)$ to total mean glandular dose$\left(\overline{D}_g^{Tot}\right)$.

1.5 Summary

In this chapter the theoretical framework for breast k-edge energy imaging has been presented. Using the above analysis for the measurement of iodine projected thickness, vascular contrast medium enhancement and kinetics measurements can be performed irrespective of breast composition, breast thickness and detector material. The detrimental effect of scatter radiation has been determined analytically in order to evaluate its effect on the iodine projected thickness measurements. Image quality metrics to find theoretical limits of the iodine detection were provided. Two dimensional image simulations based on the derived analytical expressions can be used to select optimal parameters. A methodology for the assessment of the energy spectral pair and their relative fluence has been developed in order to provide a dose efficient scheme that is crucial for the evaluation of the clinical potential of the proposed imaging technique. The remainder of the thesis organised as follows:

- Chapter 2 describes the CMOS APS sensors used in this study and introduces the main components of the CMOS active pixel flat panel imager (APFPI).
- Chapter 3 presents the theoretical framework along with computational methods to perform electro-optical and X-ray performance evaluation of digital detectors.

- Chapter 4 presents thorough electro-optical and physical performance characteristics of the APFPIs.
- Chapter 5 presents a quantitative analysis of the analytical expressions derived above and the development of quantitative contrast enhanced mammography.
- Chapter 6 compares the findings of this work with the literature and investigates the clinical potential of the system developed.

Chapter 2

Active Pixel Flat Panel Imager

2.1. Overview

This Chapter describes the main properties and the pixel architecture of the three different CMOS APS sensors used in this study. A brief description of the properties of the x-ray converter selected is also presented. Lastly the final system that has been assembled to from the CMOS active pixel flat panel imager (APFPI) is described.

2.2. Detector requirements for conventional and perfusion mammography

The minimal requirements for effective performance of a mammographic system able to perform conventional and advanced mammography can be summarized as follows. The limiting resolution of the system is stated by the detection of microcalcifications (200 um in size), an early indicator of breast cancer. A pixel pitch in the range of 25-70 μm is assumed to be adequate. The sensitivity of a system is directly related to the dose absorbed by the patient, thus it has to be high and, in particular for perfusion mammography, is the most critical requirement. However, a signal-to-noise ratio approximately equal to 5 is the minimal requirement for efficient detectability (Rose A *et al* 1953). High dynamic range (12 bits or at least 3100 grey levels for digital systems Maidment A D *et al* 1993) is required in order to avoid high breast compression, to visualize dense breasts and accommodate the maximum raw exposure. Scattered radiation decreases the SNR which means an effective way of eliminating it is required (antiscatter grid or scanning operation). Furthermore, images in digital form that give the capability of acquiring a series of images, direct post processing of the images, contrast and peripheral enhancement (Tang H *et al* 2001 and Snoeren P R *et al* 2006) and use of computer aided diagnosis (CAD) systems (Pisano E T *et al* 2005) are essential for improved sensitivity and specificity (Doi K *et al* 2006). Fast image acquisition in order to further reduce the overall examination time and perform dynamic imaging is crucial. Last but not least for quantitative imaging detector image lag, ghosting (Bloomquist A K *et al*

2006) and baseline drifts have to be minimal (Jong R A *et al* 2003). CMOS active pixels sensors are able to fulfill the above requirements.

2.3. CMOS Active Pixel Sensors

CMOS active pixels sensors (APS) are integrating sensors; this means that they depend on the measurement of the charge integrated on a photoelement, (i.e. photodiode capacitance) as the sensing method. Such circuits operate by resetting the photoelement, allowing charge to accumulate and then sensing the charge value. A CMOS APS incorporates at least 3 transistors per pixel: a reset transistor that resets the photoelement, a source follower input transistor that converts the accumulated photocharge to voltage, and a row select transistor that selects the row to be read. The term "active" refers to the incorporation of the active amplifier within each pixel (source follower input transistor). The readout is column-parallel. CMOS Passive Pixel Sensors (PPS) can also be designed: they only feature 2 transistors per pixel and their operation is analogous to that of active matrix flat-panel imagers (AMFPIs) currently used in digital radiography. However, CMOS PPS suffer from higher read noise and lower speed than APS due to the way they are operated (Fossum E R *et al* 1997).

In the present study three different CMOS APS with different pixel architectures were used. All sensors offer different characteristics that where very attractive for medical imaging. In Table 2.1 the design specifications of the three sensors are given.

Table 2.1. The design specifications of the three CMOS APS sensors.

Design specifications	**3T APS**	**Vanilla**	**OPIC**
Pixel format	525 x 525	520 x 520	72 x 64
Pixel pitch	25 μm	25 μm	30 μm
Array dimensions	13 mm x 13 mm	13 mm x 13 mm	2 mm x 2 mm
Optical fill factor	~75 %	~80%	~10%
CMOS process	0.5 μm	0.35 μm	0.25 μm
Optical sensor	N-Well photodiode	N-Well photodiode	N-Well photodiode
Frame rate (full array)	10 fps	~40 fps	~3700 fps
ADC	10 bits (on-chip)	12 bits (of-chip)	8 bits (on-pixel)

2.4. N-well photodiode

The sensing element of the three CMOS APS sensors used is based on an n-well to p-substrate photodiode. The n-well photodiode produces an effective electrostatic potential between the photosensitive volume and the unrelated junction of the read out circuitry. With this pixel architecture, charge collection from the epitaxial layer (epi-layer) and beyond the photodiode area is achieved insuring high fill factor (Dierickx B *et al* 1997). In Figure 2.1 the properties of the photodiode are visualised for the case of charged particle detection (Turchetta R *et al* 2001). It demonstrates that charge released in the epi-layer can diffuse and be collected at the photodiode. A similar effect is observed from photoelectric interactions of visible photons. The passivation layer is of the order of a few microns (top layer in Fig. 2.1) making the sensor very sensitive to visible light and in particular to the blue part of the spectrum (Lulé T *et al* 2000).

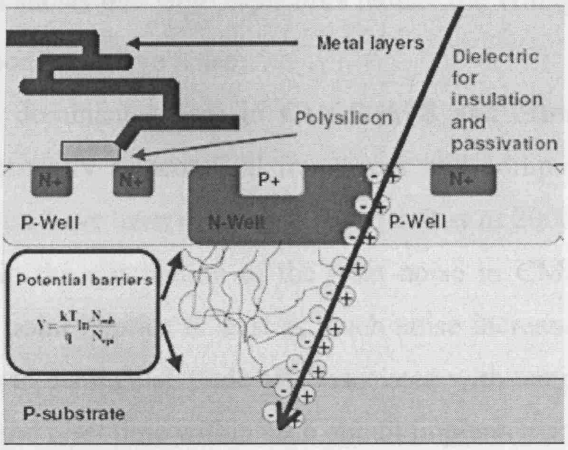

Figure 2.1. Schematic cross section diagram of the structure of the pixel and n-well to p-substrate photodiode. The two electrostatic potentials are proportional to the ratio of the holes concentration between the p-well and the epi-layer and the epi-layer and the substrate. This difference in the concentration of holes (three orders of magnitude) acts as reflective barriers for the electrons. The passivation layer, metal lines, and NMOS transistors are also shown (Turchetta R *et al* 2001).

2.5. Reset modes and noise reduction in CMOS APS

A standard three transistor (3T) CMOS APS pixel may be reset in two ways. The reset is termed "soft" if the reset gate is clocked high to the supply voltage of the sensor. This leaves the potential under the reset gate less than the sense node voltage by the reset transistor's threshold voltage, allowing charge from the photodiode to thermally cross the reset gate barrier. As a result, the current image may be affected by residual charge from

the previous frame, commonly known as image lag. For soft reset, noise from the reset transistor is half the usually quoted kTC noise (Tian H *et al* 2001). By performing a "hard" reset, where the reset transistor is overdriven with a voltage greater than the sum of the supply voltage and the threshold voltage, the field that would cause charge to leave the sense node is eliminated. However, this reset approach exhibits the full kTC noise.

Reset noise is typically caused by thermal and shot noise sources that are intrinsic characteristics of all resistors, transistors, and diodes. When a capacitor C (parasitic capacitance of photodiode) is reset to a dc voltage through a resistive switch (reset transistor), and the switch is abruptly opened, the noise voltage power on the capacitor is $\sigma_{V_c}^2 = kT/C$. Since the voltage multiplied by the capacitance equals charge, the charge noise stored on the capacitor after reset is $\sigma_{Q_c}^2 = kTC$. The reset noise in r.m.s. electrons is $\sigma_{rst} = \sqrt{kTC}/q$. This shows that large capacitors reduce the voltage noise. Conversely, smaller capacitors reduce the charge noise.

Reset noise is the dominant source in CMOS APS and effort has been directed towards reducing it. Recently a theoretical framework and computational methods for calculating the reset noise have been developed (Fowler B *et al* 2006) possibly leading to improved approaches in the elimination of the reset noise in CMOS APS. Of course, noise reduction at one point implies at least as much noise increase somewhere else. In any case it is necessary to distinguish trade offs associated with temporal noise, dc offset, stability, lag, linearity and reset time within each circuit implementation.

2.6. The sensors - 3T APS (Startracker)

The first sensor is a 525 × 525 CMOS APS array with 25 × 25 μm pixel pitch and on-chip column-parallel 10-bit analog-to-digital converters (ADC). The sensor at its current version reads only at 10 frames/sec (integration time=100 msec) and is operated in a rolling shutter way. In the rolling shutter, the rows of pixels in the image sensor are reset in sequence, starting at the top of the image and proceeding row by row to the bottom. When this reset process has moved some distance down the image, the readout process begins: rows of pixels are read out in sequence, starting at the top of the image and proceeding row by row to the bottom in exactly the same fashion and at the same speed as the reset process.

The pixel has 4 n-well photodiodes (PD) as sensing elements along with reset, source follower (SF), and row select transistors (Fig. 2.2). The four n-well photodiodes were placed at 12.5 μm pitch (Prydderch M L *et al* 2003). This pitch was designed in order to increase the charge collection efficiency from the bulk epi-layer, provide uniform charge collection and eliminate charge diffusion to neighbouring pixels (Soo L J *et al* 2003, Shcherback I *et al* 2004). The 3T APS provides the highest possible fill factor, for a given CMOS process, a very critical requirement for X-ray medical imaging. This pixel architecture is scalable to large formats with minimal degradation in the performance of the sensor (Scheffer D *et al* 2007).

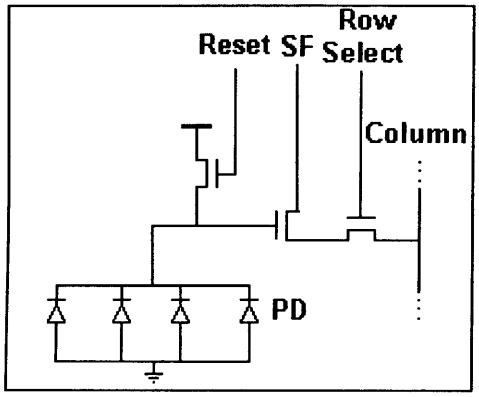

Figure 2.2. Pixel architecture of the 3T CMOS APS, with the 4 n-well photodiodes, the reset, the source follower input (SF), and the column select transistor.

2.7. The sensors - Vanilla

The second sensor, Vanilla, is a 520 × 520 array of 25 × 25 μm pixel pitch with random pixel addressing and region of interest readout. Although, the sensor comes with a 10 bit on-chip ADC, the 12-bit off chip ADC was used for full frame readout at up to 140 frames/sec (fps). A frame rate of over 20Kfps can be achieved for a region of 6x6 pixels using analogue readout and digitising off chip via a fast ADC. Low reset noise is achieved using a 'flushed' reset (Pain B *et al* 2003). A flushed reset achieves the low noise of soft reset, while overcoming the associated image lag by performing a hard reset followed immediately with a soft reset. The hard reset is the 'flush' as this completely erases the pixel while the soft reset provides the low noise. To achieve this, an extra reset circuit is added off-pixel so quantum efficiency and dark current performance is unchanged (Fig 2.3).

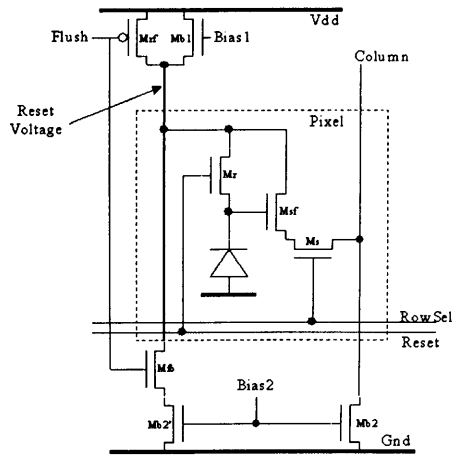

Figure 2.3. Pixel architecture of the Vanilla CMOS APS including the flush reset circuitry.

2.8. The sensors - OPIC

The last APS used is a test structure with on-pixel ADC and will be referred to as On Pixel Intelligent CMOS (OPIC). It allows high-speed read-out (>3700 frames/sec) and snap shot digital imaging (Kleinfelder S *et al* 2001). This structure comprises a 72 × 64 pixel array with 30 × 30 μm pixel pitch. Each pixel, apart from the 3T circuit and the photodiode, incorporates two in-pixel DRAM 8-bit memories and a comparator (Fig. 2.4). The OPIC sensor with on-pixel ADC enables high frame rate and offers increased on-pixel functionality. Three different read out modes are possible. The first is the raw ADC value corresponding to the pixel signal. The second is the address of pixel location for sparsification of the image. The third is a time related value that records the time taken for the pixel signal to cross an external threshold. The on-pixel comparator compares the pixel signal level to the global threshold value and a "hit flag" is set to select only pixels above the threshold for sparse readout. The two in-pixel DRAM memories are used to store an 8-bit gray coded value equivalent to ADC value following voltage conversion, and also the time-related code when the diode passes the global threshold voltage. However, the high degree of pixel level integration provides the smallest fill factor of the three different sensors employed in this study.

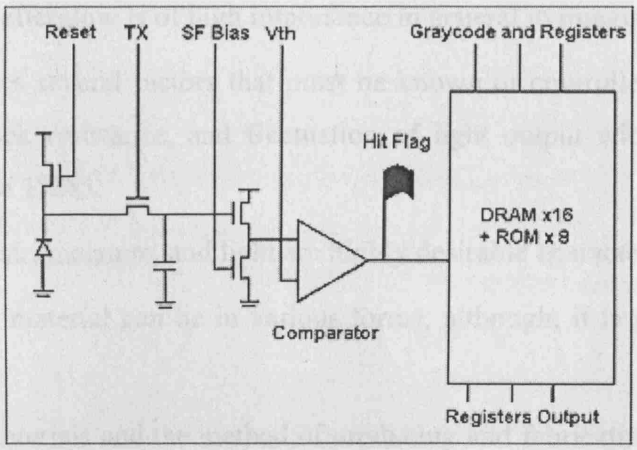

Figure 2.4. Schematic diagram of the two different the OPIC pixel with the read out transistors, on-pixel ADC, comparator, and "hit flag".

2.9. X-ray converters for indirect detection for conventional and perfusion mammography

In indirect x-ray imaging systems the x-ray converter is a very critical component of the system that defines the resolution and the sensitivity of the system (excluding any secondary quantum sink within the components of the system). The most important considerations in the pursuit of the 'best' x-ray converter for mammography applications are:

1. The scintillation wavelength, which will determine the spectral matching factor and the suitability of combining the x-ray converter with the photoreceptor.
2. Increased light yield is important in improving sensitivity and spatial resolution (Swank R K *et al* 1973).
3. High density and attenuation coefficient (i.e., high effective atomic number) are important for reducing the amount of scintillator material needed, thus increasing the spatial resolution (Van Eijk C W E *et al* 2002).
4. Energy resolution and proportionality also depend on light yield, which in case of extrinsic scintillators depends on the activator concentration (Trefilova L N *et al* 2002)
5. Fast signal rise and decay times are important for high readout rates (Van Eijk C W E *et al* 2003).

6. The absence of afterglow is of high importance in general in imaging systems.
7. Stability includes several factors that must be known or controlled: ruggedness and mechanical shock resistance, and fluctuation of light output with temperature and time (Holl I *et al* 1988).
8. Insensitivity to air, moisture, and light are highly desirable characteristics.
9. The scintillator material can be in various forms, although, it is preferable to be in solid form.

The price of raw materials and the method of producing and fabricating the material into the desired size and shape all enter into the final cost, although for such a demanding task this is usually not so critical.

2.10. CsI:Tl properties

CsI:Tl scinitllator with columnar structure fulfils most of the required criteria. CsI:Tl due to its columnar structure gives the lowest possible light diffusion as a function of thickness as compared with powder scintillators (Yu T *et al* 1997). This property gives the ability to increase the stopping power by increasing its thickness offering a high quantum efficiency detector in a broad range of energies (10-70 keV) (W Zhao, *et al* 2004). The drawback of increasing CsI:Tl thickness is that the light output is decreased (Moszynsky M *et al* 1997); however, the overall performance (DQE) of this scintillator is very high (Samei E *et al* 2003). Additionally, due to its columnar structure high resolution imaging can be performed (Fig 2.5).

One of the most important properties of CsI :Tl is the light yield which is defined as the number of photons created in the crystal per unit of absorbed ionizing energy (photons/MeV) (Van Eijk C W E *et al* 2003). It is among the most luminous room-temperature phosphors with a light yield of 67.000 Photons/MeV (Weber M J *et al* 2002), thus the x-rays can be efficiently detected and the scintillation light can be well confined. The matching factor directly affects the sensitivity of the imaging system and describes the spectral matching between the emission light of the scintillator and the sensitivity of the sensor. The system gain that is proportional to matching factor has to be at least of the order of 10 electrons/x-ray (~18 keV) in order to achieve quantum limited performance

(Yaffe M J *et al* 2000), although this number depends on the detector total additive electronic noise. The higher it is the better matching factor should be achieved. The CsI:Tl has an emission spectrum in the green region (~540 nm) of the spectrum because it is doped with Thallium (Tl) (Schotanus P *et al* 1990) and, when coupled to CMOS sensors, gives very good spectral matching (see chapter 4).

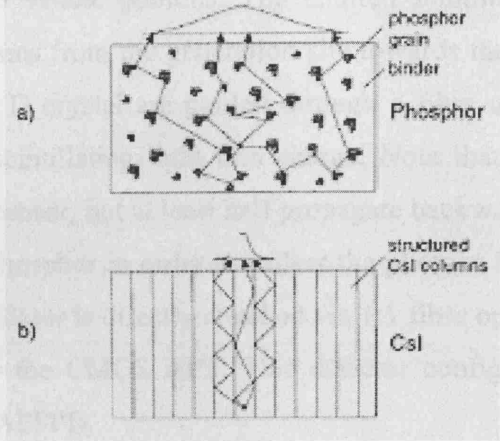

Figure 2.5. Two types of scintillator structures: (a) settled scintillator, (b) columnar CsI scintillator. A hypothetical line spread function of each system is shown (Yaffe M J *et al* 1997).

The decay time and afterglow of the x-ray converter are very important in dynamic studies. For activator ions in CsI:Tl 'converters' the visible scintillation radiative decay times are generally limited to 0.8 to >6 μs. A preferred condition is that <0.01% of the maximum scintillation intensity is emitted after 3ms. The afterglow of the CsI:Tl is high (2% after 3 ms), however, by codoping with Eu^{2+} it can be suppressed to be adequate even for high speed imaging (Nagarkar V V *et al* 2006). Local variations in the scintillation light output are unavoidable using x-ray converters. A possible origin of this inhomogeneity can be a concentration gradient or local fluctuation of luminescence centers in a scintillation crystal. The number of scintillation photons then depends on the point in the phosphor at which the scintillation light is created. For very high light yield performance local variations in the scintillation gain are unavoidable. This result in long range image correlations (corresponding to low spatial resolution) and large magnitude signal fluctuations (Siewerdsen J H *et al* 1998). A nonproportional response of CsI:Tl has been reported and seems to be strongly affected by the x-ray photons energy (Dorenbos P *et al* 1995). Despite the short falls of the CsI:Tl, in terms of image quality in the

diagnostic energy range, it outperforms all the alternative scintillators for radiographic imaging.

2.11. The prototype CMOS active pixel flat panel imager

The sensing element of the system consists of the CsI:Tl scintillator that converts the incident x-ray quanta to visible photons. The emitted scintillation photons propagate through the CsI:Tl columns from the generation site towards the sensor (Fig. 2.5.). The photons exiting the CsI:Tl crystal are guided through a fibre optic plate to the CMOS APS that converts the scintillating light into charge. Note that not all the photons are propagated towards the sensor, but at least half propagate backwards. A reflection coating is added on top of the phosphor in order to reflect the photons back towards the CMOS sensor. The CsI:Tl scinitllator is directly attached via 1:1 fibre optic faceplate (FOP) with 60-70% transmission to the CMOS APS. This detector configuration forms an active pixel flat panel imager (APFPI).

The sensors used in this study have integrated column-parallel ADCs offering a full digital interface (Fig. 2.6) and the sensors are fully X-Y addressable. The data acquisition (DAQ) hardware is based on a specifically designed field programmable gate array (Xilinx), which provides the timing and control logic block for readout. All the sensors are controlled using the same DAQ. Finally the data are transferred to the host computer for displaying, saving, and further analysis. The detector bias and operation settings, such as the type of reset (hard, soft or flush), the range that the ADC ramps e.t.c. can be set by the user using a vector generator and downloaded to the FPGA. This means that along with the characterization of the device, optimum performance is achieved in order to utilize the sensors according to the imaging task.

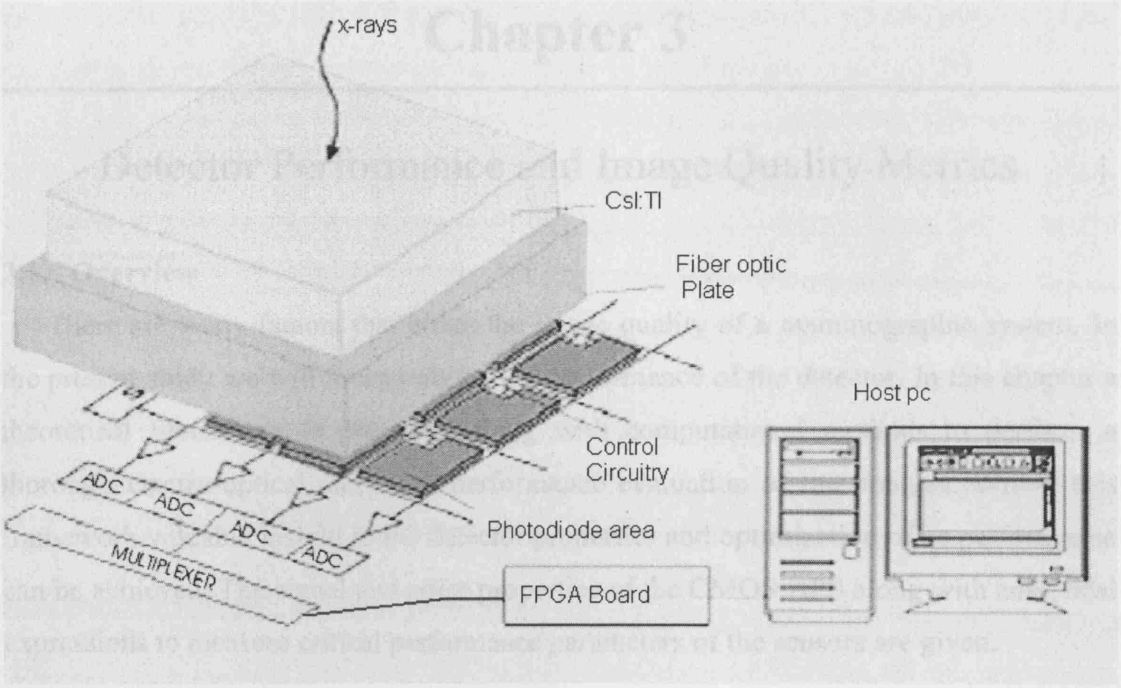

Figure 2.6. Diagram showing the active pixel flat panel imager (APFPI) (thicknesses of different layers are not drawn to scale).

2.12. Summary

In this Chapter the design characteristics and the pixel architecture of the three different CMOS APS sensors used in this study have been provided. The CsI:Tl with columnar structure was selected as X-ray converter as it offers high resolution, high light yield and good spectral matching with CMOS APS. Finally, the main components of the systems that have been assembled to form a high performance x-ray imagers for diagnostic radiology named as CMOS-APFPI was presented. The high performance anticipated from this detector technology will facilitate the development of new imaging approaches such as quantitative contrast enhanced mammography that require a limited number of low dose images per examination

Chapter 3

Detector Performance and Image Quality Metrics

3.1. Overview

There are many factors that affect the image quality of a mammographic system. In the present study we will focus only on the performance of the detector. In this chapter a theoretical framework is presented along with computational methods to perform a thorough electro-optical and x-ray performance evaluation of the imagers. Within this framework valuable insight to the detector properties and optimization of its performance can be achieved. The signal and noise properties of the CMOS APS along with analytical expressions to measure critical performance parameters of the sensors are given.

3.2. Transfer theory and spatial frequency assessment of X-ray imagers

The term "transfer signal" in X-ray imaging systems has come to mean the description of the transfer of spatial detail in the signal from the input to the output of an imaging system, while "noise transfer" relates to the corresponding noise attributes (Cunningham I A *et al* 1999).

The concept of noise variance transfer has little meaning for the description of x-ray imaging systems due to noise correlations. If the system response were truly the same at all points, then global descriptors (contrast, SNR) would be completely satisfactory to characterize all behaviors of the system. However, the fact that both signal and noise are spatially correlated to some degree makes it useful to consider a frequency-response characterization. Transfer theory for characterising an imaging system must therefore be tied somehow to concepts of both image structure and system spatial resolution. This can be achieved in the frequency domain with the application and extensive use of Fourier transform and related theorems.

The analysis of digital detectors is thus tied to the theoretical framework of linear systems theory in order to describe the signal and noise transfer from the input to output. A linear response is generally necessary before a linear systems approach can be used to analyse system performance. Thus the first step in any analysis is to ensure that the

system under study is indeed linear (or linearisable). Essentially, this means the output must be proportional to the input throughout the dynamic range of the detector.

A system must also have a sift-invariant response especially when Fourier-based analysis is used. This requires that the system impulse-response function be shift-invariant so that a particular structure in the image will appear the same, regardless of where in the image is placed (Dobbins J T *et al* 1995). For example, in digital detectors the analog (presampling) signal, and noise propagated through the detector, are sampled by the digital matrix at discrete points, and the system response is not strictly shift invariant (unless shifts are by an integer number of pixels). However, if the *presampling* signal and noise are stationary, complications arising from the nonstationarity of the sampling process may be taken explicitly into account. A system that is both linear and shift invariant in its response is sometimes referred to as "LSI" system.

3.2.1 Cascaded system

In a cascaded system such as digital detectors, the output of one stage constitutes the input to the following stage. In a linear, shift invariant cascaded system each of the independent stages are also linear and shift invariant. At the output of any given stage of a cascaded detector system, the minimum possible value of the noise spectrum is that set by the (uncorrelated) Poisson variance of the output quanta which is equal to the number of quanta. This means that in a cascaded linear system the noise generated is effectively passed as signal to the subsequent stage (Rabbani M *et al* 1987). In general, the processes in a cascaded imaging system could be described as introducing either gain or blur. For example blur (noise correlations) may be introduced in a stochastic amplification process such as the conversion of x-ray photon to many light photons in the radiographic screen. The relationship between the input and output signal and noise are governed by the properties summarised in Fig. 3.1.

For each stage, *i*, the signal is described by the distribution of image quanta, $q_i(x, y)$, and the noise is described by the noise power spectrum (NPS), $S_i(u, v)$ where (x, y) and (u, v) are orthogonal spatial and spatial-frequency coordinates, respectively. A process which changes the mean number of image quanta is described by a gain stage and characterized by an intrinsic average gain, $\overline{g_i}$ and a variance in that gain, σ^2. A process

which changes the spatial distribution of the image quanta is described by a spreading stage and characterised by the modulation transfer function (MTF), $T_1(u,\upsilon)$, given by the point spread function (PSF), p(x, y). The amplification (gain) and blurring (spreading) processes could be classified as either deterministic or stochastic.

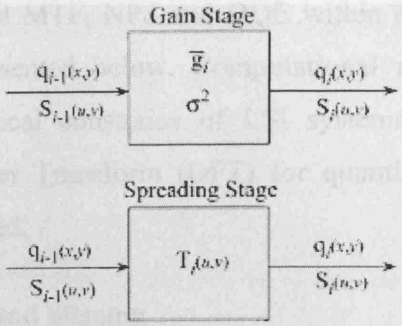

Figure 3.1. Schematic illustration of the properties governing the signal and noise transfer for gain and spreading stages (Siewerdsen J *et al* 1997).

3.2.2 Amplification processes

Amplification processes are those that describe the change in the average number of quanta (photons, electrons, holes, etc.) between the input and output of a given stage. Gains may be greater than, less than (quantum sink), or equal to unity. In a stochastic gain process, the number of output quanta is not uniquely determined, but obeys a statistical distribution that describes the gain process. If the gain $(\bar{g})$ is smaller than 1 (e.g., stages representing absorption or attenuation) the statistics of the amplification process are simplifying represented by a binomial selection process.

3.2.3 Blurring processes

In a blurring process, the number of quanta is the same at the input and output, but the spatial distribution of the quanta has been modified according to the MTF (modulation transfer function) associated with the process. The blurring process can be either stochastic or deterministic. In a *stochastic blurring* process, the spatial locations of the output quanta is not uniquely defined but are distributed according to the point spread function that characterises the scattering process. In a *deterministic blurring* process, such as occurs when quanta are incident on an integrating aperture (pixel), the individual quanta are summed in the aperture, and the process is accurately described as a

convolution with a continuous function in space. Unlike a stochastic blur, there is no spatial noise introduced by a deterministic blur.

3.3. Empirical physical characteristics of the X-ray imager

The frequency domain analysis for the performance evaluation of the x-ray imagers and definitions of the digital MTF, NPS and DQE within the theoretical framework of LSI systems theory is presented below. Computational methods to evaluate digital systems within the theoretical constrains of LSI systems theory along with proper handling of Discrete Fourier Transform (DFT) for quantitative assessment of digital systems will also be presented.

3.3.1 Presampling MTF and aliasing

The MTF in digital systems is usually described by the response of a system to a single frequency (u) sinusoid:

$$MTF_d(u) = \frac{|FT_d(u)|}{|FT_{in}(u)|} \tag{3.1}$$

where $FT_{in}(u)$ and $FT_d(u)$ are the amplitudes of the sinusoid before and after sampling. One commonly used form for the DFT (in one dimension) of a sequence of N values α_n for $0 \le n \le N-1$ is given by:

$$A_m = DFT\{\alpha_n\} = \sum_{m=0}^{N-1} \alpha_n e^{i2\pi nm/N} \tag{3.2}$$

which consists of a sequence of the N complex values A_m for $0 \le m \le N-1$. Sinusoidal functions are thus identified as being eigenfunctions of the imaging system, while the MTF describes the eigenvalues. By definition MTF is normalised to unity at $u = 0$. The 1D MTF is typically measured by the Fourier transform of the line spread function as:

$$MTF_d(u) = FT\{LSF(x)\} \tag{3.3}$$

where $LSF(x) = \int_{-\infty}^{+\infty} psf(x,y)dy$ is the line spread function and FT indicates the Fourier transform operator.

The characterization of the spatial-frequency response from the system's MTF requires the imaging system to be linear (or linearazable) and shift invariant, which is the

case only for finely sampled signals. However, for undersampled digital systems, the MTF is no longer a simple mapping of input to output frequency amplitudes. Undersampling in digital systems occurs when the image is not sampled finely enough to record all frequencies without aliasing. In order to avoid aliasing, the sampling frequency F_S has to be at least twice the Nyquist frequency $F_{Nyquist}$:

$$F_S \geq 2 \cdot F_{Nyq} \tag{3.4}$$

where $F_{Nyquist}$ is:

$$F_{Nyq} = \frac{1}{2x_0} \tag{3.5}$$

where x_0 is the pixel size. The presampling MTF has its first zero at $u=1/x_0$, twice the cut-off frequency, and aliasing may be hard to avoid. For measuring the digital MTF finely sampled techniques have been developed (Fujita H *et al* 1992 and Samei E *et al* 1998).

3.3.2 Oversampled line spread function and image corrections

The oversampled LSF of digital systems can be measured using the slanted slit technique (Fujita H *et al* 1992) as it provides a very accurate and simple way to oversample the LSF. Careful alignment of the slit camera should be obtained (Samei E *et al* 2006). The slit with respect to the detector pixel matrix is placed in an angle of approximately 2^0. The angle is measured by plotting the maximum transverse profile along the length of the slit versus pixel location of the profile (Dobbins J T *et al* 1995). In Figure 3.2 the maximum values indicate that the slit is above the center of a pixel whereas the minimum indicate that the slit is at the edge of the pixel. By measuring the pixel distance (d) of two consecutive minimum values the angle of the slit can be measured as follows:

$$\tan(\theta) = \frac{1}{d} \tag{3.6}$$

where θ is the angle of the slit with respect to detector matrix. Averaging over all the minimums high accuracy in the angle determination is achieved.

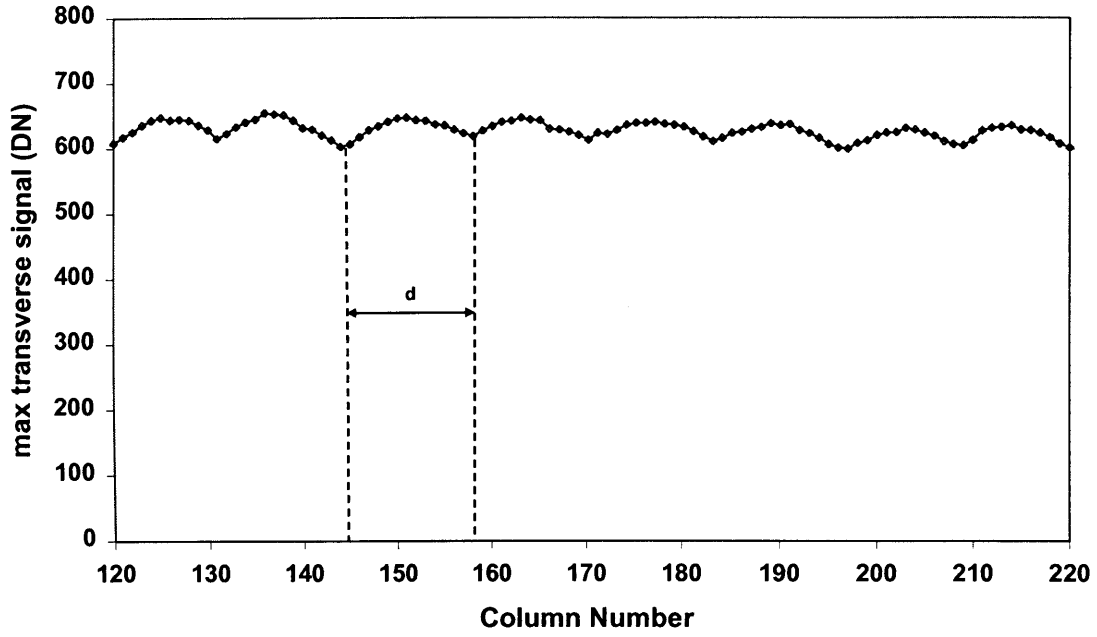

Figure 3.2. Plot of maximum transverse profile pixel value expressed in digital numbers (DN) versus column number. This is in the case of the slit placed vertical to the columns of the detector.

The slit images have to be corrected for sensor offset and phosphor spatial gain variations. Those corrections are performed on a pixel by pixel basis and are summarised in Eq. 3.7.

$$a(x,y) = \frac{1}{NM}\left[\sum_{x=1}^{N}\sum_{y=1}^{M} a_{n,dsf}(x,y)\right]\frac{a_{n,s}(x,y)}{a_{n,dsf}(x,y)} \tag{3.7}$$

where a is the corrected pixel value, $a_{n,dsf}$ is a pixel value of an averaged dark subtracted flat field image $a_{n,s}$ is a dark subtracted pixel value of the slit image and N, M are sensor dimensions.

The oversampled line spread function (LSF) can be measured by rearranging the data from one minimum to the next (Fig 3.3). The maximum of the LSF is positioned at zero distance. Variations along the edge of the slit have to be corrected by dividing with the integral of the line perpendicular to the slit (Vedantham S *et al* 2000). This correction is applied by normalising the pixel values on column by column basis as follows:

$$b_1 = \frac{a_1}{a_1 + a_{10} + a_{11} + a_{20} + a_{21}} \tag{3.8}$$

where a_1 is the pixel value and b_1 is the same pixel value after applying the normalisation. The slit row data have been converted to double precision numbers in order to avoid loss of information (truncation error) due to this division.

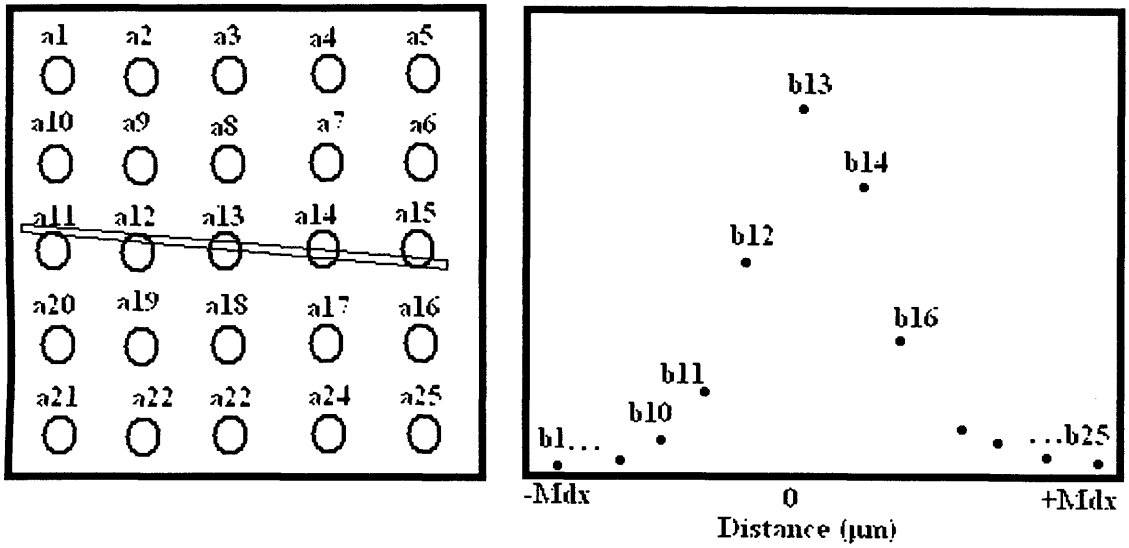

Figure 3.3. Illustration of slit image oversampling and correction for slit width variations. The distance between two points is $\tan(\theta)\cdot dx$, with dx equal to pixel size.

After the oversampling, one has to shift the x-axis of the LSF data in order to have the peak of the LSF at the origin in order to avoid zero position and phase errors. The sampling frequency Δf, as determined by the angle of the slit is:

$$\Delta f = \frac{1}{N \tan(\theta) x_0} \tag{3.9}$$

where N is the number of sample points (the number of the LSF points) ϑ is the angle of the slit with respect to detector matrix and x_0 is the pixel size.

3.3.3 Digital MTF

The FFT of the oversampled LSF gives the presampled MTF of the digital radiographic system. The term presampled MTF is referred to the free of aliasing MTF of the system as it was measured with the aid of the fine sampling techniques. The finite width of the slit introduces a bias in the measurement of the MTF of the system. Thus

convolution in the frequency domain with the sinc function of the slit provides the true presampled MTF of the system.

$$MTF_{true}(f) = \frac{MTF_{pre}(f)}{\sin c_{slit}(f)} \tag{3.10}$$

The MTF was truncated up to maximum frequency $1/x_0$.

3.3.4 Digital NPS

The noise power spectrum may be understood as the variance of image intensity (i.e. image noise) divided among the various frequency components of the image (Cunningham I A *et al* 2000). The NPS is two dimensional, and when integrated over all frequency space, gives a value equal to the variance of image values (such as pixel values in a digital image). The NPS is measured by finding the variance at each spatial frequency component in an ensemble of measurements of white field images.

Assuming that the resulting signal has been sampled by δ functions scaled by the values α_n, then the NPS is the presampling NPS. In practice, it is not possible to measure NPS_{pre} because the input to a system will contain all noise frequencies simultaneously (white noise from a flat field x-ray exposure), including those above cut-off frequency $(F_{Nyquist})$. The two dimensional digital NPS is given by

$$NPS_{dig}(u,\upsilon) = \lim_{X,Y\to\infty}\left\langle \frac{1}{XY}\left| x_0 y_0 \sum_{n=0}^{N-1}\sum_{m=0}^{M-1} a_n(nx_0, my_0)\, e^{-2\pi i(ux-\upsilon y)}\right|^2 \right\rangle \tag{3.11}$$

where the pointed brackets denote ensemble averaging, $X = Nx_0$ and $Y = My_0$, x_0 and y_0 are the x and y spacing of the discrete values (pixel dimension) and N and M the image dimensions (in our case N=M and x_0=y_0). The $a_n(x,y)$ is evaluated at a set of discrete values $x=nx_0$ and $y=my_0$ where n=0,1....N-1 and m=0,1...M-1. The digital NPS is defined (in the case of 1-D) only for the frequencies:

$$u = \frac{n}{Nx_0} \tag{3.12}$$

for $-N/2 \le n \le N/2$. At these frequencies the digital NPS can be viewed as a numerical estimator of the presampled NPS.

3.3.5 Presampling NPS and noise aliasing

The aliasing problems that exist in the interpretation of the MTF in a digital system also apply to the interpretation of the NPS as stated by the sampling theorem. Unfortunately, the presampling NPS cannot be directly measured using fine sampling techniques such as commonly employed to measure the presampling MTF. Therefore the NPS consisting of the full complement of input frequencies, plus the aliases, is the only NPS readily available (Dobbins J T *et al* 1995). The noise components to frequencies greater than u_c $(1/2x_0)$ get aliased into the image noise at lower frequencies. This means that NPS does not describe the variance in amplitude of each frequency component of a system. Thus the NPS is computed only up to the cut-off frequency ($F_{Nyquist}$). Strictly speaking due the aliasing in the NPS one should referred to the image quality metrics that use the NPS as estimated and not determined values. In the NPS estimation there is no phase dependence, because the NPS is defined as the ensemble average that includes contributions from all possible random phases of the noise.

3.3.6 Two dimensional NPS

For the NPS measurement, computing directly the 2-D NPS using FFT routines that are available in all software programs is straight forward, and gives the possibility of describing the noise correlations to all directions in the image as well as finding numerous artifacts that cannot be seen from 1-D NPS. However, there are many practical and experimental considerations when measuring the NPS, which require a careful handling of the data. In particular, when Fourier-based analysis is used, a system must be linear and shift invariant. This requires offset and background trends, such as the heel effect, to be removed before any quantitative analysis is performed. In Table 3.1 the various methods proposed so far to detrend the images are shown. The second degree polynomial fit is adequate to eliminate spectral leakage of the very low frequency background trends that can inflate the low frequency NPS (Williams M B *et al* 1999). Note that the user of any FFT routine should be aware of the FFT algorithm being used before attempting any quantitative work. The raw 2D NPS can be computed as follows:

$$NPS_{Raw}(u,\upsilon) = \frac{\left\langle \left| FT(a_n(x,y)) \right|^2 \right\rangle}{N_x N_y} \Delta x \Delta y \tag{3.13}$$

where,

$$a_n(x,y) = a_{n,ff}(x,y) - P(x,y) \tag{3.14}$$

and $\left\langle \left| FT(a_n(x,y)) \right|^2 \right\rangle$ represents the ensemble average of the squares of the Fourier amplitudes from all ROIs, N_x and N_y are the number of elements in the discrete Fourier transform, and Δx, and Δy are the pixel sizes, $a_{n,ff}(x,y)$ is the dark subtracted flat field image and $P(x,y)$ is a second degree polynomial fit.

3.3.7 Region of interest size and spectral variance

The size of the region of interest (ROI) is of critical importance because it defines the finite window of the noise data required to provide adequate resolution for proper representation of the NPS, without the finite window overtly affecting the NPS estimate. In general the larger the size of the ROI the lesser the effect of the finite window to estimate the NPS is. Note that in order to accurately estimate the mean value in the ensemble averages and, in general, the NPS we need $N \to \infty$. Thus using a large ROI size we fulfill this requirement. Using a large ROI size, a sinc^2 correction for the finite window width is not necessary as it has a minor effect in NPS estimation. However, the larger the size of the ROI the smaller the number of NPS to average and thus the higher the uncertainty in the spectral estimates will be.

The variance in the final NPS estimate decreases as the square root of the number, n of determinations. Assuming that the variance of using the whole image is equal to one, then by subdividing the image in n smaller ROIs, the variance in the final estimate decreases as:

$$Var = \frac{1.0}{\sqrt{n}} \tag{3.15}$$

Conversely, for a given sampling interval Δx (pixel size) the spectral resolution Δf of the NPS is inversely proportional to the number, n of determinations used to generate each NPS.

$$\Delta f = \frac{1}{\left(\frac{N}{n}\right)\Delta x} = \frac{n}{N\Delta x} \tag{3.16}$$

Because we want high frequency resolution in order to detect all the noise attributes in the system a ROI of 128x128 ROI size is adequate (Williams M. B. *et al* **1999**). In addition, with a ROI size larger than 128 x 128 pixels, the Raw NPS is equal to the True NPS and correction for the finite width of the ROI size is not required. Another practical aspect for the choice of such ROI is related to the small format of the sensors (~ 520 × 520), as a larger ROI would require more images to be used for the ensemble averages, making the NPS measurement more susceptible to exposure fluctuations. Finally, as there is not a deference in using overlapping or non overlapping ROIs (Dobbins J T *et al* 2006) we have chosen to use overlapping ROIs in order to further reduce the variance in the final NPS estimate per frequency.

3.3.8 One dimensional NPS

For a quantitative comparison of different NPS measurements, ease of graphing and computing results for the DQE estimation, a one-dimensional (1D NPS) representation of the NPS is desired. The assumptions for utilizing the 1D NPS are that the 2D NPS exhibit moderate radial symmetry and that the noise data are nominally uniform within the small annuli of spatial frequencies used for regrouping the noise data (Vedantham S *et al* 2000). Many ways have been developed so far in order to extract the 1D NPS from the 2D NPS, as the one-dimensional curve along the u and υ axis does not give very satisfactory results. In Table 3.1 the various methods proposed are presented along with ways to detrend the images for the NPS estimate.

Table 3.1 the various methods proposed are presented along with ways to detrend the images for the NPS estimate

Data averaged	Detrending	Ref.
Both axis w/o axis	1st order ramp	Dobbins et al 1995
Both axis w/o axis	2nd order ramp	Williams et al 1999
Radial averaging	Flat fielding	Granfors et al 2000
Both axis w axis	2nd order ramp	Samei et al 2002
Diagonal direction	2nd order ramp	Samei et al 2003

There are subtle differences in the various ways proposed and they are directly related with the response of the sensor. For example Granfors *et al* 2000 measures the performance under clinical conditions and so flat fielding has been applied. After flat fielding any trends or fixed components in the images are removed, and if the system exhibits radial symmetry radial averaging can be used. However, estimation of the NPS after flat fielding is susceptible to noise correlations and exposure variations. One conflicting point is whether or not to include the x-and y-axis data of the 2D NPS in the extraction of the 1D NPS. The main reason to include the main axis data is to include the low frequency EMI (usually perceived as horizontal stripes) and structured noise that will be present in the final image. This type of noise can be noticeable in the low (EMI) and high (structured) intensity areas of the image. However, these data are not representative in amplitude of the rest of the 2D NPS in the vicinity of the axis and can not be completely removed by detrending. Therefore in order to avoid overestimating the NPS, we have chosen to exclude the data from the axis. In addition diagonal direction averaging can be performed, although it overestimates the low frequency noise component as shown by Samei *et al* 2003 it can be beneficial in avoiding aliased components in the NPS estimate at frequencies close to cut of frequency. In the detectors that we are evaluating the pixel size is reasonably small thus there is no need to use radial averaging. Linear first order ramp as proposed by Dobbins *et al* 1995 is inefficient as the various trends in the image are nonlinear (Williams M B *et al* 1999) thus exclusion of the axis data is necessary. It is evident from the discussion above that the method to extract the data from the 2D NPS is directly related with the detrending method adopted, as well as whether we want to measure the noise of the detector alone or of the imaging system under clinical conditions. Last but not least a smooth spectrum should be achieved irrespective of the method adopted in order to have an accurate estimate of noise amplitude at all frequencies.

Our aim was to measure the performance of the detector. Therefore we used the data in a thick slice, directly adjustment to the axis, comprising eight lines on either side of the axis (excluding the axis), in order to achieve a smoother spectrum. For each (u,v) value in this thick slice the frequency is computed as $\sqrt{(u^2+\upsilon^2)}$ for the one-dimensional plot.

This provided 8 lines x 2sides x 128 frequency bins= 2048 data values that are binned to 0.1 mm^{-1} frequency bins in order to further smooth the spectrum.

In Table 3.2 we present the relevant parameters and corrections used for NPS method employed. The 30 cm distance was dictated by the flux of the tube.

Table 3.2. The parameters and corrections used for NPS method employed

Tube/filtration	Distance	No of images	ROIs and size	Background elimination	Data rows averaged
Mo / 30μmMo/3.8 cm PMMA	30 cm	50	Overlapping(>800) 128 x 128	2-D 2nd order polynomial	8 lines both axis w/o axis

3.3.9 Empirical DQE

The absolute scaling of system performance is greatly facilitated by the introduction of detective quantum efficiency (DQE). For most 2D digital imaging detectors, the DQE is a function of at least three independent variables: its two spatial coordinates and the X-ray exposure. It has been shown (Cunningham I. A. *et al* 1999) that the DQE as a function of frequency, u, of a system can be written as:

$$DQE\left(u,\bar{q}\right)=\frac{SNR_{out}^2}{SNR_{in}^2}=\frac{a_{n,ff}^2 MTF^2\left(u\right)}{\bar{q}NPS_d\left(u\right)} \tag{3.17}$$

where, $\bar{q}$ is the square of the ideal signal to noise ratio (in units of x-ray photons/mm^2). The assumption that an ideal detector behaves as an ideal photon counting detector has been used (Samei E *et al* 2002). In the above equation *NPS(u)* is the raw 1D NPS and $a_{n,ff}$ is the square of the mean signal values of the dark subtracted ROIs.

In the absence of additional noise sources (additive electronic noise) or when those noise sources are very small, DQE is independent of $\bar{q}$ and the system is called quantum limited. The DQE is normalised to express the fraction of input quanta used to create an image at each spatial frequency and describes the ability of a particular system to effectively use all available input quanta. An ideal imaging system has DQE of unity. No system can have DQE greater than unity.

The measured exposure integrated over the normalised spectral distribution was used to determine the X-ray photon flux per unit area (Johns H E *et al* 1983) as follows:

$$\Phi = X\int\frac{\Phi_N^j\left(E\right)}{\left(\frac{\mu_{en}\left(E\right)}{\rho}\right)_{air}\cdot W\cdot E\cdot q_e}dE \tag{3.18}$$

where Φ is the X-ray photon fluence spectrum (quanta/mm^2), X is the exposure in C/kg, $\Phi_N^j(E)$ is the normalised spectrum incident on the detector, $(\mu_{en}(E)/\rho)_{air}$ is the mass energy absorption coefficient of air (m^2/kg), E is the X-ray photon energy (in eV), W is the ionisation energy of air (33.85 eV), and q_e is the electron charge.

3.4. Signal and noise transfer in CMOS APS

The image formation in a CMOS APS can be understood by considering the different stages where the image signal and noise are transferred: charge generation, charge collection and charge measurement (Janesick J *et al.* 2003).

Charge generation is related to the ability of the sensor to intercept impinging photons and create photoelectrons through the photoelectric effect. Consider a number of visible quanta q hit the geometrical pixel area during the exposure time. These photons generate a number of electrons, a process described by the interacting quantum efficiency. The photon generated electrons in the pixel (a_q) can be expressed as:

$$a_q = \frac{E \cdot A \cdot \eta_i \cdot \nu}{h \cdot c} \cdot t \tag{3.19}$$

where E is the irradiance on the sensor (W/m^2), A the area of the pixel (m^2), η_i is the interacting quantum efficiency of the photodiode, ν is the light wavelength, h is the plank's constant, c the speed of light and t is the integration time.

The interacting quantum efficiency represents the fraction of the visible photons interacting with the sensor with respect to the number of photons incident on the sensor. It can be expressed as follows:

$$\eta_i = \frac{InteractedPhotons}{IncidentPhotons} \tag{3.20}$$

The interactive quantum efficiency is the product of the photodiode quantum efficiency and fill factor $(\eta_i = \eta \times FF)$, since the entire area of the sensor is not photosensitive.

Charge collection expresses the ability of the sensor to accurately collect the generated photoelectrons under each pixel. For reasons of simplicity it is assumed that all the photoelectrons are collected. The dark signal (a_d) in the sensor is referenced to the number of electrons in the pixel and added to the photon generated electrons.

The total pixel induced signal (a_{tot}) will be equal to

$$a_{tot} = a_q + a_d = \left(q \cdot \eta_i + \frac{i_D}{q_e} \right) t \qquad (3.21)$$

where q is the average number of quanta incident on the pixel (photons pixel^{-1} sec^{-1}), i_D is the thermally generated dark current (Amp pixel^{-1} sec^{-1}), and q_e is the electron charge (1.60218 x 10^{-19} Coulombs).

The charge measurement is the final and most important function of the sensor. The collected electrons are converted into voltage by means of a capacitor, amplified and finally digitised. The final digital value is related to the number of electrons generated by the overall system gain that describes the number of electrons per digital number (or ADC bit).

In all the above stages, apart from the photon and dark shot noise, there are numerous other sources of noise related with the readout, amplification and digitization that are added to the final signal (Janesick J *et al* 2002). The total noise in the CMOS APS can be expressed as:

$$\sigma_{tot}^2 = \sigma_Q^2 + \sigma_D^2 + \sigma_{RST}^2 + \sigma_{SF}^2 + \sigma_A^2 + \sigma_{ADC}^2 + \sigma_{PFPN}^2 + \sigma_{DFPN}^2 + \sigma_{CFPN}^2 \qquad (3.22)$$

where σ_Q^2 and σ_D^2 are the signal and dark current shot noise, σ_{RST}^2 is the reset noise, σ_{SF}^2 is the RTS and white noise of source follower, σ_A^2 is the amplifier noise, σ_{ADC}^2 is the quantisation noise, σ_{PFPN}^2 is the fixed pattern noise due to pixel-to-pixel variation in sensitivity or photoresponse non-uniformity, σ_{DFPN}^2 is the dark current fixed pattern noise and σ_{CFPN}^2 is the offset differences between pixel and column parallel signal readout. All the noise contributions can be expressed in electrons rms. The fixed pattern noise is the result of non-uniformities in the CMOS process causing small variations in device physical dimensions, and differences in pixel and column voltage thresholds. The first six terms of Eq.3.22 are temporal noise sources. In Figure 3.4 the signal and temporal noise transfer of a single pixel is presented.

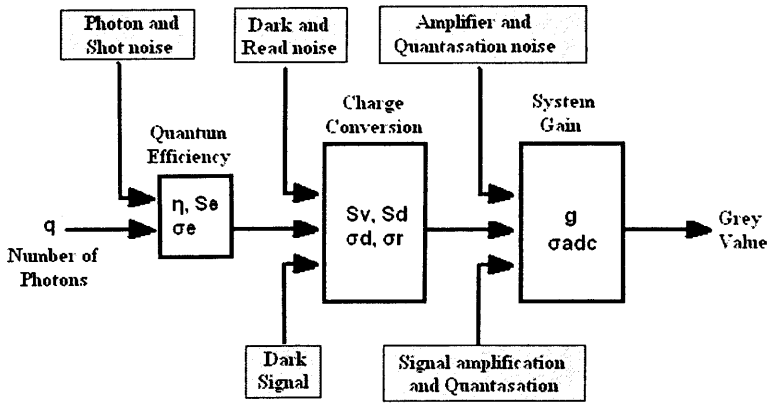

Figure 3.4. Signal transfer diagram of a single pixel with the main sources of signal and noise.

3.4.1. Mathematical model for CMOS APS performance evaluation

Considering the different stages that the image signal and noise are transferred in a CMOS sensor, a mathematical model for the electro-optical evaluation of the CMOS APS can be developed. The CMOS APS can be considered as an LSI system with amplification stages. Stochastic spreading and noise correlations are minimal due to well defined pixel aperture; thus spatial domain analysis is adequate to evaluate its performance. However, a frequency domain analysis can be used in order to gain more insight in the various stages of signal and noise transfer and quantify any noise correlations in the performance of the sensors. For example, nonstationary noise arising from electromagnetic interference (EMI) from the power supply during the read out of the sensor can be examined and quantified.

One way of describing noise is to calculate the variance in measurements of the image signal over a specific region of interest, which has uniform expected value. Noise variance is given as:

$$\sigma_a^2 = E\left\{|\Delta a|^2\right\} \tag{3.23}$$

where $\Delta a = a - E\{a\}$. Units of the variance σ_a^2 are the same as units of the squared signal a^2. The variance is defined in terms of the expected value of $|\Delta a|^2$ and can be obtained from an average of many images at a particular location r. This is called an ensemble average. In practice, it may be necessary to use a spatial average of $|\Delta a|^2$ as an estimate

of the ensemble average. A system for which the ensemble and spatial averages are equivalent is called *ergotic*.

The total mean pixel induced signal $(\bar{a}_n)$ can be expressed in raw digital numbers with the aid of camera gain (g) as:

$$\bar{a}_n = g \cdot \bar{a}_q + g \cdot \bar{a}_d \tag{3.24}$$

where $\bar{a}_q$ is the input signal $(\bar{a}_q = \bar{q} \cdot \eta_i)$ and $\bar{a}_d$ is the dark signal expressed in electrons. In a digital detector, this involves a number of consecutive binomial selection processes (Barrett H H *et al* 1981) the individual gains (i-1, i, i+1...i+n) can be equivalently represented as a single stage, i, with mean gain given by a linear combination of the individual gains,

$$\overline{g_i} = \prod_{k=0}^{n} \bar{g}_{i+k} \tag{3.25}$$

The average conversion gain of detected electrons to raw digital numbers (DN) generated by the ADC can be determined by measuring the noise variance in the mean observed signal (Rabbani M *et al* 1987),

$$\sigma_a^2(x,y) = \bar{g}^2 \sigma_q^2(x,y) + \sigma_g^2 \bar{q}(x,y) + \sigma_{add}^2(x,y) \tag{3.26}$$

where σ_a^2 is the noise variance of the mean detector signal, x and y are the spatial coordinates, σ_g^2 is the variance of the camera gain, and σ_q^2 is the input signal variance. σ_{add}^2 is the system total additive noise variance expressed in digital numbers and has been added to the equation since it is independent (uncorrelated). $\bar{g}$ is the mean camera gain (DN/e^-) and $\bar{q}$ is the average input signal. In the case of a linear $(a_d = 0)$ and shift invariant detector ($\sigma_g^2 << 1$) an input signal of $\bar{a}_q$ quanta per pixel will produce an output mean signal $\bar{\alpha}_n = \bar{g} \cdot \bar{a}_q$. If the input quanta are governed by Poisson statistics ($\sigma_q^2 = \bar{a}_q$), and the camera gain variance is very small with respect to the mean camera gain the additive noise sources can be removed (σ_{add}^2) and Eq. 3.26 reduces to:

$$\bar{g}'_n\left(e^- / DN\right) = \frac{\bar{\alpha}_q\left(DN\right)}{\bar{\sigma}_q\left(DN\right)^2} \tag{3.27}$$

where $\bar{g}'_n = 1/\bar{g}_n$ and the signal α_q and signal shot noise σ_q are expressed in digital numbers (DN). Using Eq. 3.27, the relative digital signal generated by the on-chip ADC of a digital camera, expressed in raw digital numbers (DN) is converted to absolute electron units through the camera gain constant.

3.4.2. Photon Transfer Curve

The various noise sources in CMOS active pixel sensors mentioned above can be grouped as photon shot noise, read noise and FPN sources and quantified through the photon transfer curve (PTC). The overall mean system gain $\bar{g}$ can be computed as follows:

$$\bar{g}\left(DN / e^-\right) = \frac{1}{\bar{g}'\left(e^- / DN\right)} = \frac{\bar{\sigma}^2_{n,temp} - \bar{\sigma}^2_{d,temp}}{\bar{\alpha}_q - \bar{\alpha}_d} \tag{3.28}$$

where $\bar{\sigma}^2_{n,temp}$ a and $\bar{\sigma}^2_{d,temp}$ are the signal and detector temporal noises. $\bar{\alpha}_n$ and $\bar{\alpha}_d$ are the signal and dark reference signals or offset signal. All the above quantities are expressed in raw digital numbers (or gray values). Eq. 3.28 is equivalent to Eq. 3.27 and describes the linear correspondence of noise versus signal. Plotting the noise versus signal at different pixel intensities the camera gain can be measured from the slope of the plot. It is interesting to remind that the above expression for the camera gain measurement can be used only when the detector is linear (or linearasable). In order to isolate the temporal noise sources, fixed pattern noise (FPN) has to be removed. The most effective removal of FPN noise is by subtracting two consecutive frames where any fixed noise component is removed. Note that the process of subtraction doubles the noise in the image thus in order to measure the r.m.s. noise of the system division with $\sqrt{2}$ is necessary.

3.4.3. CMOS Nonlinearity

In CMOS sensors there are two fundamental properties that create nonlinearities in the response of the sensor. Such deviations from linear response appear due to the change in capacitance as the diode discharges (Janesick J *et al* 2006) and due to intrinsic non-

linearity of the source follower. Usually the gain nonlinearity (V/V) of the source follower input transistor is very small and can be neglected. However, the sensitivity nonlinearity (V/e$^-$), especially in 3T CMOS APS can be considerable where the photodiode is an element of the sense node. This causes its capacitance to change during charge integration leading to significant deviations from linearity, as is explained below.

The relationships linking V/e$^-$ signal and noise, sense capacitance, charge, voltage and resultant nonlinearity are all related through the differential equation

$$C_{SN}(V_{SN}) = q\frac{dS(e^-)}{dV_{SN}} \tag{3.29}$$

where $C_{SN}(V_{SN})$ is the sense node capacitance that varies with sense node voltage dV_{SN}, $S(e^-)$ is the sense node charge and q the electron charge. Depending on sense node capacitance C_{SN}, the sense node sensitivity $S_{SN}(V_{SN}/e^-)$ is related through the integral of Eq. 29 as:

$$S(e^-) = \frac{1}{q}\int_{V_{Ref}}^{V_{SN}} C_{SN}(V_{SN})\,dV_{SN} \tag{3.30}$$

where V_{Ref} is the sense node voltage after reset. The sense node noise sensitivity $N_{SN}(V_{SN}/e^-)$ is connected to the sense capacitance as:

$$N_{SN}(V_{SN}/e^-) = \frac{q}{C_{SN}(V_{SN})} \tag{3.31}$$

In CMOS C_{SN} always increases as the diode charges causing $S_{SN}(V_{SN}/e^-) < N_{SN}(V_{SN}/e^-)$.

In the measurement of the camera performance parameters those nonlinearities have to be corrected otherwise an erroneous estimation of the performance of the sensor will be performed. The C_{SN} variation in most cases starts after a reasonable amount of charge has been integrated from the photodiode. Thus beyond this level, the sensor response should be corrected in order to accurately determine its performance. This correction is straight forward using the linearity data of the sensor, by assuming that the signal continues to have the same proportionality to the light level as before the nonlinearities

become observable. After the correction has been applied the conversion gain throughout the entire dynamic range of the sensor are equivalent $\overline{g'}(e^- / DN) = N(e^- / DN) = S(e^- / DN)$.

3.4.4. Camera performance parameters

With the aid of the photon transfer curve most of the critical performance parameters of the sensor can be measured in absolute units. The total additive electronic noise $(\sigma_{e,tot})$ and the full well capacity (FW_e) can be measured as follows:

$$\sigma_{e,tot} = \sigma_{n,temp} \cdot N(e^- / DN) \tag{3.32}$$

and

$$FW_e = \overline{\alpha}_{q,sat} \cdot S(e^- / DN) \tag{3.33}$$

where $\alpha_{n,sat}$ is the signal level expressed in digital numbers at the maximum pixel variance $(\overline{\sigma}_{s,temp,\max})$. The sensor dynamic range is defined as the ratio of full well capacity to total additive electronic noise. The most important noise component in CMOS APS is the reset noise. Once the capacitance of the sensor after reset is measured through Eq. 3.31 the reset noise can found from

$$\sigma_{rst} = \frac{kTC^{1/2}}{q} \tag{3.34}$$

For an ideal ADC the quantizing noise is given by:

$$\sigma_{ADC} = \frac{\overline{g'}(e^- / DN)}{12^{1/2}} \tag{3.35}$$

Note that the quantizing noise can be negligible if the camera gain constant is set to be at least equal to the read noise floor.

The nonlinearity of the sensor can be measured from the integral nonlinearity expressed as:

$$Int.Nonlinearity = \frac{\sqrt{\left((b \cdot \overline{q} + c) - \overline{a}_q\right)^2}}{\overline{\alpha}_{q,sat}} \tag{3.36}$$

where, $b\cdot\bar{q}+c$ is the linear fit of the linearity data with $\bar{q}$ the average number of optical quanta per pixel per integration time, $\bar{a}_q$ is the pixel value after the nonlinearity appears and $\bar{\alpha}_{q,sat}$ is the pixel value at full well.

3.4.5. Dark current curve

The dark current expresses the amount of thermally generated electrons on the sensor in the absence of irradiation. This signal component forms an offset signal in the detector and ads shot noise in the actual signal. It is related to the operational temperature of the sensor and can be measured using the dark current curve by varying the integration time at constant temperature. It can be computed according to the mathematical model as:

$$i_d = \frac{\bar{\alpha}_d(DN)\bar{g'}(e^-/DN)\cdot q_e}{A\cdot t} \tag{3.37}$$

where i_d is the dark current (A/cm^2) $\bar{\alpha}_d(DN)$ is the mean dark signal at different integration times, t is the integration time, $\bar{g}'(e^-/DN)$ is the mean camera gain, A is the pixel area (in cm^2), and q_e is the electron charge.

3.4.6. Interacting Quantum efficiency

The interacting quantum efficiency as a function of wavelength (λ) can be measured through the use of camera gain constant and raw data from the sensor as follows:

$$\eta_I(\lambda) = \left(\frac{1}{M}\sum_{m=1}^{M}\sum_{x=1}^{N}\sum_{y=1}^{N}\alpha_{n,x,y}(\lambda) - \alpha_{d,x,y}\right)\times\bar{g'}\times\frac{\eta_{PD}(\lambda)\times q_e}{i_{PD}(\lambda)\times t} \tag{3.38}$$

where α_n is the pixel signal in digital numbers, α_d is the offset signal responsible for dark current and small variations of the detector from the base line, M is the number of images used and x, y the number of pixels used to measure the signal in the sensor. $\bar{g'}$ is the camera gain constant (e$^-$/DN), η_{PD} is the quantum efficiency of a calibrated reference photodiode, i_{PD} is the reference photodiode photocurrent (Amperes), t is the integration time of the sensor (seconds), and q_e is the electron charge. The last terms in

Eq. 3.38 account for the conversion of the photodiode photocurrent to photons per integration time.

3.5. Summary

In this chapter the theoretical framework of signal and noise transfer of digital X-ray imagers and CMOS APS has been presented. Within this framework a complete X-ray and electro-optical performance evaluation of the imagers can be performed. Along with the computational methods to measure the performance of the X-ray imagers, deviations from the theoretical framework due to the discrete nature of digital systems have been also presented. Ways to take explicitly into account these deviations and to conduct relevant corrections has been presented. For reasons of clarity, the CMOS sensor has been treated as separate element of the X-ray imager and its signal and noise transfer properties have been analyzed separately. A detailed description of ways to compute its performance parameters has also been presented. Implementation of the analysis presented provides the means to evaluate, optimise and calibrate the sensors presented in order to gain insight in the CMOS APS sensor technology and determine in absolute units whether this detector technology is suitable for conventional and quantitative contrast enhanced mammography.

Chapter 4

Electro-optical and X-ray Performance Evaluation of the Imagers

4.1. Overview

In this chapter the elector-optical performance evaluation of the three CMOS APS employed in this study is presented. The electro-optical performance of the sensors has been measured in terms of linearity, cross talk, read noise, fixed pattern noise, full well, dark current and interacting quantum efficiency. The physical characteristics (MTF NPS and DQE) of the imagers are also presented.

4.2 Materials and Methods

4.2.1. Electro-optical performance evaluation of the CMOS APS

The linearity data were generated by varying the light intensity of a uniformly irradiated 100 x 100 pixel region of the sensor from dark until saturation. Uniform irradiation has been achieved by placing a diffuser in front of an LED. Using a diffuser with 20% transmission and placing the detectors at a distance higher than 50 cm from the light source more than 99% uniformity in the irradiation at the entire detector's surface was achieved. The uniformity was measured by scanning a photodiode in the X and Y direction at the detectors plane. Note that if detectors with larger dimensions are used it is likely that a longer distance between the light source and the detector will be required. In the linearity plot the x-axis is the number of photons incident on the sensor per integration time per pixel as it was measured by a calibrated photodiode (Si photodiode, S1336-44BQ, Hamamatsu) and the last term of Eq. 3.38 multiplied by the ratio of pixel size to photosensitive area of the photodiode. The y-axis is the mean pixel signal in the uniform irradiated region of 100 x 100 pixels. The signal has been converted to absolute units after the camera gain constant has been determined.

In order to investigate the geometrical charge collection efficiency and the pixels cross-talk, a 1060 nm wavelength semiconductor pigtail fibre laser beam with a focused

light spot diameter of 7 μm was used to illuminate the imager. The fibre laser was operated in pulse mode with pulse frequency, duty cycle and amplitude controllable. PC controlled X-Y step motor stages were used to move the sensor in X and Y directions, which allows the laser spot scanning over the sensor surface. This yielded the laser map image of the imager at 0.69 μm resolution, representing the charge collection efficiency across the array. A 3 μm/step was used to measure the pixel cross talk with the laser spot scanning in the X and Y direction along the centre of the pixel.

The photon transfer curve data are generated by varying the light intensity of a uniformly irradiated 100 x 100 pixel region of the sensor from dark until saturation. The r.m.s. noise as a function of pixel signal is plotted logarithmically in the PTC. Isolation of each noise component can be performed by successively removing from the total noise each of the major noise sources (Chapter 3 section 3.4.2). The dark current transfer (DTC) can be generated in similar way as the PTC but instead of varying the light intensity, the integration time is varied. When generating the DTC data one has to make sure that the sensor is placed in a light tight box.

The interacting quantum efficiency has been measured according to Eq. 3.38. The dark current was removed using the offset signal which has been extracted from an equal size region of image immediately adjacent to the irradiated region. The calibrated photodiode used for the linearity measurements has been used to measure the incident photons on the sensor. A monochromator (H20 series, JYHoriba) with 0.25 nm reproducibility was connected to a stable light source (UV-Visible fibre light source L7893 series, Hamamatsu) to produce monochromatic light at different wavelengths. A fibre optic from the monochromator was used to guide the light directly to the surface of sensor as well as to the photodiode.

4.2.2. Empirical physical characteristics of the X-ray imager

A prototype micro focus X-ray tube (X-Tek systems Ltd) with Mo target and 30μm Mo filter combination was employed for the X-ray performance evaluation. Although this X-ray tube is not used in clinical mammography, it provided a mammographic spectrum to evaluate the sensor in the mammographic energy range. In addition, due to its small focal spot, high tube loads could not been achieved so in order to have sufficient flux the

tube was set at 30 kVp for all the measurements presented. Discussion of the effects of the tube voltage is given where appropriate. For the NPS measurements the X-ray beam was hardened by 3.8 cm of poly(methylmethacrylate) (PMMA), which was placed close to the tube, in order to eliminate scatter photons reaching the detector.

The exposure was measured with a calibrated ion chamber (KEITHLEY 35050A Dosimeter) placed between the X-ray tube and the sensor and corrected with the inverse square law. The measured exposure integrated over the normalized spectral distribution was used to determine the X-ray photon flux per unit area (Eq. 3.18). In Figure 4.1 the normalised spectrum incident on the detector is presented. The spectrum of the X-ray tube has been measured using high purity germanium detector (HPGe Ortek). Low X-ray photon flux has been employed to avoid pile up; no correction was necessary due to the high quantum efficiency (~100 %) of the detector in this energy range. The spectrum was measured without the PMMA present, thus for the photon fluence measurements the spectral distribution was provided by attenuating the spectrum with 3.8 cm PMMA using tabulated attenuation coefficients (Berger M J *et al* 1999).

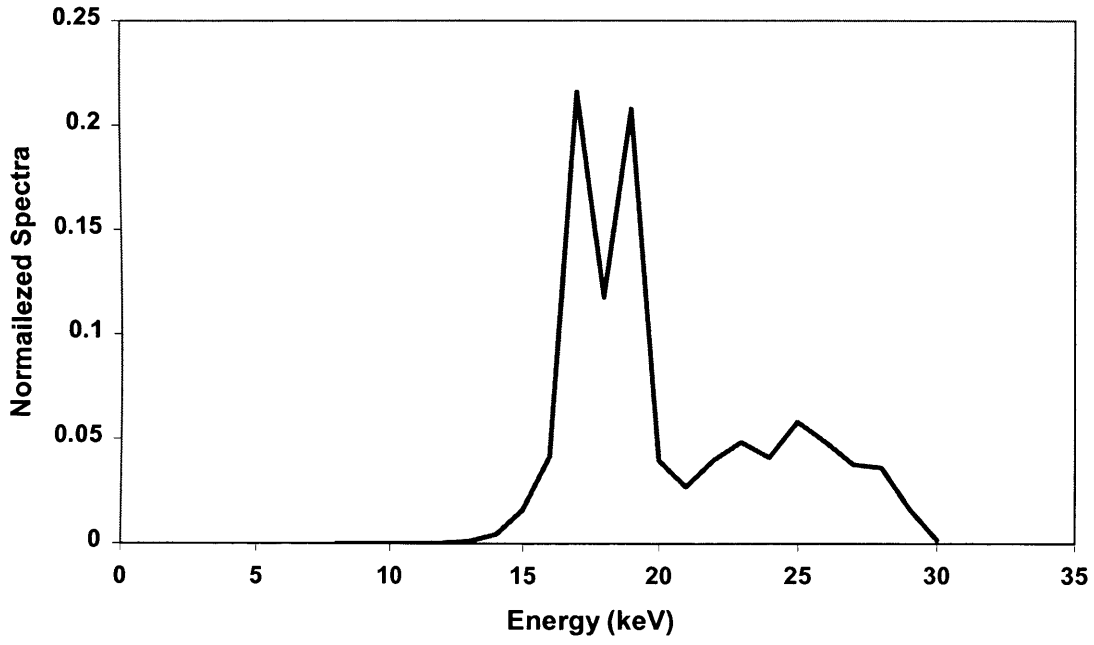

Figure 4.1. Normalized Mo spectra used for the NPS measurements and the determination of the DQE.

Four CsI:Tl (from now on referred to as CsI) phosphors from different vendors with columnar structure have been employed for the X-ray measurements. From the first vendor (Hamamatsu) two CsI phosphors were provided. One was optimized for high sensitivity (HS) and the other for high resolution (HR). Their physical dimensions were 18 mm x 18 mm with thickness 150 μm. A 3 mm thick fibre optic plate (FOP) was used as a substrate in these phosphors. From the second vendor (Applied Scintillation Technologies-AST) came the other two CsI phosphors. Their physical dimensions were 18 mm x 18 mm with thicknesses of 95 μm and 115 μm respectively. For both phosphors the back reflectivity (X-ray entrance) was 70% as provided by the manufacturer (AST). A 1 mm thick fibre optic plate (FOP) was used as a substrate in these phosphors. An optical gel with 1.52 refractive index has been used for the optical coupling of the phosphors FOPs with the sensors. The 3T APS sensor bonding wires did not allow coupling the X-ray converters directly to the sensor as they had larger physical dimensions than the chip size, so another FOP 5 mm thick with 75% transmission was glued to the 3T APS sensor. The glue that coupled the FOP with the sensor was approximately 5 microns thick. The 3T APS was coupled with the 95 μm and 115 μm CsI, resulting in two different system configurations. The Vanilla was coupled with the 150 μm HS and HR CsI and the 115 μm CsI resulting in three different system configurations.

The X-ray sensitivity of the sensors has been measured within the exposure range of 0.05 μC/kg to 0.7 μC/kg for the Vanilla system configurations and from 0.7 to 13 μC/kg for the 3T APS system configurations. The range of exposures used has been dictated by the difference in the systems' sensitivity and their range of linearity. As will be shown later, the 3T APS has longer range of linearity and its sensitivity is half of the Vanilla, thus higher exposures were required. The mean pixel signal has been measured from a small (50 × 50 pixels) area of the sensor and converted to absolute units through the camera gain constant. The X-ray gain of the system was measured from the linear fits of the number of electrons generated per pixel as a function of X-ray photons incident on the sensor per pixel. The determination of the X-ray photon flux per unit area from the measured exposure was performed as described above. The images have been dark field subtracted and flat field corrected.

For the MTF measurements the X-ray tube was filtered only with the 30 μm Mo. The presampling MTF was obtained by the Fast Fourier Transform (FFT) of the oversampled line spread function (LSF) as described in Chapter 3. The slit used was 10 μm (± 1 μm) width by 5.5 mm in a 1.5 mm thick tantalum disk (MA4976, Gammex rmi). The angle of the slit with respect to the detector pixel matrix was approximately 2^0. The slit images were corrected for sensor offset and phosphor spatial gain.

For the determination of the NPS, the raw data was used as they were provided from the on chip analog-to-digital converter (ADCs) that incorporates all the noise components of the system. The two dimensional noise power spectra (NPS) were measured using a 128 × 128 region of a flat field image from the two different sensors. The pixel values expressed in relative digital numbers (DN) have been converted to electrons with the aid of camera gain constant. The expression of the 1-D NPS in absolute units (e^2 mm^2) can be used to express the noise of the system as absolute spectral density (ASD). This can be very useful because apart from expressing the noise in absolute terms, it can be used to evaluate in absolute units the effect on the NPS estimate of the various corrections employed. Offset and background trends such as heel effect, were removed by means of dark and ROI surface fitted subtraction, as explained in Chapter 3. The noise power spectrum of the electronic noise has been determined with the same approach but without ROI surface fitting. No other processing of the data was performed as there where no dead lines or pixels on the sensors.

The detection quantum efficiency (DQE) was measured according to the empirical equation Eq. 3.17. The MTF data used for the measurement of the DQE were provided by linear interpolation of the experimental data. The exposure range used to measure the DQE was 0.05 μC/kg to 0.7 μC/kg for the Vanilla system configurations and 0.44 μC/kg for the 3T APS system configurations. Due to low flux of the tube, DQE measurements at higher detector entrance exposures were not possible.

4.2.3 Experimental precision

In the photon transfer curve, the measurement of the camera gain uncertainty is given by $\sqrt{2/N}$, were N is the number of pixels used and for the 100 by 100 region used provided 0.014 uncertainty. For the interacting quantum efficiency 5 images for each

wavelength have been acquired. The size of the region of the image used to integrate the generated photocharge varied between 80 by 80 to 280 by 280 pixels, with no significant difference observed. This provided, in total, 25 points in each wavelength. The maximum uncertainty in the interacting quantum efficiency measurements was 0.53%

For the MTF measurements the slit was placed 2 mm in front of the detector (due to the size of the slit and detector housing), providing slit magnification of less than 1.008 and giving minimal focal spot blurring. Several MTFs from each detector configuration were averaged to improve accuracy. For the NPS measurements 128 × 128 overlapping ROI's from 50 images were used, providing more than 1000 ROI's. The final NPS was the ensemble of 1000 spectra resulting in less than 2.0% standard error.

For the photon flux measurements, 10 exposure measurements in free air were acquired and averaged to improve precision and, including the precision of the ion chamber as provided by the manufacturer, the overall uncertainty in exposure measurements was less than 1%. In all signal measurements a 100 by 100 region of image has been used, and the error was measured as standard errors of the individual pixel values from the mean signal. Error bars in the figures indicate the experimental precision, unless the size is too small to be visible.

4.3 Results and discussion

4.3.1. Electro-optical performance evaluation of the CMOS APS

4.3.1.1. Linearity

The linearity data of the 3T APS (Fig. 4.2) have been fitted up to $6x10^4$ electrons (60% of full well capacity) with a linear regression. After that point, deviations of the sensor from linearity started to appear and have been excluded from the fit. The linearity data of the Vanilla sensor (Fig. 4.3) have been fitted up to $2x10^4$ electrons (35% of full well capacity) with a linear regression. After that point deviations of the sensor from linearity started to appear and have been excluded from the fit. The origin of these deviations have been explained in chapter 3 section 3.4.3 and appear due to the change in capacitance as the diode discharges (Janesick J *et al* 2006) as well as in intrinsic non-linearity of the source follower.

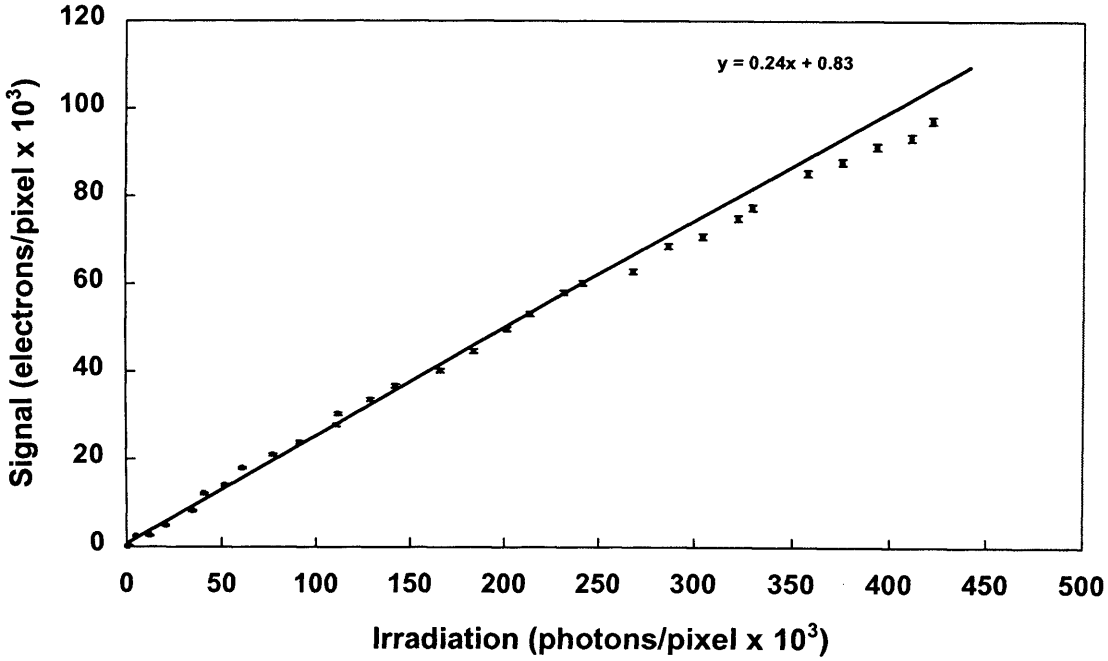

Figure 4.2. Linearity plot of the 3T APS expressed in absolute units normalised to pixel size and integration time. The correlation coefficient of the fit was 0.99 with the data up to $6x10^4$ electrons signal. The light wavelength was 640 nm ± 10 nm.

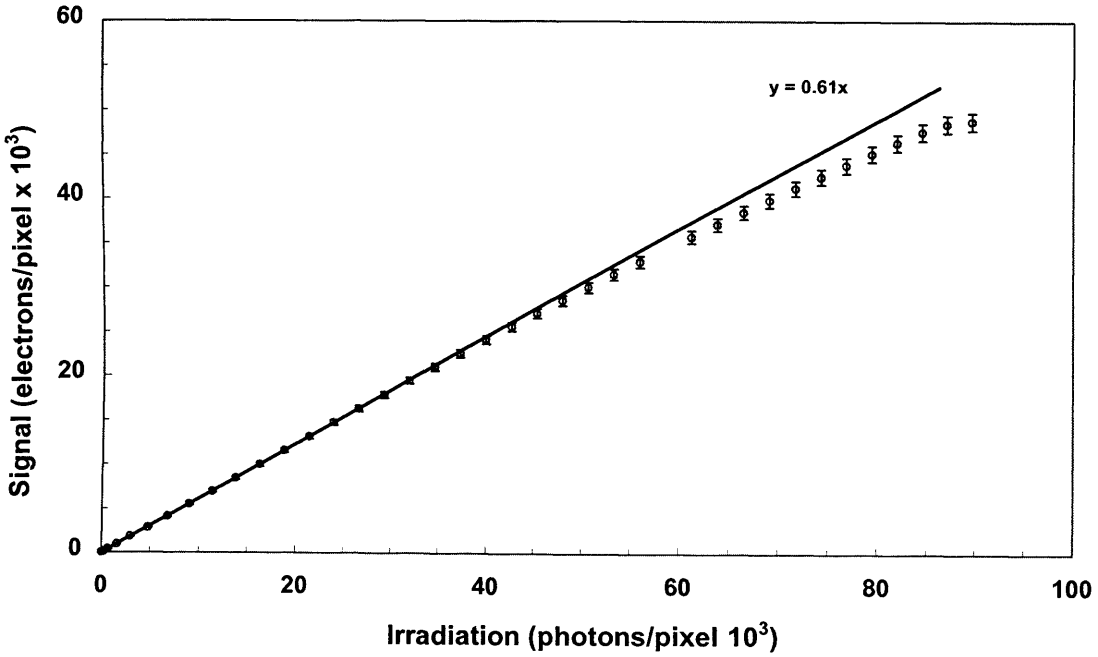

Figure 4.3. Linearity plot of the Vanilla expressed in absolute units normalised to pixel size and integration time. The correlation coefficient of the fit was 0.99 with the data up to $2x10^4$ electrons signal. The light wavelength was 520 nm ± 10 nm.

The linear regressions were used to correct the sensor for deviations from linearity and measure the full well of the sensor. The slope of these curves is equivalent to the interacting quantum efficiency at the peak wavelength of the LEDs.

4.3.1.2. Integral Non-linearity

In Figure 4.4 the integral nonlinearity (Eq. 3.36) of the 3T APS and Vanilla sensors is presented. From the plot it is evident that the Vanilla sensor exhibits much greater nonlinearity than the 3T APS, where a small but constant trend towards higher integrated charge is observed.

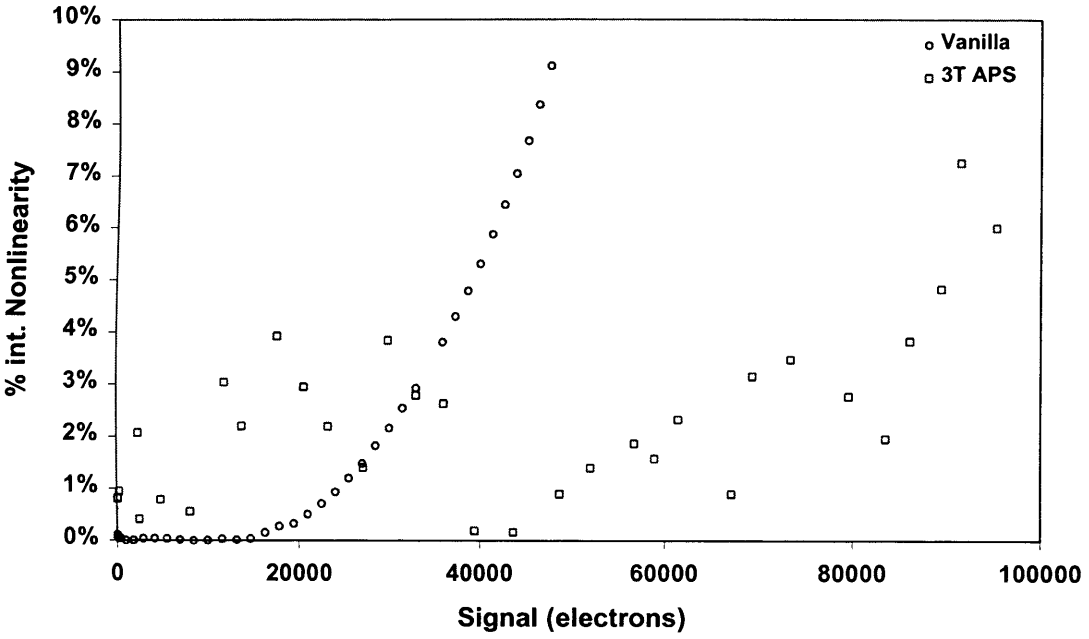

Figure 4.4. Integral nonlinearity plot of the 3T APS and Vanilla sensors.

Janesick *et al* 2006 has proved, by simulating the photodiode's depletion region as a function of accumulated charge that this nonlinearity is fundamental property of MAPS and starts at 10^4 electrons irrespective of CMOS foundry or pixel architecture. It originates from the breakdown of the depletion region of the photodiode. The simulation has been performed on a pixel with one photodiode. Those observations are confirmed with the Vanilla sensor that has one photodiode per pixel. On the contrary, the 3T APS presented here, because it incorporates 4 photodiodes per pixel the nonlinearity starts to

appear almost at 4 times higher signal. This is a very important observation indicating that linear response at high levels of photocharge could be obtained using APS sensors when employing more than one photodiode per pixel. The 3T APS sensor exhibits roughly 2% nonlinearity irrespective of accumulated charge due to grounding problems. However, these problems can be eliminated with more careful design and are not fundamental limitations of the sensor.

4.3.1.3. Cross talk and laser mapping measurements

The charge collection efficiency depends on the position where the carriers were initially generated. When electrons are generated close to the pixel edge or below the pixel but deep in the epi-layer, those photocarriers could diffuse and be collected by neighbouring pixels. This phenomenon, where a photocarrier generated under one pixel and through diffusion, is assigned to a neighbouring pixel is called "cross talk". The 3T APS has pixels with 25 μm pitch; at the boundary of the pixels there is a region of approximately 3 μm covered with the metal. All the pixels are on the same Si substrate.

Figure 4.5(a) shows the detailed response distribution of a central pixel of the imager (25 × 25 μm^2 area). The pixel shows uniform response at the centre and gradually falls off at the edges. The lowest response regions are located in the 4 corners of the pixel. The response mapping image also shows some asymmetries in X and Y direction due to the fine structures of the pixel (readout lines and transistors) indicating low charge collection efficiency at the corners of the imager. Figure 4.5(b) shows the pixel outputs normalised to unity when the laser spot is scanning along the row and column direction across the centre of the pixels. In both directions the output of the pixel is close to a Gaussian line shape with a FWHM of 19.8 μm in row direction. The diameter of the laser spot was ~7 μm, so the FWHM of 19.8 μm is dominated by the pixel size of 25 μm and carrier transfer properties, which also reflects the spatial resolution of the imager. The output decreased to ~5 % of the peak value at the centre of the neighbouring pixel. Therefore, pixel cross talk could be estimated to be ~5 %. Summation over the outputs of 5 neighbouring pixels along row direction gives the total response of the imager along this scanning line. The 5 pixels summation reaches a maximum at the central positions of the pixels, and had a ~15 % dip in the gaps between pixels. The results along column

direction are similar to those of scanning in row direction, with a smaller FWHM of 18.6 μm and a larger dip 18 %. These differences could be ascribed to the asymmetry of the pixels.

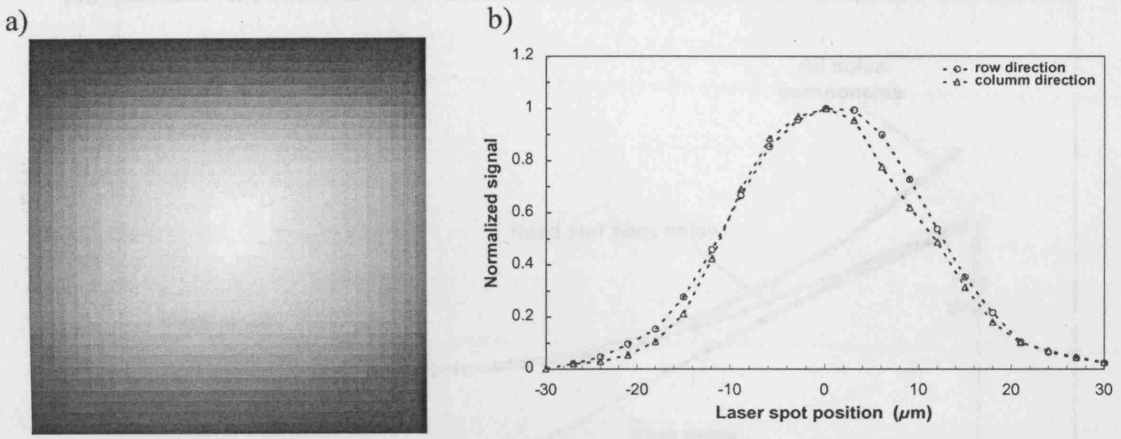

Figure 4.5. (a) The laser spot scan in row (Horizontal) and column (Vertical) direction with 0.69 μm/step (area 25×25 μm^2). (b) The laser spot scan along row and column direction with 3 μm/step.

4.3.1.4. Photon Transfer Curve

The PTC of the Vanilla sensor is displayed in Figure 4.6. The three noise curves presented are A) all noise components that incorporate read, shot, and fixed pattern noise, B) read and shot noise and C) shot noise. The third curve is used to extract the camera gain constant and should have a slope of ½ if the camera is operating under shot noise limited conditions. This indicates that the optimum sensor parameters have been found and read and FPN have been effectively removed. Three regions can be identified in the curve that contains all noise components. The first region, with zero slope is dominated by read noise. The second with slope of ½, is dominated by shot noise from the signal and sensor electronics. At higher signal levels, the slope is ~1 where the fixed pattern noise is the dominant noise component of the signal and increases linearly with the signal.

The read noise and full well capacity are converted from relative digital numbers to absolute units of electrons after measuring the camera gain constant (e^-/DN). The camera gain constant is measured at the intersection of the shot limited curve with x-axis (σ_{SN}=1). It is important to note that the PTC curve can be effectively used to optimize

the sensor. Optimum performance is achieved when the shot noise curve has a slope equal to 0.5. This curve was used to optimize the ADC voltage step by limiting the range that it ramps to maximum achievable pixel variance.

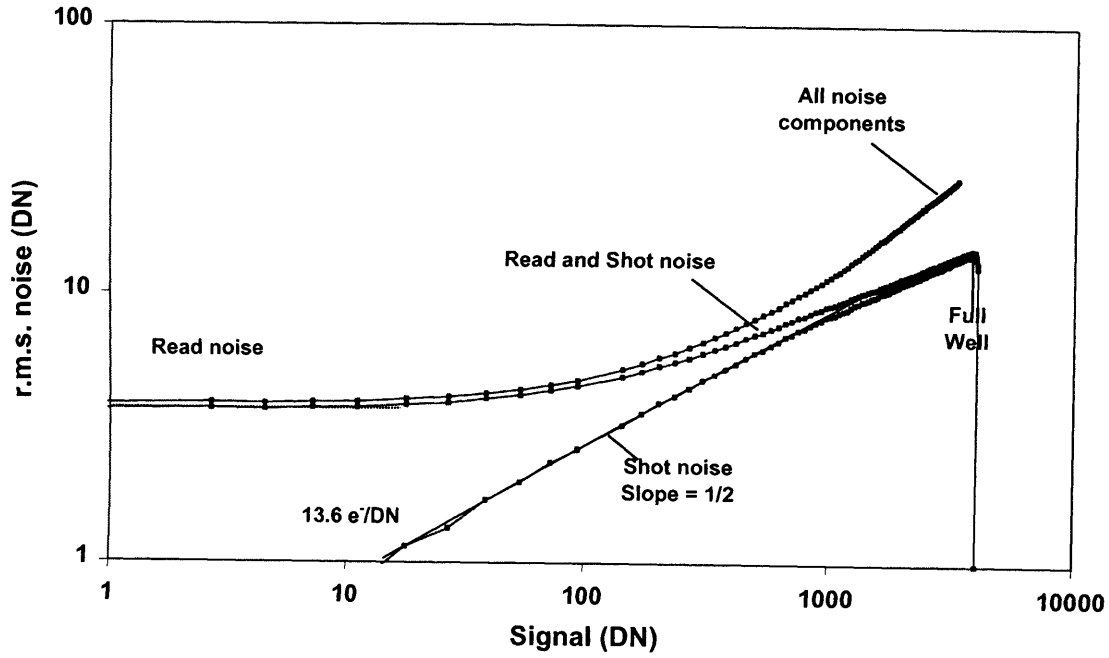

Figure 4.6. The photon transfer curve of the Vanilla sensor.

In Figure 4.7 comparison of the PTC for the two sensors operated under hard reset is presented. The 3T APS has double the read noise of Vanilla and higher full well capacity. Signal-to-noise ratio (SNR) and dynamic range (DR) can be measured using the signal and the r.m.s. noise from the shot noise limited curve (Eqs. 3.32, 3.33). The data have been extracted from the PTC after it has been corrected from nonlinearities. It is interesting to note that the FPGA based DAQ of the Vanilla sensor, due to imperfections of the clocking and biasing of the board as well as some bugs in the embedded firmware, resulted in improper readout of approximately 1% of the pixels. Those pixel values appear to be abnormally low with respect of the rest of the pixel values and were nonstationary in nature. Those "affected" pixel values are not representative of the sensor properties and will inflate the noise estimates especially at higher irradiation levels. If they are not removed they can lead to a false estimation of camera gain and noise through the PTC technique. For the evaluation of the sensor performance these pixel values have

been removed using an algorithm developed for this purpose. This algorithm scanned the entire sensor (or the ROI of the sensor used for the measurements) and when an affected pixel value was found it was removed by applying a median filtering. As "affected" pixel values has been assigned these pixel values that had unreasonably low and nonstationary response.

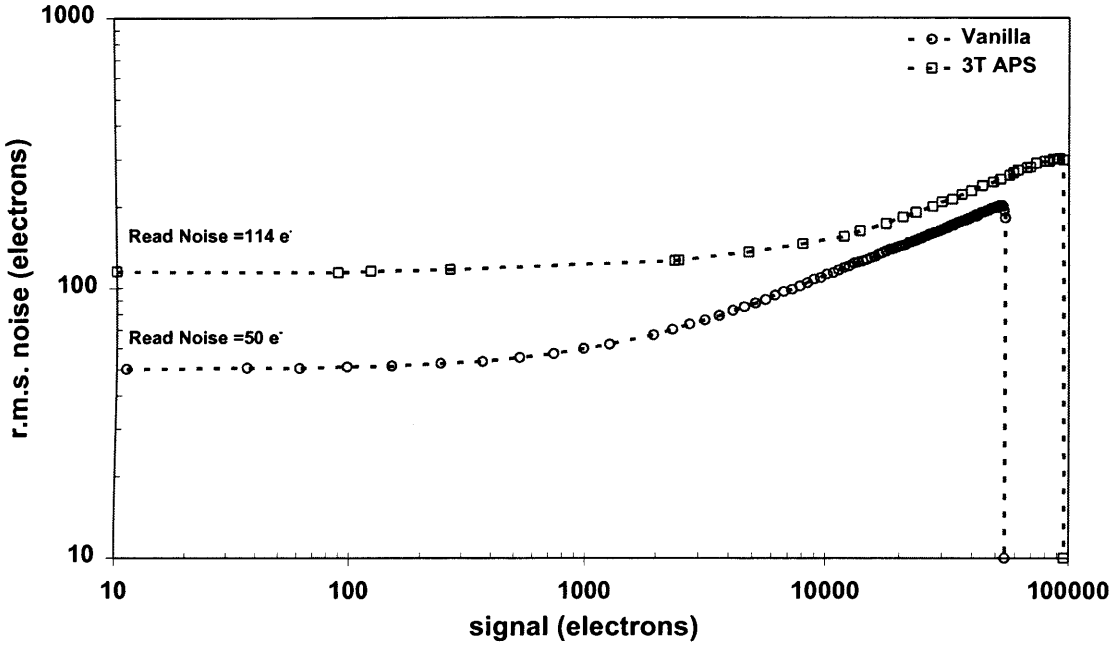

Figure 4.7. Comparison of the 3T APS and Vanilla sensor operated under hard reset.

4.3.1.5. Read noise histogram

The PTC data presented above have been extracted from a region (100 pixels x100 pixels) of the sensors. A more precise measurement representative of the entire sensor can be performed if a small 20 x 20 pixel region is used and scanned over the entire sensor. A histogram representing the variation of read noise (or camera gain) across the array can be created. This approach can be very useful if the sensor has areas that do not respond in the same way, and for large area sensors where process related imperfections may degrade the performance of the sensor at its borders. In Figure 4.8 the read noise histogram of the entire area of the Vanilla sensor is shown. As can be seen, the sensor has moderate symmetry around 51 electrons which, within experimental precision, is equivalent to the mean noise measured by the PTC method (Fig. 4.7). The most important

aspect of this method to estimate the read noise is to find whether the histogram is skewed or not. If the sensor does not exhibit symmetry then there is degradation in its response across the array. This type of degradation is usually found in APS sensors at the edges of the wafer.

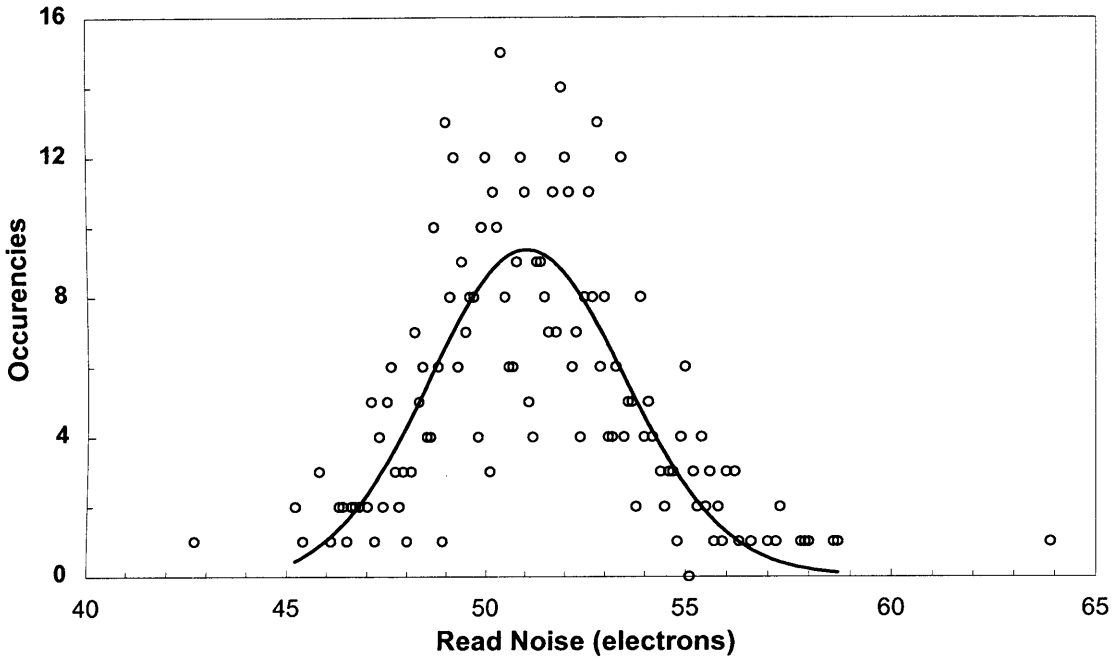

Figure 4.8. The read noise histogram of the Vanilla sensor. The mean of the Gaussian fit was 51 and the sigma 2.5.

4.3.1.6. Vanilla flush reset super-linearity

The Vanilla sensor is able to perform different modes of operation in order to reduce the kTC noise. To achieve this, an extra reset circuit was added off-pixel in order to perform flush reset and achieve low noise without limiting the quantum efficiency and dark current performance of the sensor. In Figure 4.9 the linearity plot of the Vanilla under 'flush' reset is shown. As can be seen the sensor exhibits "super-linearity". In order to further investigate this response of the sensor the photon transfer curve has been generated and is presented in Figure 4.10.

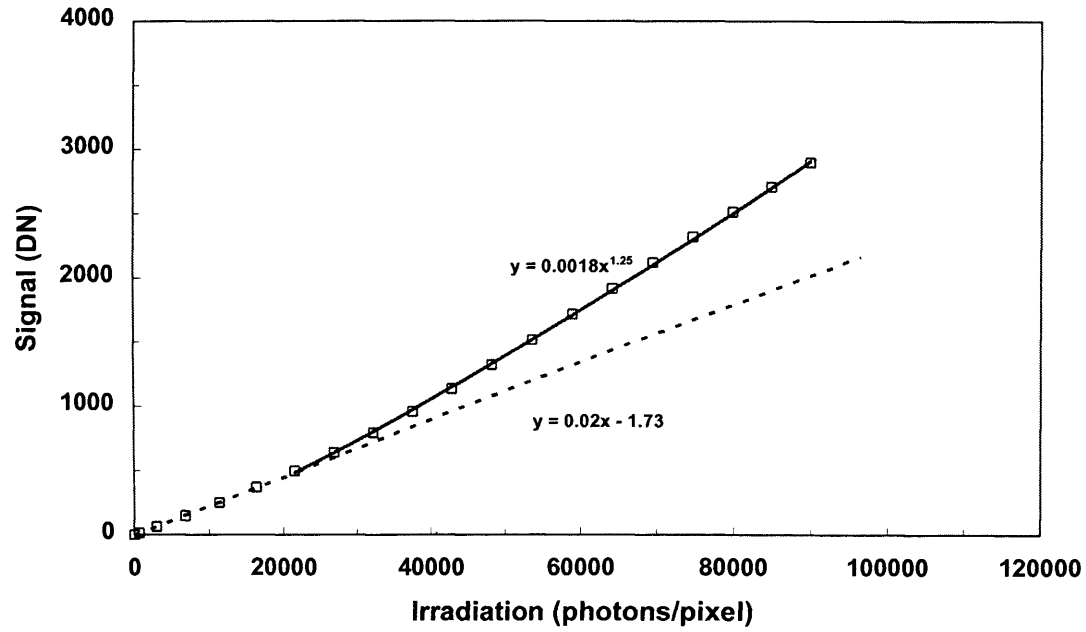

Figure 4.9. Linearity plot of the Vanilla under "flash" reset operation. The data have been fitted with a linear regression up to 500 DN and with an exponential curve above 500 DN. The correlation coefficient of the fits was 0.99 with the data.

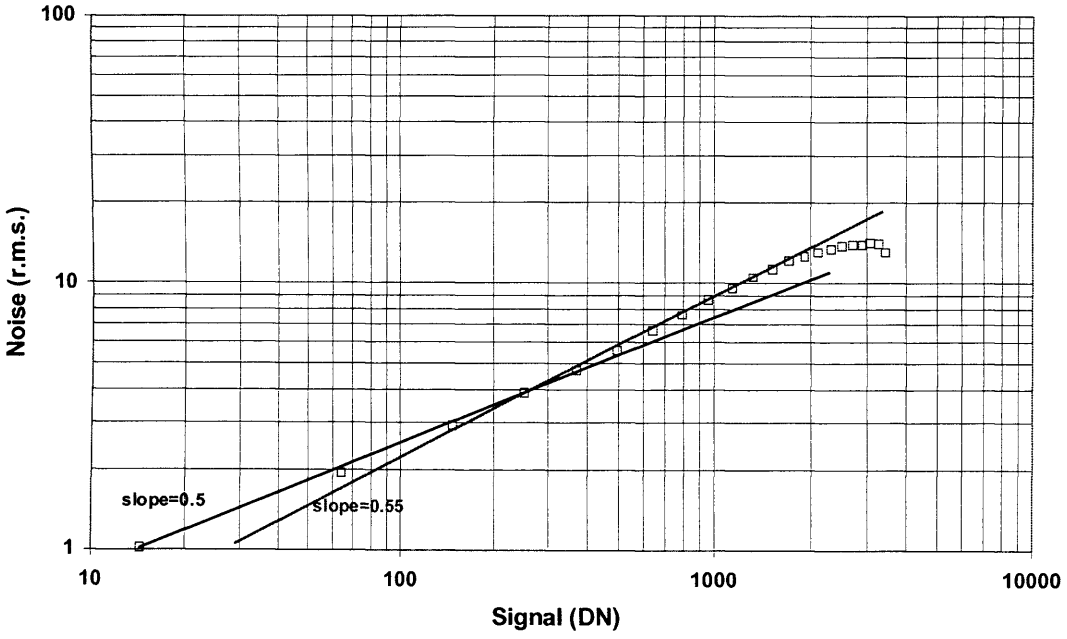

Figure 4.10. The photon transfer curve of the Vanilla sensor under "flush" reset operation.

The slope above 0.5 indicates that the read noise of the sensor has been reduced. This implies that the capacitance of the sense node has been reduced. Recalling Eq. 3.31 reduction in capacitance results in increase of the sense node sensitivity, which increases the camera gain as it is inversely proportional to the sense node sensitivity. Thus for the same flux of incident quanta, a higher number of ADC units are recorded from the sensor that is responsible for the super-linearity observed. Considering that the "flush" reset mode of operation aims to reduce reset noise via capacitive control, possibly the sensor suffers from capacitive coupling. This coupling could be originated from the extra reset circuit, and as result can alter the capacitance that source follower input transistor "sees" resulting in different sensor node sensitivity at different signal levels. This super-linearity makes the sensor inappropriate for medical imaging, where linear response is essential in order to compare the relative brightness of different structures in the image. Thus the 'flush' reset was not used. All the sensors were characterized under hard reset operation as it provides minimum image lag (Tian H *et al* 2001), a very important requirement for dynamic studies, which is the focus of this work.

4.3.1.7. Dark current transfer curve

The dark current can be measured by plotting the integrated charge due to thermal generation of electrons at different integration times (Fig. 4.11). From the slope of the linear regression of the data and Eq. 3.37 the dark current of the Vanilla sensor has been measured at room temperature. As can be seen from Figure 4.11 the nonlinearities of the Vanilla sensor observed in Fig 4.3 start to appear at the same integrated charge level. The data, above the point that nonlinearity appears, have been excluded from the fit. The dark current was found to be 43 pA/cm^2 (at ~300 K). This dark current approaches performance of CCD cameras and is very close to performance limits currently available in CMOS APS (Janesick J *et al* 2003, and Janesick J 2002). This plot could not be extracted from the 3T APS as this sensor was operated only at 10 fps.

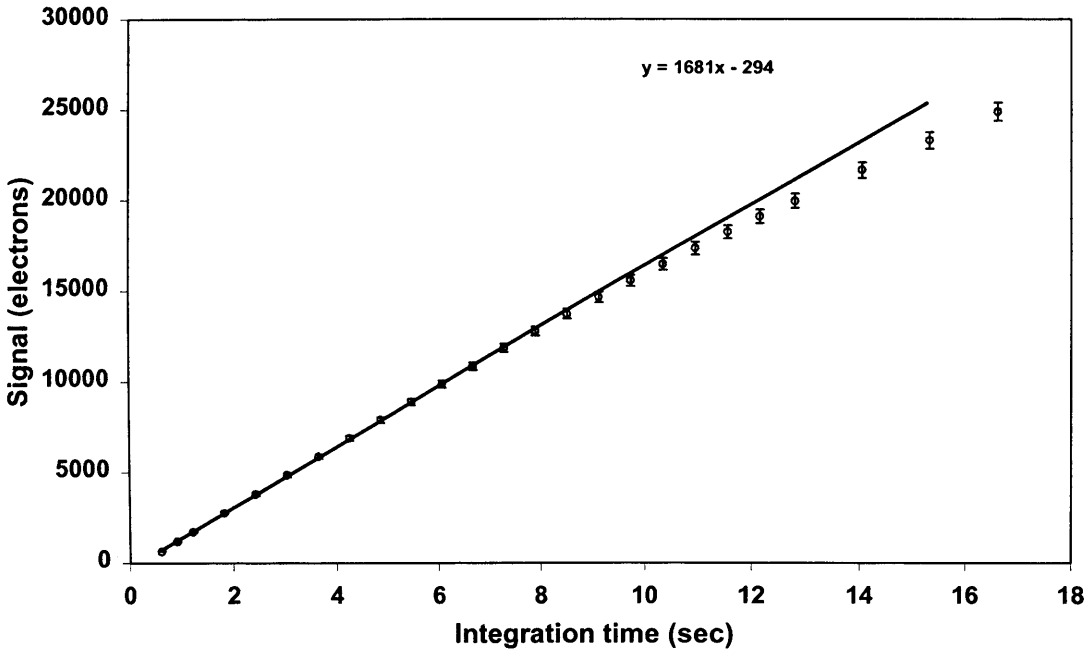

Figure 4.11. Integrated pixel charge of the Vanilla sensor at different integration times. The correlation coefficient of the fit was 0.99 with the data up to $1.5x10^4$ electrons signal

4.3.1.8. Interacting Quantum efficiency

The interacting quantum efficiencies of the 3T APS and the Vanilla sensor are presented in Figure 4.12. Both sensors have similar trends in their response, with Vanilla exhibiting remarkably higher spectral response. This is because in the manufacturing of Vanilla an optimised process has been adopted that resulted in thinner passivation layers (Fig 1.1) leading to an increase in sensitivity of the Vanilla. An additional reason is that the Vanilla sensor has 14 μm epi-layer, which almost 4 times thicker than the 3T APS (Fig 1.1), allowing photoelectrons generated deeper in the epi-layer (longer wavelength photons) to diffuse and to be collected by the photodiode.

The sudden changes in the interacting quantum efficiency are possibly due to photon scattering and diffraction from the data lines of the sensor. Especially in the 3T APS that incorporates 4 photodiodes per pixel. Because of this more lines above the photosensitive area of the sensor are required to connect the photodiodes with the readout circuitry of the pixel. An additional reason is that both sensors have been manufactured in monocrystaline silicon, so incident visible photons have to pass through a stack of top layers with different refractive indexes (Si:3-5, SiO_2:1.45) and thicknesses. The nature of

the various materials used in this stack makes the transmission wavelength dependent. The interacting quantum efficiency of the 3T APS and Vanilla was found to be 33% and 63% respectively at 540 nm. It is evident that the spectral response of the CMOS APS provides good spectral matching with the CsI phosphors whose emission spectrum peaks at approximately 540 nm (Zhao W *et al* 2004). The fact that the interacting quantum efficiency for both sensors peaks at approximately 630 nm indicates that CMOS APS provide excellent coupling efficiency for scintillators doped with Eu^{2+}.

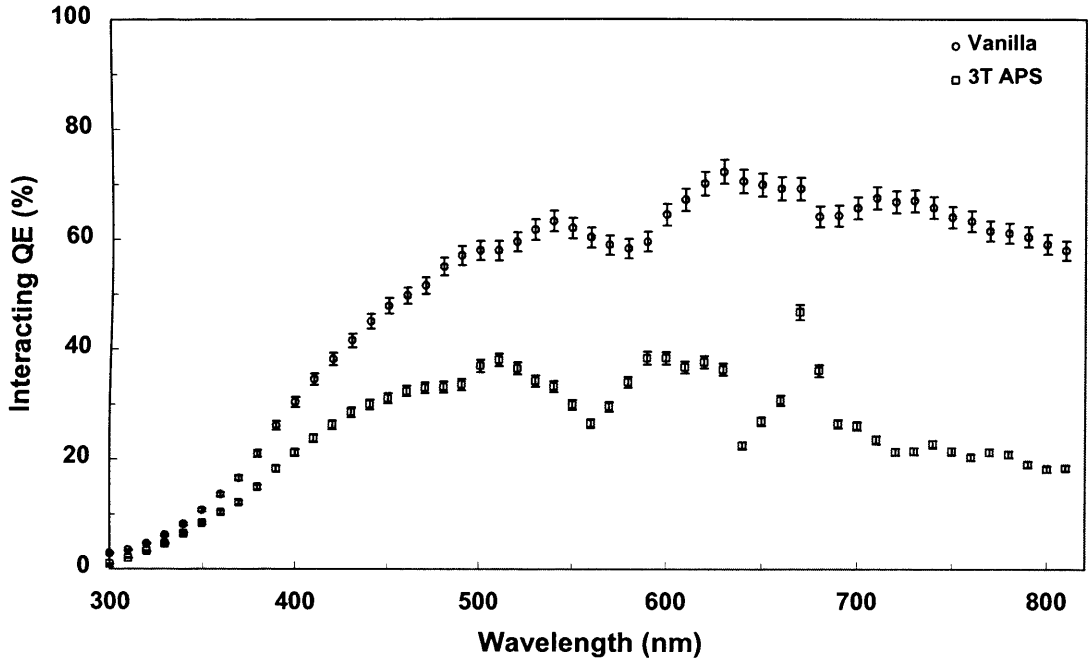

Figure 4.12. The interacting quantum efficiency of the 3T APS and Vanilla sensor as a function of wavelength.

4.3.1.9. Electro-optical performance comparison of the sensors

Table 4.1 presents a comparison of the electro-optical performance of the three sensors employed under "hard" reset operation. The 3T APS exhibits the highest noise floor. This is an inherent characteristic of the 3T APS as the sense node is part of the read out circuitry and it does not provide any way to compensate for the high kTC noise. Furthermore, the incorporation of the 4 PD per pixel, as was shown above, increases the capacitance of the sensor. Thus the kTC noise of the 3T APS could be much higher than the Vanilla. The OPIC sensor has a similar noise floor to the Vanilla. For the OPIC

sensor quantization noise was very high because the full dynamic range of the sensor is quantized with the per-pixel 8-bit ADCs. Instead, the results shown in Table 4.1 were calculated by sampling the dynamic range of the sensor using smaller ADC voltage range. The use of a smaller voltage range at which the ADC ramps reduces the camera gain, which in turn reduces the quantizing noise (Eq. 3.35). The pixel level DRAM was used to store a 7-bit gray code relating to the ADC signal level and a 1-bit parity code. These values are then related back to the global 12-bit DAC ramp as this is directly proportional to the measured pixel voltage. The linearity of the DAC-Voltage relation was investigated to ensure this calculation was valid for all pixel signals.

All sensors demonstrate similar dynamic range (DR) and shot limited signal to noise ratio (SNR). The slightly higher DR of the OPIC is because a global 12-bit DAC ramp was used to scan the sensor's dynamic range, whereas in the 3T APS and Vanilla sensor the range of the ADC ramp was adjusted to the point just before degradation in linearity of the sensors becomes very pronounced. The dark current of the Vanilla sensor is substantially lower than 3T APS this could be due to improved process employed in the Vanilla manufacturing. As explained above this was the reason for the high interacting QE of the Vanilla sensor. The OPIC had extremely low interacting QE mainly due to the small fill factor. In this sensor a high degree of pixel integration (127 transistors) was used in order to increase the pixel functionality. Although the OPIC is a very interesting and novel sensor with on pixel functionality and high frame rate capabilities, due to its very low sensitivity it has been excluded from the rest of the analysis. It is interesting to note that if this sensor is used for scientific or medical imaging the quantisation problems associated with the on-pixel ADC should be carefully addressed.

It is interesting to attempt a comparison of the performance of the sensors related with the pixel architecture and the process used to manufacture them. The 3T APS has been manufactured under standard 0.5 μm CMOS process (Table 2.1) and the Vanilla under optimised 0.35 μm processes (Table 2.1). It is evident that the optimised process offers a substantially improved performance in the dark current, possibly reflecting the maturity of CMOS sensors and the dramatic reduction of imperfections in the process. Another possible reason for the reduced dark noise of the Vanilla sensor is that it employs only one photodiode per pixel, perhaps resulting in less process-related imperfections in the

depletion and epi-layer, which have a direct impact on the leakage current. The two-fold interacting quantum efficiency justifies the improved response of the sensor when an optimised process is employed.

Figure 4.13 shows quantum efficiency of the two sensors when normalized to maximum. The trends and the peak value in the QE are similar showing some of the properties of the CMOS sensors. It is interesting to note that the response in the blue part of the spectrum is almost identical indicating that the relative response of the sensor does not alter by changing process, although smoother and higher sensitivity can be achieved. The big difference in the red part of the spectrum of the two sensors is due to the difference in the epi-layer (4 μm and 14 μm for the 3T APS and Vanilla respectively). It is apparent that the flexibility provided by CMOS sensors, makes it possible to produce sensors optimised for different imaging tasks.

Table 4.1. The electro-optical performance parameters of the three different CMOS APS employed

Performance Parameters	3T APS	Vanilla	OPIC	Units
Camera Gain	**114**	**13.6**	**29**	**electrons/DN**
Read Noise	**114**	**50**	**55**	**electrons**
Full Well	**1×10^5**	**55×10^4**	**1×10^5**	**electrons**
Pixel-to-Pixel Non-uniformity	**1**	**1**	**9**	**%**
Dark Current Non-uniformity	**-**	**23**	**-**	**%**
Integral Non-linearity (FW)	**7**	**9**	**-**	**%**
Shot Noise Limited SNR	**50**	**49**	**51**	**dB**
Dynamic Range	**59**	**60**	**65**	**dB**
Dark Current (@ ~300 K)	**600**	**45**	**-**	**(pA/cm^2)**
Interacting QE (@ 540 nm)	**33**	**63**	**4**	**%**

* The dark current of the 3T APS sensor was taken from Prydderch M. L. *et al* 2003.

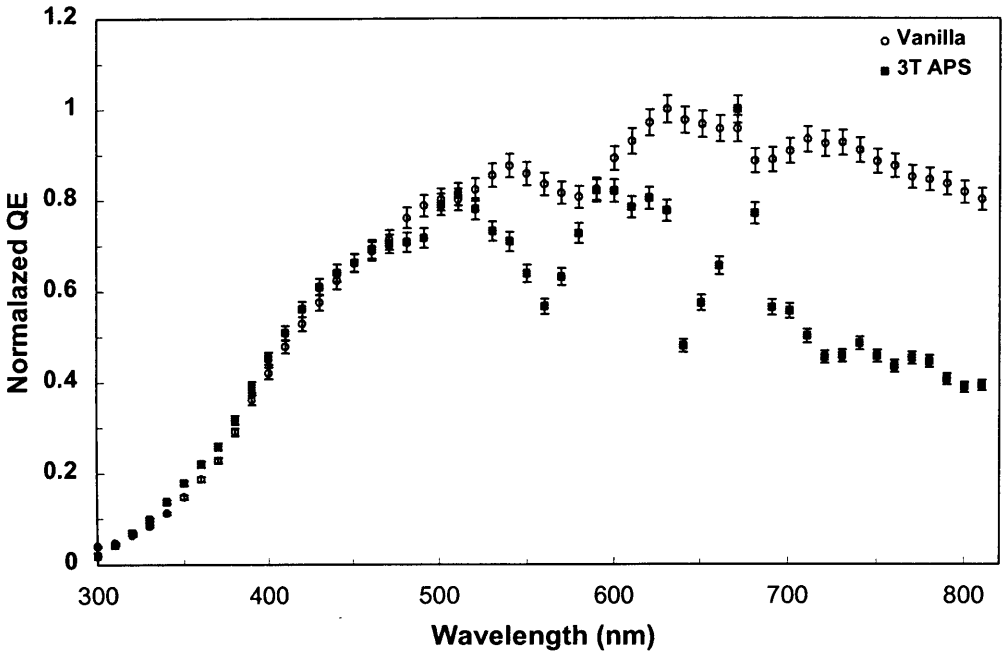

Figure 4.13. The normalized quantum efficiency of the 3T APS and Vanilla sensor as a function of wavelength.

4.3.2. Empirical physical characteristics of the X-ray imager

4.3.2.1. X-ray sensitivity of the imagers

The X-ray sensitivity of the two detectors with the different system configurations is given in Figures 4.14 and 4.15. Only the linear range of the sensor has been used under the X-ray irradiation. From the slope of the fits the X-ray sensitivity (or X-ray gain) of the different system configurations expressed in 'number of electrons per X-ray photon incident the detector' can be measured. The correlation coefficients of the linear regression fits is greater than 0.999. When employing the 115 μm CsI, X-ray gain is 47 electrons per X-ray photon and for the 95 μm CsI, 43 electrons per X-ray photon for the 3T APS sensor (Fig. 4.14). The small difference in these two phosphors reflects the difference in their thickness and the small difference in their quantum efficiency. For the Vanilla sensor when employing the 115 μm CsI, the slope is 137 electrons per X-ray photon and for the 150 μm HR and HS CsI, the slope is 109 and 198 electrons per X-ray photon respectively (Fig. 4.15). The difference in the slope of the 150 μm phosphors is 0.55 and is in close agreement with the design specifications provided from the vendor (FOS Hamamatsu).

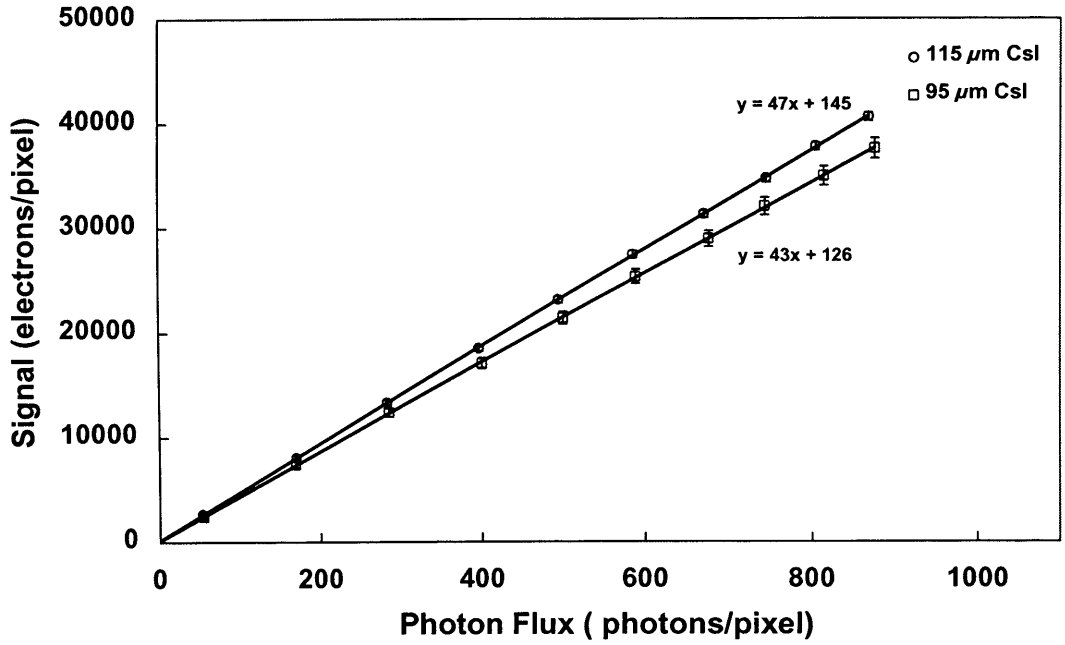

Figure 4.14. X-ray sensitivity of the two 3T APS system configurations expressed in absolute units. The correlation coefficient with the linear regression was 0.9999. The slope of the curve was used to measure the X-ray sensitivity of the sensor.

As was expected, the Vanilla system configurations are more sensitive than the 3T APS. This is due to two reasons. Firstly the Vanilla sensor, as was shown above, is almost twice as sensitive at the wavelength that the CsI phosphors emit (~540 nm). Secondly, in the 3T APS configurations two FOP with ~70% transmission each were used to couple the phosphors with the sensors that resulted in another 30% loss of optical quanta. This made the Vanilla system configurations 2.85 $(2/0.7)$ times more sensitive. This can be seen from the difference in the slope of the 115 μm phosphors that were used on both sensors. It is apparent that while 3T APS has longer range of linearity the Vanilla sensor has remarkable higher sensitivity that is able to detect single X-ray photon with approximately 20 keV energy. However, the maximum raw exposure that could be accommodated by the Vanilla system configurations was 2.0 μC/kg (150 μm CsI-HS), 2.8 μC/kg (115 μm CsI)and 3.5 μC/kg (150 μm CsI-HR). The raw exposure accommodated by the 3T APS system configurations was ~25.8 μC/kg. Thus, only the 3T APS system configurations as suitable for conventional mammography as they can accommodate the exposures found beneath the breast in conventional mammography. It

is apparent that the higher the system gain is the smaller is the exposure that the imagers can accommodate. Thus using CMOS APS sensors, X-ray imagers with wide range of sensitivities can be produced in order to satisfy the requirements of a given imaging task

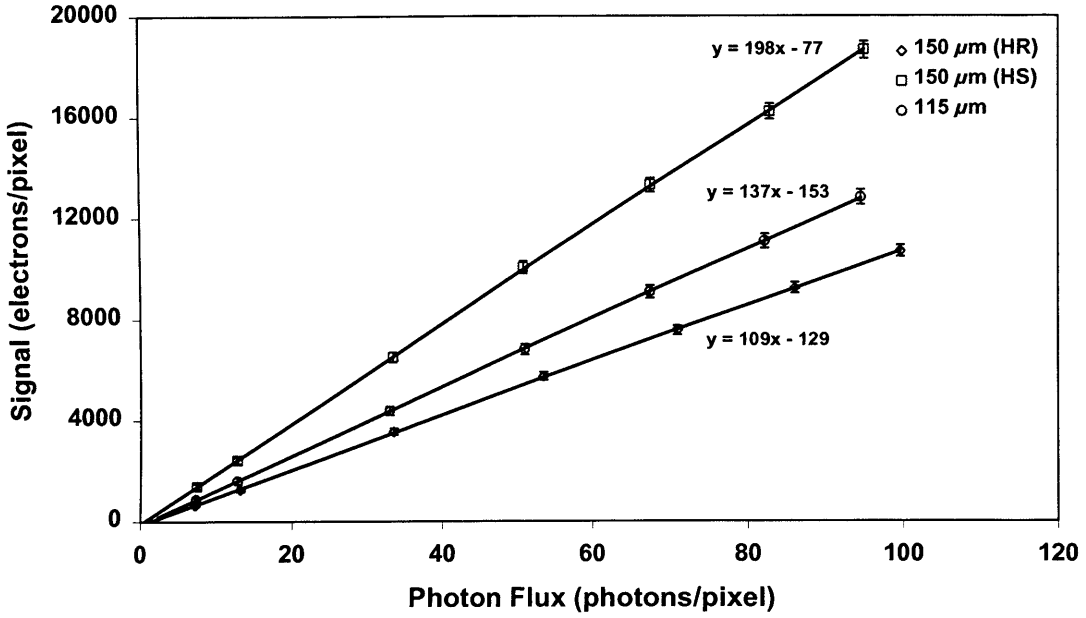

Figure 4.15. X-ray sensitivity of the three Vanilla system configurations expressed in absolute units. The correlation coefficient with the linear regression was 0.9999. The slope of the curve was used to measure the X-ray sensitivity of the sensor.

4.3.2.2. Oversampled line spread function

The oversamlped line spread function can be used to observe any serious degradation in the signal. Such degradation can be estimated from the full width at half maximum (FWHM) and the tails noise spreading. An additional reason was that we wanted to see if there any differences in the LSF of the CsI provided from the two different vendors. In Figure 4.16 the normalised oversampled LSF of two Vanilla system configurations is shown. As can be seen the LSF in the system configuration with 115 μm CsI the LSF exhibits a constant exponential decay. Conversely, in the system with 150 μm CsI (HR), the LSF reaches a point where it bends and follows a Lorentzian decay. Similar results were obtained from the 150 μm (HS) CsI. This response of the CsI is due to the absence of substrate patterning, a technique that forces the formation of columnar structure directly from the substrate (Jing T *et al* 1992). Absence of pattering in the 150 μm CsI

(Zhao W et al 2004) results in the formation a very thin crystal layer of a few microns as the CsI is deposited on the fibre optic plate that acts as a light diffuser. However, the 150 μm CsI, despite being a thicker phosphor has a slightly narrower FWHM. This is probably due to poor phosphor coupling in the 115 μm CsI.

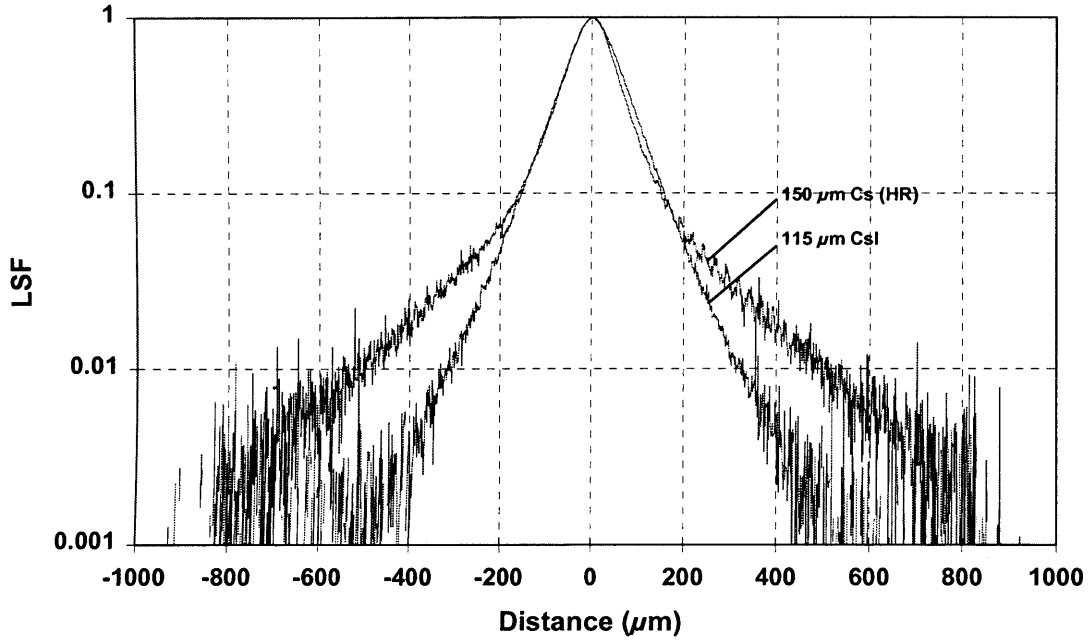

Figure 4.16. The normalized oversampled LSF of the Vanilla system configurations with the 150 μm (HR) and 115 μm phosphors.

Figure 4.17 shows the comparison of the LSF of the 3T APS and Vanilla sensor when coupled with the 115 μm CsI. The two sensors had the same pixel size thus any degradation in the LSF is primarily due to different coupling with the CsI. In the 3T APS, due to the presence of the glued FOP, we were able to achieve good coupling through high compression. As can be seen the effect of coupling on the LSF is significant thus very good coupling has to be achieved for high resolution detectors. It is apparent that this is more important than the optical properties of the phosphor and can have a significant effect on the overall response of the sensor (Maidment A D *et al* 1993). We have to note that in the Vanilla system configurations was not possible to improve the coupling efficiency more as the sensor was very sensitive to compression.

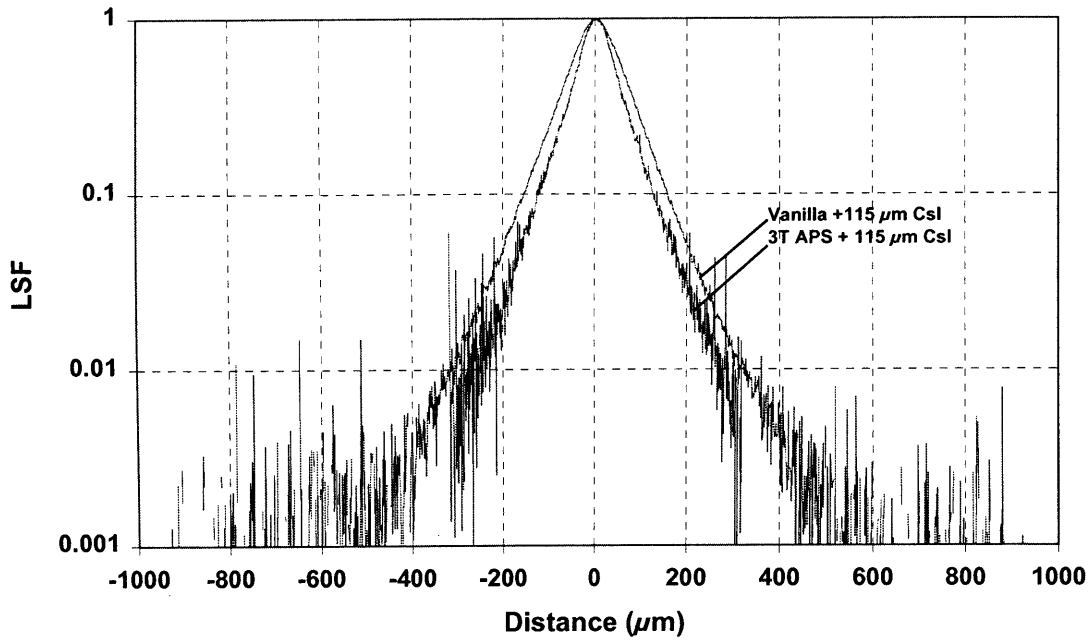

Figure 4.17. The normalized to unity oversampled LSF of the 3T APS and Vanilla sensors coupled with 115 μm CsI.

4.3.2.3. Modulation transfer function of the imagers

The MTF plot of the Vanilla and 3T CMOS system configurations is shown in Figure 4.18. The MTF of the 3T APS system configurations at 10% was 9 cycles/mm and 9.5 cycles/mm for 115 μm and 95 μm CsI respectively. The MTF for the Vanilla system configurations was 10% at 7 cycles/mm cycles/mm for the 150 μm (HR) CsI, and 6.5 for the 150 (HS) μm and 115 μm CsI respectively. Both phosphors used with the 3T APS have been optimized for high resolution and are suitable for conventional mammography. The MTF of both 3T APS system configurations at low frequencies is almost identical. The MTF above 10 cycles/mm is similar for both system configurations. This could be due to the 70% backing reflectivity employed in both phosphors and the imperfect coupling of the CsI with the sensor. For the Vanilla system configurations the 115 μm CsI had better resolution at low frequencies, whereas the configuration with the 150 μm HR CsI was better at high frequencies, as this CsI has been optimized for high resolution. The system configuration employing the 150 μm HS CsI had the lowest resolution as it has been optimized for high sensitivity (Fig. 4.15).

The lower resolution of the Vanilla system configurations was because optimum coupling efficiency could not be achieved, as discussed above. It is interesting to note the higher MTF at low frequencies of the CsI phosphors with substrate patterning. Based on the above discussion, it is apparent that substrate patterning is very important at low frequencies and can result in substantial improvement at mid to low frequencies. However, at high frequencies the diameter and the quality of the columns are possibly more important. The quality of the column could reduce light diffusion or column cross talk and guide the light in a more efficient way. This will increase the resolution of the system at high frequencies. It should be emphasized that for indirect X-ray detectors the system MTF is affected by the "optical" MTF that describes the degradation of system's MTF due to the imperfect coupling of the scintillator with the sensor. This type of degradation is a concern in indirect detection imagers and if not minimised can have a significant contribution to the system's MTF especially at higher frequencies. This is apparent from the differences in the MTF at the high frequencies between the 3T APS and Vanilla sensors when coupled with the same CsI (Fig. 4.18)

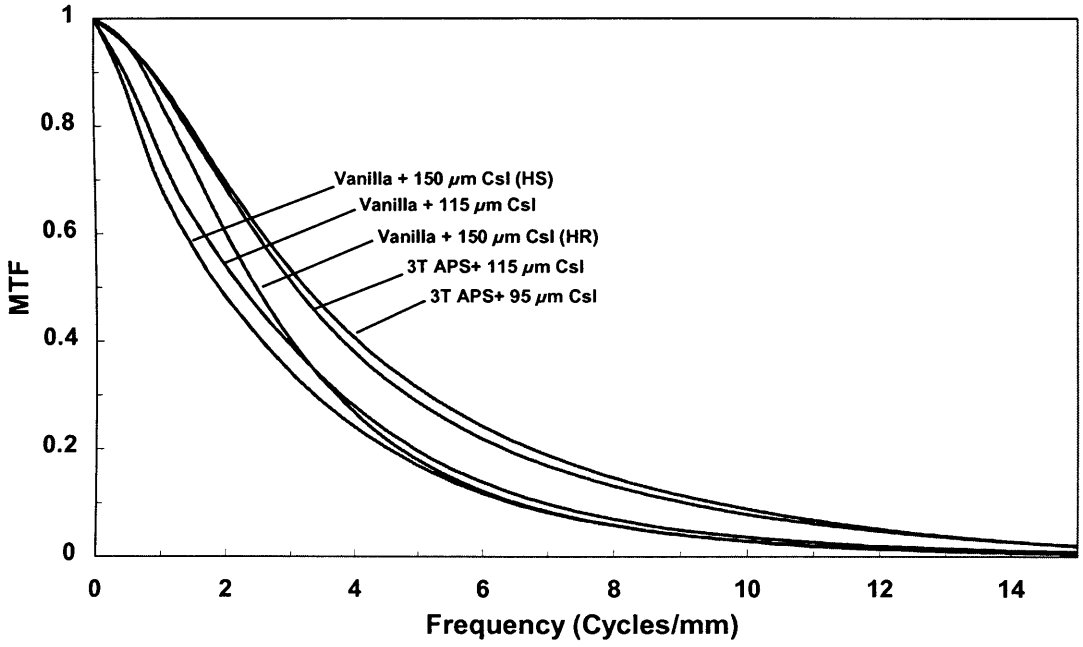

Figure 4.18. The MTF plot of the Vanilla and 3T CMOS system configurations.

4.3.2.4. Binned MTF

As the resolution of the system at this pixel size is primarily determined from the resolution of the scinillator, results from the 3T APS are also presented (Fig 4.19) with the pixels binned in a 2x2 configuration to achieve 50μm pitch. This will allow us to determine the effect of the pixel size on the system's MTF. The pixels were binned after readout and the MTF of the system configuration employing the 115 μm CsI was determined. The MTF of the sensor alone has also been determined at 25 and 50 μm pixel pitch. The MTF of the system was 10% at 8 cycles/mm. It can be seen that although the degradation in the sensor MTF is significant, the system's resolution was not changed significantly. This suggests that a pixel size of 50 μm could be used for high resolution performance.

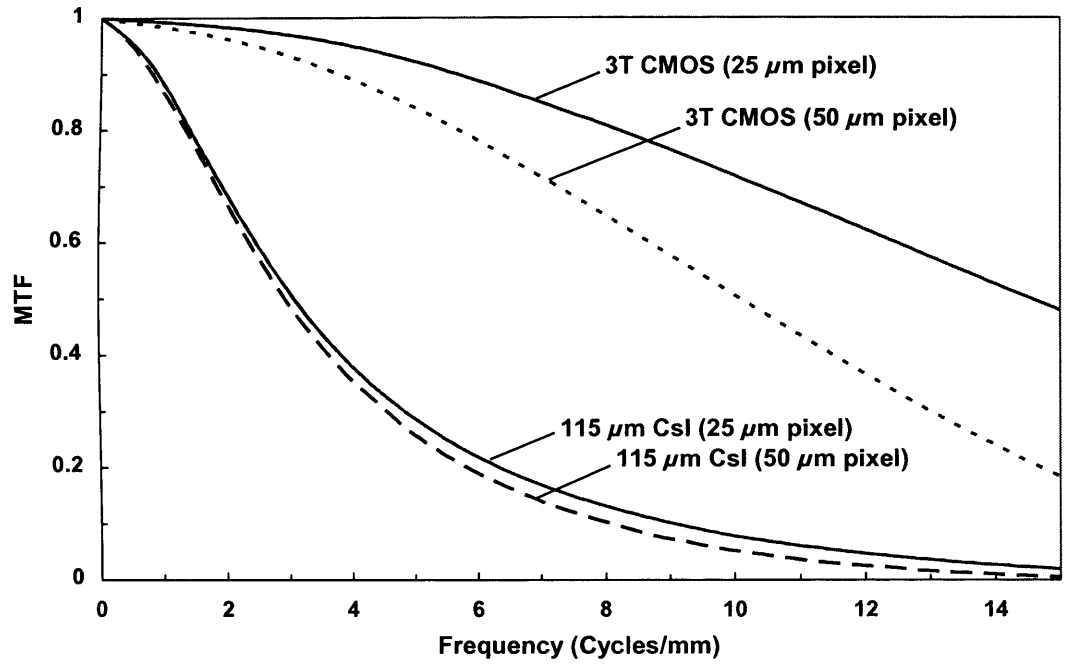

Figure 4.19. The MTF of the 3T CMOS and the MTF of the 115 μm system configuration at 25μm pixel pitch and after binning a 2x2 block of pixels.

4.3.2.5. MTF as a function of energy

Although the x-ray imager is evaluated in the mammographic energy range, it is interesting to measure if there is any degradation in its resolution due characteristic rays absorption when the energies used are above the k-absorption edge (33.2 keV) of the

iodine. This will be important in dual energy imaging. Figure 4.20 shows the MTF of the Vanilla sensor with150 μm HS CsI for two energies that straddle the iodine k-edge. Division of the system MTF measured at energy above the iodine k-edge (34 keV) with the MTF below k-edge provides the MTF of the k-absorption edge only. For completeness the MTF determined using Mo tube operated at 30 kVs is also shown in Figure 4.20. These experiments were performed in ID17 biomedical beamline at the European Synchrotron Radiation Facility (ESRF). The facility consists of a monochromator hutch and an experimental hutch located in the satellite building, outside the storage ring. The white beam reaching the detector is fan with maximum dimension of 150 mm width and 20 mm height. A tunable fixed exit device based on two bent Si crystals has been used as the monochromator. It produces a monochromatic beam parallel to the incident white beam, with a vertical offset of 40 mm.

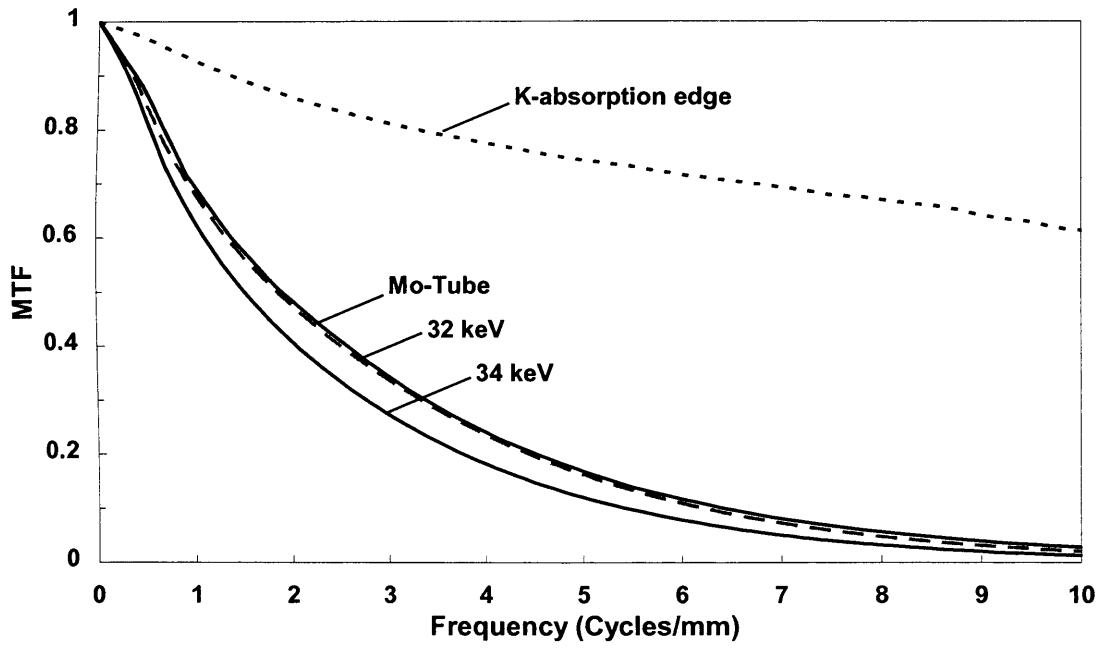

Figure 4.20. The MTF plot of the Vanilla coupled with 150 μm HS CsI for 32 and 34 keV energies. The K-absorption edge MTF and the MTF of the system using Mo tube operated at 30 kVs is also shown.

The MTF at 32 and 34 keV at 10% was 6.1 and 5.4 cycles/mm respectively. It can be seen that when the energy is above 32.2 keV there is modest degradation in the MTF of the sensor above 1 cycles/mm. At mid frequencies the degradation is more pronounced

indicating that the characteristic rays absorption contributes in the reduction of the resolution of the sensor. The MTF of the k-absorption edge shown in Figure 4.20 could be slightly underestimated, as the absorption ratio of the CsI is much higher above the iodine k-edge, leading to smaller depth of interaction of the X-ray photons. Although the CsI studied is structured, imperfections in the columns could lead to higher light diffusion as it is propagated towards the sensor that further degrades the MTF at 34 keV. However, the contribution of the light diffusion is assumed to be very small. It is interesting to note that the reduction in the MTF due to absorption of characteristic rays is more significant as compared with the effect of pixel binning (Fig. 4.19).

4.3.2.6. Two dimensional noise power spectrums

The two dimensional NPS for the 3T APS system configurations and the sensor electronic noise are displayed in Figure 4.21. The exposure at the detector entrance window was 0.44 μC/kg (1.72 mR).

At zero frequency in the y-axis (column direction) the noise was higher than in the x-axis (Fig. 4.21 (a)). This higher DC noise in the y-axis is associated with nonstationary fluctuations arising from the row select transistors of the imager during read out. In particular, this DC component is due to high frequency electromagnetic interference noise that expresses itself in the image as horizontal stripes. Horizontal stripes in the image appear because the EMI signal is synchronized to the start of the readout. This can happen when at the start of line readout, more current is drawn from some DC/DC converter and it reacts with an unwanted voltage swing. This swing always has the same form and always comes at the start of column read out; the result is a non-regular horizontal strip. Stationary vertical variations between column amplifiers have been corrected by dark field subtraction, although remnants are present as seen from the weak, but noticeable, amplitude of the x-axis in the 2D NPS (Fig. 4.21).

A number of spikes can be observed in Figs 4.21(b) and 4.21(c). These are usually associated with correlated pick up noise from power supplies (Siewerdsen J *et al* 1998), or electromagnetic interference from the X-ray tube (Williams M B *et al* 1999). Since they are absent in the dark frame NPS, their source is unlikely to be pick up noise. It appears that this systematic noise is neither pick-up noise nor electromagnetic

interference. In addition, the fact that the spikes appear at different frequencies means that they are not due to electromagnetic interference from the X-ray tube, since such interference would have the same frequency in both system configurations.

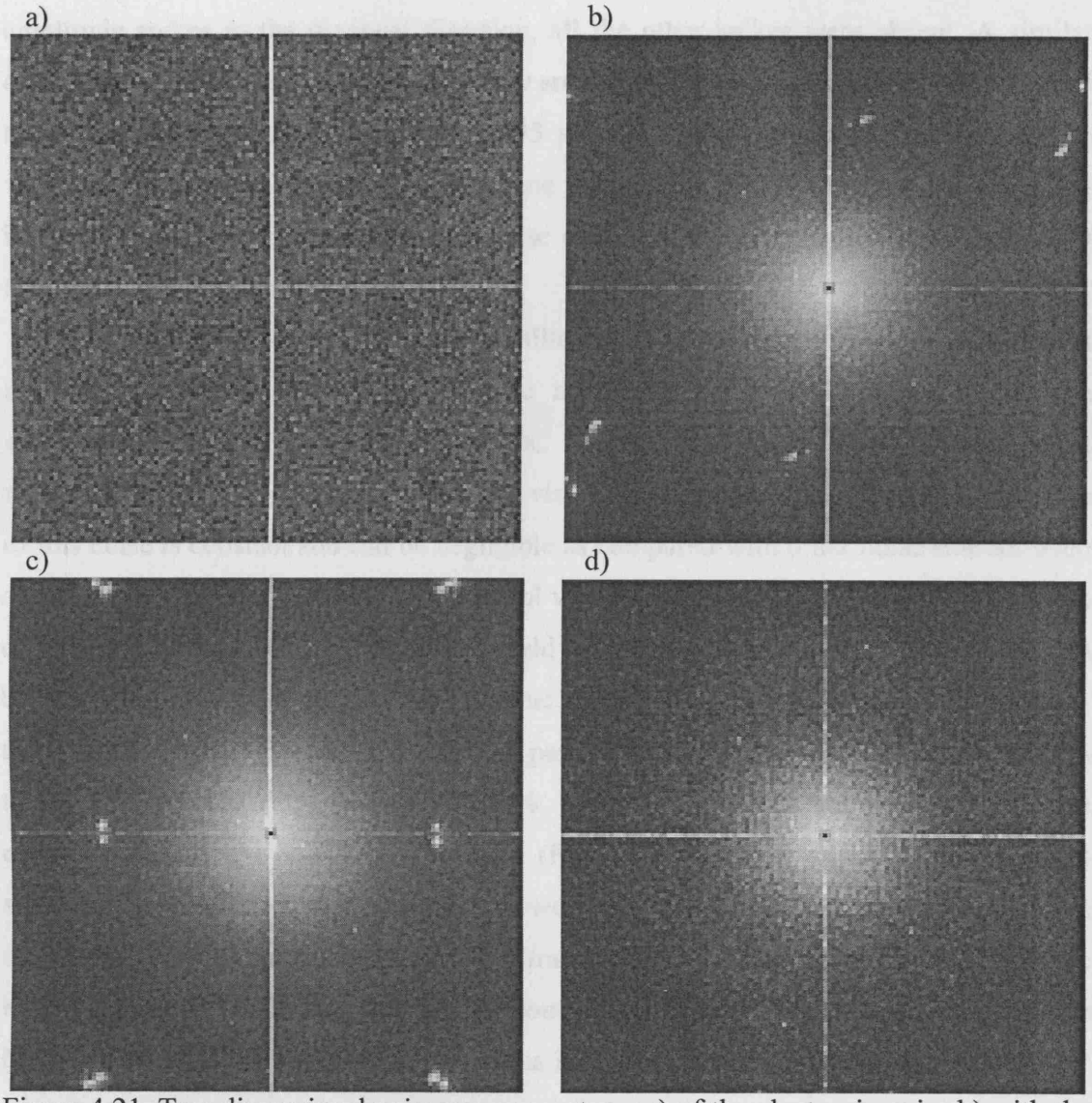

Figure 4.21. Two dimensional noise power spectrum a) of the electronic noise b) with the 115 μm CsI phosphor, c) with the 95 μm CsI phosphor at 0.44 μC/kg d) with powder phosphor. The noise at the intersection of frequency axes has been removed.

These peaks may arise from the two different FOP used, or may occur from mismatch of the two different FOP. This assumption may be confirmed by the fact that upon closer inspection, both spectrums have low amplitude peaks in the 2D NPS that are located in the diagonal direction. These are due to the FOP that was glued to the sensor, common to

both system configurations. Alignment of two different FOPs is a very tedious task; however, the 2D NPS analysis might provide a way to achieve this where necessary. In order to evaluate this assumption, a powder phosphor has been coupled to the sensor and the 2D NPS of flat field images has been measured (Fig. 4.21(d)). Apart from the small amplitude spikes in the diagonal direction, all the other spikes were absent. A similar argument has been used to explain the very small asymmetry observed in the 2D NPS of the system configuration employing the 95 μm CsI. This asymmetry was localized to very low spatial frequencies, in only one line parallel and directly adjacent to y-axis and is not representative of the system. Because of this it has been excluded from the 1-D NPS of this system configuration.

The two dimensional NPS of the Vanilla with the 150 μm (HS) CsI phosphor at different exposures and sensor electronic noise are displayed in Figure 4.22. The exposures are given in the plots. The DC noise in the y-axis from the row select transistors of the imager due to EMI is also visible in this sensor. However, the amplitude of this noise is constant and can be negligible as compared with other noise sources even at low exposures (Fig. 4.22 (b)). The vertical variations between column amplifiers in the dark images have been corrected by dark field subtraction, however at higher exposures it becomes more noticeable and exhibits higher amplitude as can be seen on the x-axis in the 2D NPS. This is characteristic of fixed pattern noise that increases proportional with the signal intensity (Fig. 4.6). In the dark image a weak but noticeable long range correlation along the x-axis can be seen (Fig 4.22 (a)). The origin of this spectral signature has not been fully understood. However, correlated components of the NPS are reduced by the square of the modulation transfer function (MTF) associated with the blurring process, while uncorrelated Poisson noise is transferred independently of the MTF (white additive electronic noise). Thus it is assumed that this is related with pixel cross talk. Cross talk is an unwanted component that reduces the MTF of the sensors. In the horizontal direction of the sensor due to the extra metal line of the "flush" reset circuit the pixels of the sensor are more isolated. Isolation of pixels results in low cross talk (Mulato M *et al* 2001). In the vertical direction there is only one metal line minimizing the photosensitive distance between pixels, possibly resulting in higher cross talk between pixels in this direction.

Figure 4.23 shows the NPS of the other two Vanilla system configurations at exposure 0. 47 μC/kg. We have to note that HR CsI was coupled to different Vanilla sensor.

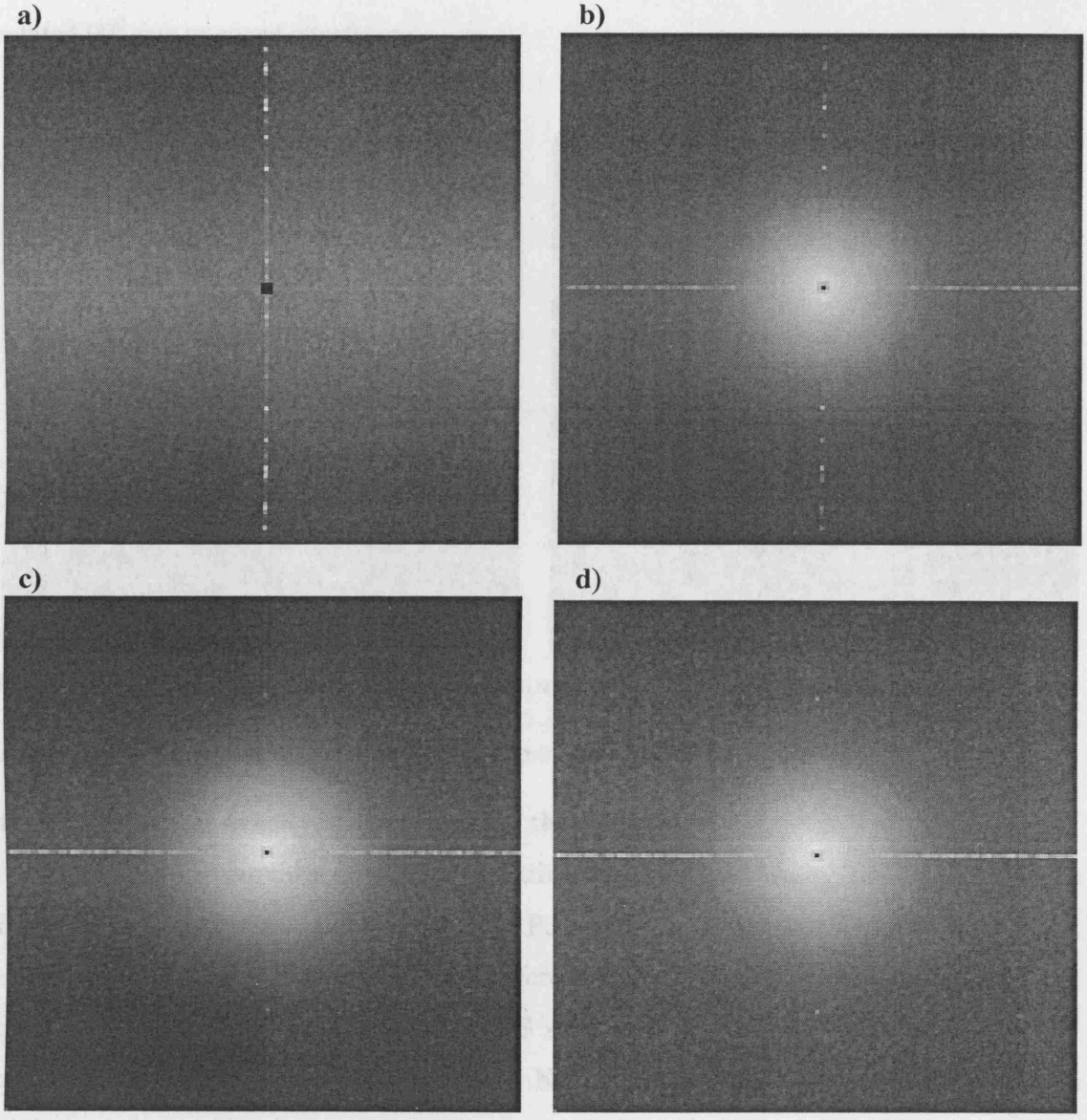

Figure 4.22. Two dimensional noise power spectrum of the Vanilla sensor a) of the electronic noise and b), c), and d) with the 150 μm (HS) CsI phosphor at exposures 0.05 μC/kg and 0. 47 μC/kg and 0.66 μC/kg. The noise at the intersection of frequency axes has been removed.

The 2D NPS with the 150 μm (HR) CsI phosphor is almost identical to the system configuration with the HS phosphor; however, the DC noise in the y-axis is much higher

indicating that this sensor might have ground problems. In the 115 μm CsI system configuration the number of spikes observed in Figure 4.21(b) are also present indicating that these are entirely due to the FOP structure. They appear in opposite quarters, as compared with the 3T APS, because for the coupling with Vanilla sensor the CsI was rotated 90^0 due to space constraints.

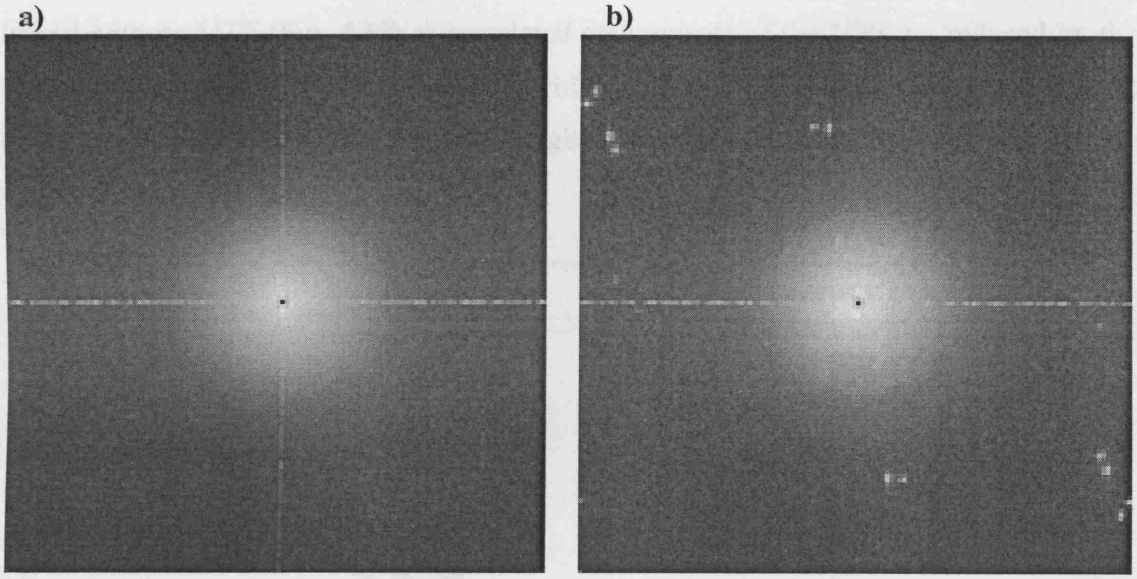

Figure 4.23. Two dimensional noise power spectrum of the Vanilla sensor a) with the 150 μm (HR) CsI phosphor and b), with the 115 μm CsI phosphor at exposure 0. 47 μC/kg. The noise at the intersection of frequency axes has been removed.

4.3.2.7. Spectral density measurement of the imagers

The 1D NPS provides a way to quantify the spectral density differences of the different system configurations of the 3T APS and Vanilla sensors. The raw 1D NPS at an exposure of 46 μC/kg of the five different system configurations along with the electronic noise of the Vanilla and 3T APS sensors is shown in Figures 4.24 and 4.25 respectively. Note that the y-axis in the raw NPS is expressed in absolute units since the digital pixel signal has been converted to electrons through the camera gain constant. The amplitude of the spectral density at low to mid frequencies is proportional with the gain of the systems. The Vanilla sensor with the 150 μm (HS) CsI phosphor has the higher noise, as this is the more sensitive sensor. In this system configuration the contribution of electronic noise was minimal as can be seen from the plateau. Similar response is observed for the 150 μm (HR) CsI configuration, although it has smaller amplitude due to

its low sensitivity. The high sensitivity phosphor results in higher spectral density due to higher quantum noise. The 115 μm CsI configuration of Vanilla sensor has intermediate response at mid to high frequencies although at low frequencies its spectral density is comparable with the HS configuration. This high noise component might be due to a higher fixed pattern noise of the fibre optic plate that is added to quantum noise. The much higher slope in the decay of the NPS of this Vanilla system configuration is directly linked with its MTF (Fig. 4.18) as correlated components of the NPS are reduced by the square of the modulation transfer function (MTF). In all Vanilla system configurations at this exposure, the electronic noise had marginal contribution to the total spectral density up to Nyquist frequency.

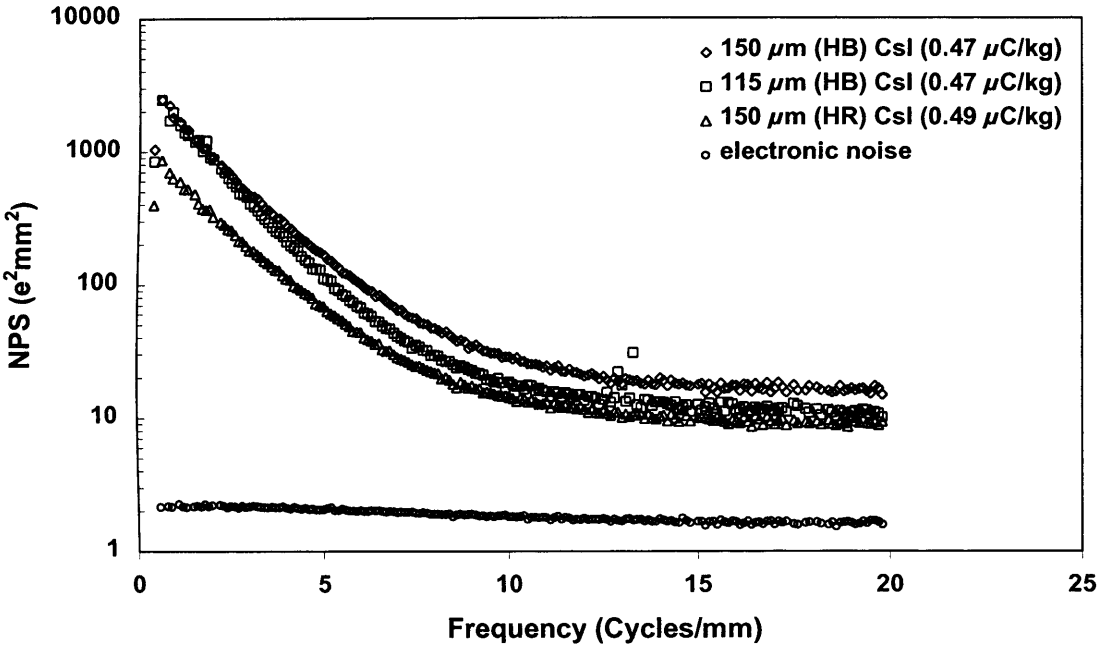

Figure 4.24. Semilog plot of the raw one dimensional NPS (absolute spectral density) of the three different Vanilla system configurations along with the electronic noise. The detector entrance exposure is shown in the plot.

In the 3T APS system configurations, the electronic noise at low frequencies has very little effect on the total noise power spectrum of the two different system configurations. At low frequencies, the noise of the system configuration employing the 115 μm CsI is higher than the one with the 95 μm CsI, as expected for a higher gain X-ray converter. The spikes discussed above are evident in the 1D NPS due to their high amplitude. At

higher spatial frequencies the two spectrums are almost identical and limited from the high contribution of electronic noise. It is interesting to note that the spikes observed in the system configurations with 115 μm CsI and 95 μm CsI appear in the 1D NPS at 15 cycles/mm irrespective of sensor used or FOP orientation. The empirically determined electronic noise was found to be ~8.4 e^2 mm^2 and ~1.8 e^2 mm^2 for the 3T APS and Vanilla sensors. This is in agreement with noise measured using the PTC method. The small slope in the Vanilla electronic noise from to low to high frequencies is due to the long range correlation observed 2D NPS (Fig. 4.22 (a)).

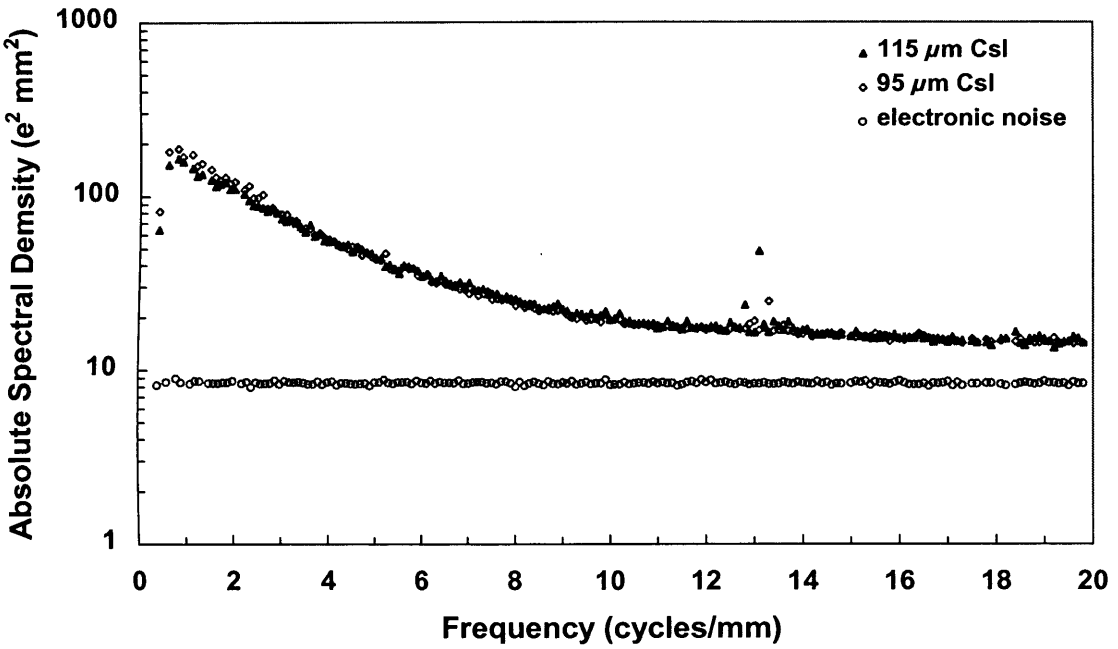

Figure 4.25. Semilog plot of the raw one dimensional NPS (absolute spectral density) of the two different 3T APS system configurations along with the electronic noise. The detector entrance exposure was 44 μC/kg.

Figure 4.26 shows the raw one dimensional NPS (absolute spectral density) of the Vanilla sensor with the 150 μm (HR) CsI at different detector entrance exposures. The exposure range under which the detector was evaluated is shown in the figure along with the electronic noise of the Vanilla. At low frequencies the electronic noise has very little effect on the total noise power spectrum over all exposures. It is worth noting that the exposure of 0.05 μC/kg integrated over the spectrum, results in only 5 X-ray photons per pixel. The small contribution of electronic noise to the total noise of the system especially

at low frequencies, indicates the ability of the Vanilla sensor to detect a single X-ray photon. However, at higher spatial frequencies the contribution of electronic noise is relatively high. Above 0.23 μC/kg the contribution of electronic noise is less than 10 % at frequencies below 8 cycles/mm. At this exposure level the noise scales proportionally (see next section) with the exposure.

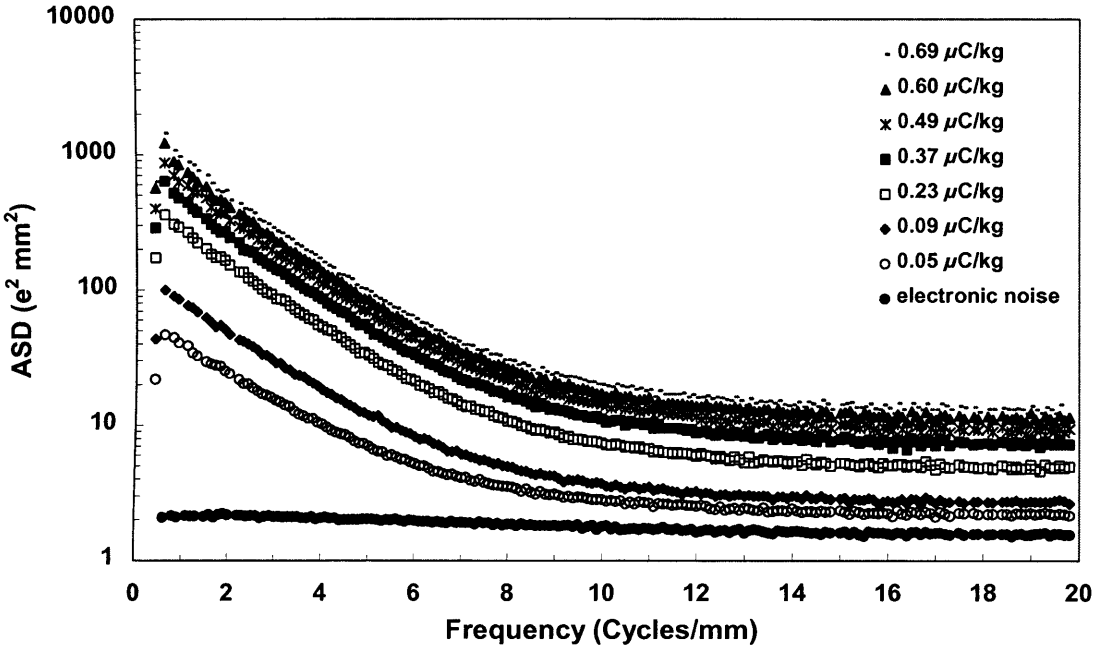

Figure 4.26. Semilog plot of the raw one dimensional NPS (absolute spectral density) of the Vanilla with the 150 μm (HR) CsI at different detector entrance exposures. The electronic noise is also shown.

4.3.2.8. A simple method to determine quantum limited detectors

A system where the dominant source noise is the x-ray quantum noise is called quantum limited and the DQE is independent of the exposure (Eq. 3.17). That is, the DQE does not change by increasing the exposure and the system noise changes with the square root of the signal (Rose A. *et al* 1953). A simple way to find the exposure level at which a system is quantum limited is by plotting the noise versus signal in a log-log plot and find at which exposure the slope is equal to 0.5. Figure 4.27 shows the pixel noise versus the pixel signal in a log-log plot of the Vanilla detector with the 150 μm CsI (HR). The noise has been extracted from the integral of the 2D NPS and the signal is the square root of large area signal (Eq. 3.17) used to determine the DQE. The detector entrance

exposures at which the data have been extracted were 0.0 μC/kg, 0.05 μC/kg, 0.09 μC/kg, 0.23 μC/kg, 0.37 μC/kg, 0.49 μC/kg, 0.60 μC/kg, 0.69 μC/kg. The linear regression of the experimental data points and the calculated gradient is shown in the plot. A slope less than 0.5 indicate the presence of significant contributions to the noise power from sources other than x-ray noise (electronic noise). A slope higher than 0.5 signifies the presence of fixed pattern noise and should be removed through simple flat fielding. Based on the Figure 4.27 the Vanilla sensor with the 150 μm (HR) CsI the DQE should be independent of exposure above 0.23 μC/kg. This method is validated in the next section where the DQE of all the system configurations is presented.

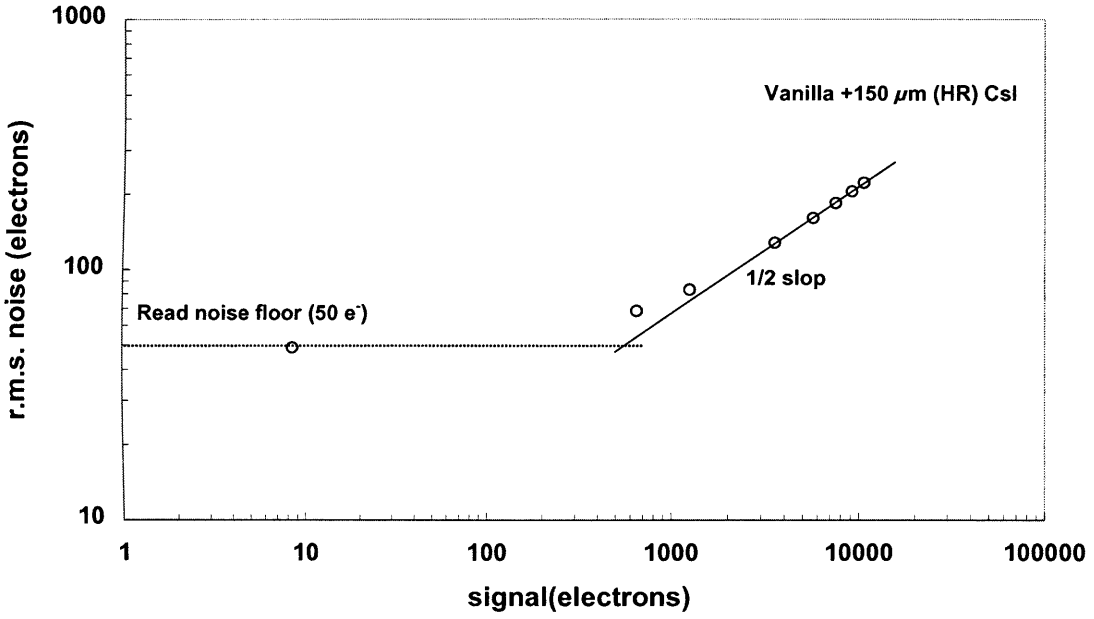

Figure 4.27. A log-log plot of the r.m.s. noise versus signal. The data have been extracted from the Vanilla with the 150 μm (HR) CsI.

4.3.2.9. DQE measurement of the imagers

The DQE of the system configurations of the two sensors was determined according to Eq. 3.17 and results are displayed in Fig. 4.28-4.31. The DQE of the 3T APS configurations (Fig 4.28) close to zero frequency of the two different system configurations was ~0.48 and ~0.45 for the 115 μm and 95 μm CsI respectively at detector entrance exposure of 0.44 μC/kg. The measured photon flux at this exposure was

102000 X-rays photons/mm^2. The system configuration with 115 μm CsI has marginally better DQE over all frequencies. Overall, the two system configurations have marginal difference in their performance. However, it is evident that the 3T APS sensor is reasonably sensitive and can record the marginal differences between the two X-ray converters employed in this study. Current constraints in changing the integration of the 3T APS and low X-ray fluence of the tube resulted in only one exposure for the DQE determination in the two different system configurations.

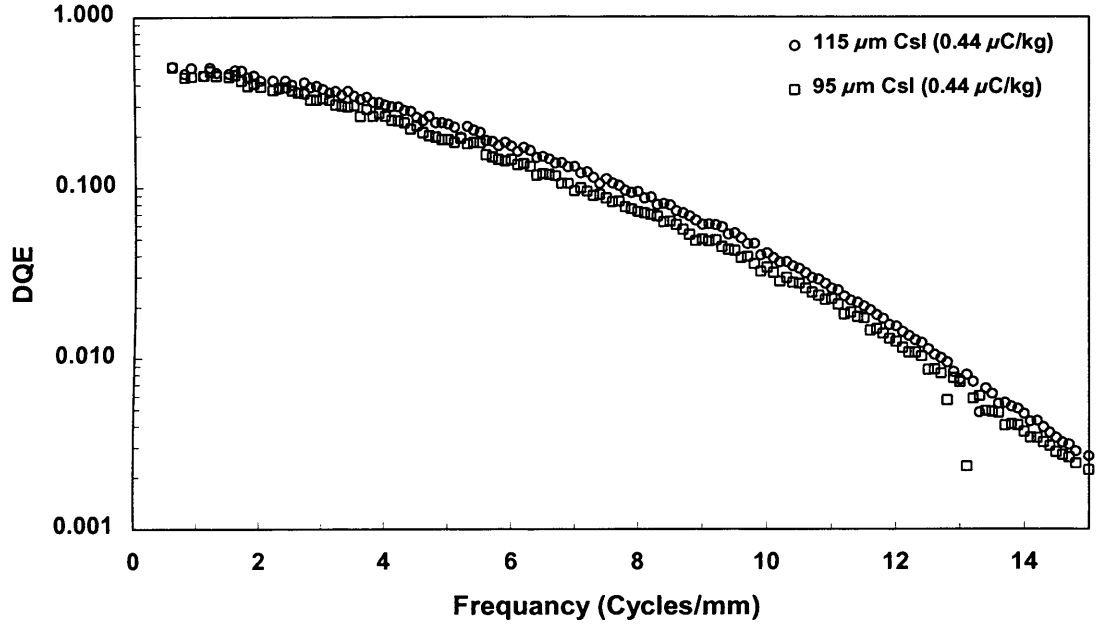

Figure 4.28. Semilog plot of the DQE of two 3T APS system configurations at detector entrance exposure of 0.44 μC/kg.

The DQE of the Vanilla with the 115 μm CsI (Fig. 4.29) close to zero frequency was ~0.35, ~0.32 and ~0.35 at detector entrance exposure of 0.05 μC/kg, 0.47 μC/kg and 0.66 μC/kg respectively. At these exposures, the measured photon flux was 11700 X-rays photons/mm^2, 108000 X-rays photons/mm^2, and 151000 X-rays photons/mm^2 respectively. Quantum limited response was achieved at 0.23 μC/kg. However, as mentioned above, this detector configuration has poor coupling efficiency that limits its DQE to much lower values compared with the 3T APS configuration that uses the same CsI. The reduction of DQE at low frequencies as function of the exposure is due to the presence of some remnant fixed pattern.

The DQE of the Vanilla sensor with the 150 μm CsI (HR) (Fig. 4.30) close to zero frequency was ~0.50, ~0.44 and ~0.42 at detector entrance exposure of 0.05 μC/kg, 0.49 μC/kg and 0.69 μC/kg respectively. At those exposures measured photon flux was 11600 X-rays photons/mm^2, 113500 X-rays photons/mm^2, and 159000 X-rays photons/mm^2 respectively. Quantum limited response was achieved at 0.23 μC/kg. This validates the method developed and is summarised in Figure 4.27. The DQE at low frequencies decreases as a function of the exposure due to the presence of fixed pattern noise.

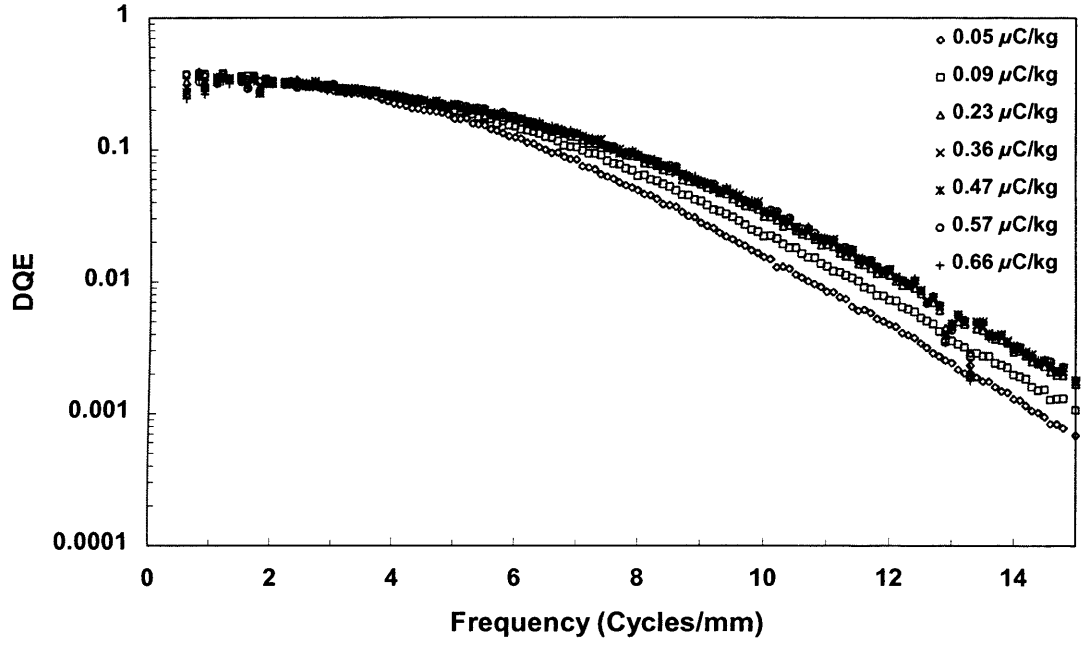

Figure 4.29. Semilog plot of the DQE of the Vanilla system configuration with 115 μm CsI and DQE with read noise removed DQE. The detector entrance exposure is shown in the plot.

The DQE of the Vanilla with the 150 μm CsI (HS) (Fig. 4.30) close to zero frequency was ~0.52, ~0.44 and ~0.43 at detector entrance exposure of 0.05 μC/kg, 0.47 μC/kg and 0.66 μC/kg respectively. At these exposures measured photon flux was 11860 X-rays photons/mm^2, 108000 X-rays photons/mm^2, and 152000 X-rays photons/mm^2 respectively. Quantum limited response was achieved at 0.23 μC/kg.

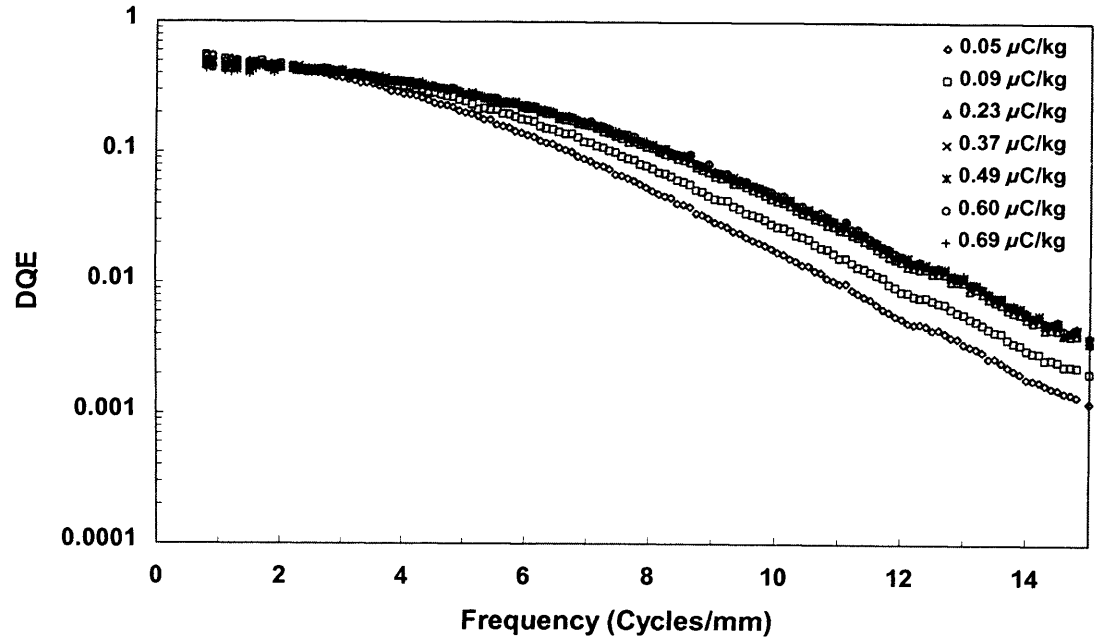

Figure 4.30. Semilog plot of the DQE of the Vanilla system configuration with 150 μm CsI (HR) and DQE with read noise removed DQE. The detector entrance exposure is shown in the plot.

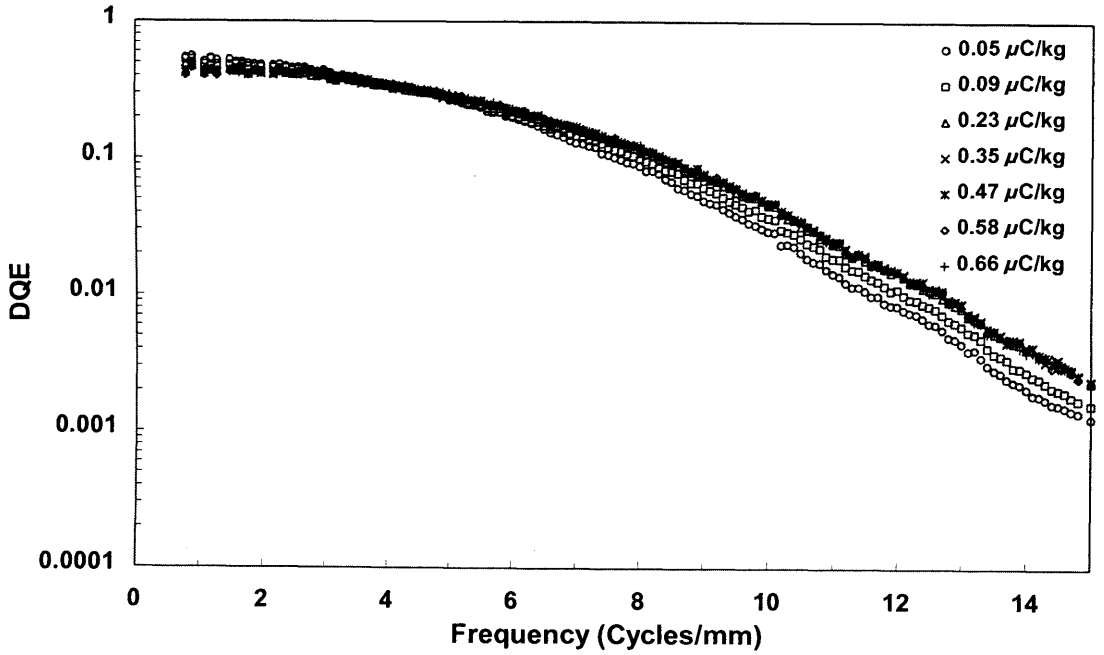

Figure 4.31. Semilog plot of the DQE of the Vanilla system configuration with 150 μm CsI (HS) and DQE with read noise removed DQE. The detector entrance exposure is shown in the plot.

The Vanilla system configuration with 150 μm CsI (HS) provides the most sensitive detector and has the smallest degradation at high frequencies over almost all exposures tested. We have to note that apart from the sensor sensitivity the scintillator characteristics are critical for high DQE. CsI with high light yield improves the DQE of the system, as it increases the sensitivity of the sensor. However, higher system gain will further reduce the maximum raw exposure that the senor can accommodate thus reducing the DR of the sensor.

4.3.2.10. Comparison of the sensors employed for the development of perfusion mammography

In order to compare the different system configurations and find the strengths and limitations in their performance they must be compared either at the same exposure or when they achieve quantum limited performance. As explained above in the 3T APS system configurations, DQE measurements of the system at higher exposures were not possible so we could not determine if the performance of the sensor was indeed quantum limited. However, since the electronic noise and the quantum noise are independent noise components we subtracted the electronic noise from the system noise as they are expressed through the NPS. This makes, within experimental error, the DQE independent of exposure (Zhao W *et al* 2004).

The DQE of each system, after removal of the electronic noise on the NPS of the 3T APS system configurations, is presented in Figure 4.32. The difference in the DQE close to zero frequency after removing the electronic noise, was marginal. Thus we can assume that for all systems at low frequencies under quantum limited conditions the DQE is from 0.45 to 0.50. It is interesting to note that this exposure level is almost a fifth of detector exposures used in mammography. This was evident from the 1D NPS and the small amplitude of the electronic noise as compared with the system quantum noise. For the 3T APS system configuration with 115 μm CsI below 5 cycles/mm, electronic noise affects the system DQE by less than 8%. However, at higher frequencies, the contribution of electronic noise becomes more significant and limits the DQE of both 3T APS system configurations. The contribution of electronic noise to the DQE of the Vanilla sensor is marginal and does not affect the performance of the systems above 0.23 μC/kg.

Finally, in order to demonstrate the effect of pixel size on the DQE the pixels were binned in a 2x2 configuration to achieve 50μm pitch and the DQE has been determined. The DQE of the 3T APS system configuration with 115 μm CsI, with read noise removed and after binning a 2x2 block of pixels, at detector entrance exposure of 0.44 μC/kg is shown in Figure 4.34. After binning (50 μm pixel pitch), the DQE close to zero frequency was ~0.51. The binned DQE at low frequencies is marginally increased and is equivalent to the DQE after read noise has been removed with the 25 μm pixel pitch. This was expected as at low frequencies; the system was quantum limited and binning could have only a marginal effect on the system DQE as the X-ray sensitivity of the system is the same. The small increase can be explained by the fact that binning smoothes the flat field images used for the determination of the NPS. The noise reduction was small as the binning has been performed at a small scale (2 x 2 pixels block). At higher frequencies, the DQE falls off more rapidly as it is modulated by the square of MTF.

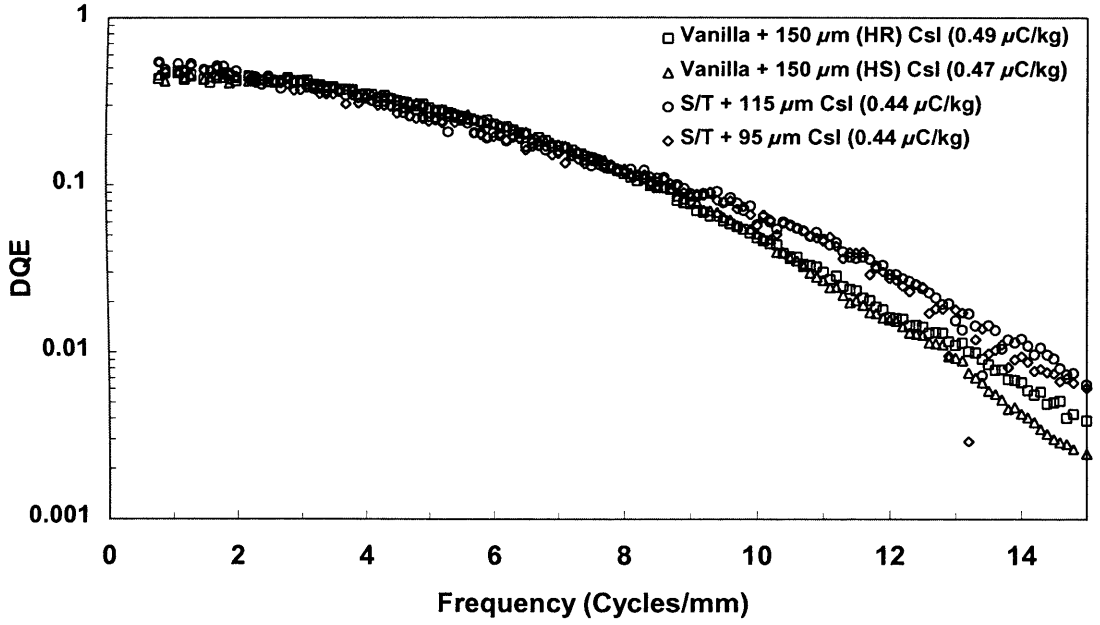

Figure 4.32. Semilog plot of the DQE of the 3T APS and Vanilla system configurations in the DQE 3T APS configurations the read noise has been removed. The detector entrance exposure is shown in the plot.

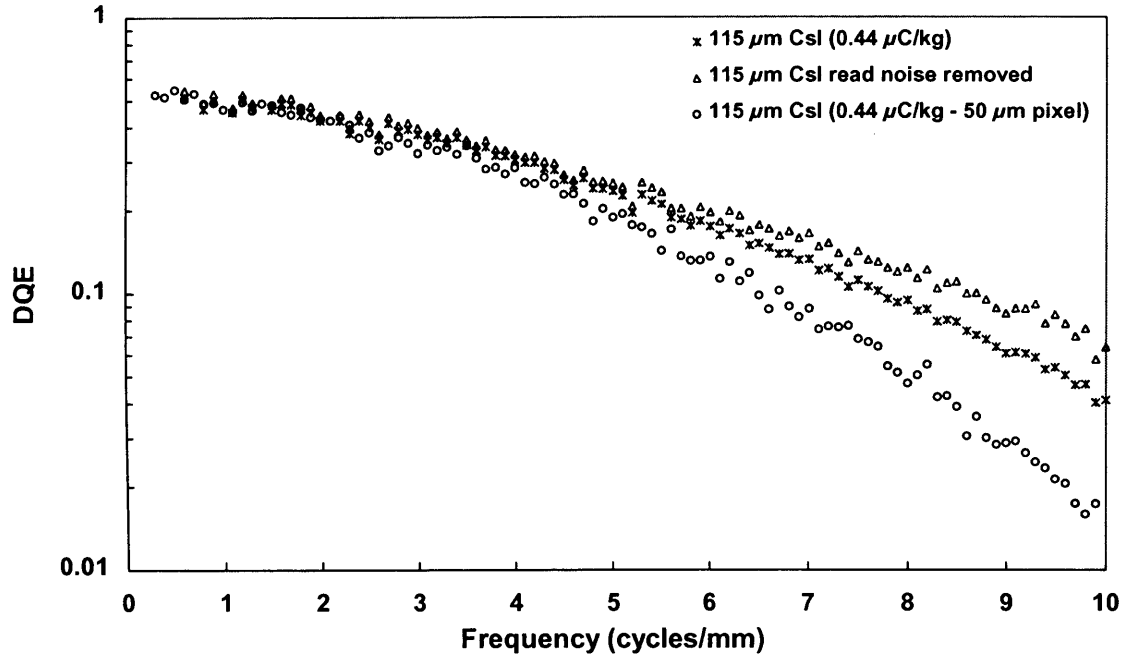

Figure 4.33. The DQE of the system configuration with 115 μm CsI, with read noise removed and after binning a 2x2 block of pixels, at detector entrance exposure of 0.44 μC/kg (1.72 mR).

Overall the response of all CMOS APS configurations has comparable performance with most of current detector technologies that have been evaluated in the mammographic energy range. Especially at low dose CMOS APS coupled to CsI scintillators can provide a very high performance detector for conventional and advanced digital mammography. The noise flour of this detector technology is an order of magnitude lower than the noise (~1000 electrons) in active matrix flat panel imagers (AMFPIs) found in clinical practice. It is interesting to note that the resolution is the more important parameter for the application of a sensor to conventional mammography. Conversely for low dose images, like those required for contrast enhanced mammography, the sensitivity of the system is more important. This is because the read noise of digital detectors tends to limit their application to the low dose requirements of this imaging approach. However spatial resolution should be as high as possible. Thus for the development of quantitative contrast enhanced mammography we choose to use the Vanilla sensor with the150 μm CsI (HR). This detector configuration provides a good compromise between resolution and DQE. In the last chapter we compare the performance of the sensors presented here with detectors found in the literature and

investigate the clinical potential of this detector technology for conventional and contrast enhanced digital mammography. In addition, at last chapter, based on the data presented we provide some suggestions about how the performance of CMOS APS based X-ray imagers can be further improved.

4.4 Summary

Empirical electro-optical and X-ray evaluation of three CMOS active pixel sensors has been performed. Optimisation in their performance has been achieved through the photon transfer curve. The sensors demonstrate the very good electro-optical properties currently available from this detector technology. Two of the three sensors presented had very good interacting quantum efficiency and were optically coupled to four different structured CsI:Tl phosphors. The two sensors resulted in five different system configurations that have been evaluated in the mammographic energy range. The sensors presented offer high resolution and an order of magnitude lower read noise as compared to AMFPIs. At 0.44 μC/kg detector entrance exposure the 3T APS system configurations presented approach quantum limited operation. The vanilla system configurations had quantum limited response at less than 0.23 μC/kg. This was due to both low noise and high system gain of the sensors employed in this study. Improved coupling efficiency with CsI scintilltors and higher dynamic range are some aspects of the sensors that should be studied further. The results suggests that this detector technology worthy a further investigation and can be useful to conventional and advanced mammography due to its high resolution low noise performance.

Chapter 5

Development of Quantitative Contrast Enhanced Mammography

5.1. Overview

This Chapter demonstrates how the dual energy approach is utilised for the isolation and quantitative assessment of contrast medium uptake from the breast. Data extracted from the simulated images were used for the optimisation of the acquisition parameters. The theoretical predictions are compared with experimental data and the effect of scatter radiation in quantitative imaging is discussed. The development of quantitative contrast enhanced mammography is presented.

5.2. Materials and Methods

Dual energy imaging, where separate low- and high-energy images permit the formation of material selective images can be used for the development of quantitative contrast enhanced mammography in order to isolate vascular contrast medium from overlapping tissue structures with increased complexity. The imaging of a compressed breast could be considered as a two material imaging problem, for example, the vascular contrast media thickness and the breast composition expressed as the ratio of adipose to glandular tissue. This allows for the estimation of the iodinated contrast medium thickness using two energy beams that straddle the iodine k-edge. For the evaluation of the clinical potential of this approach optimized conditions have to be achieved and quantitative analysis of the various imaging parameters have to be performed.

The important points that were considered include energy spectral pair formation, the quantitative assessment of iodine projected thickness at different breast thicknesses, assessment of scattered radiation, and the comparison of two different phosphors. These are presented here along with the construction of experimental phantom that incorporates flow. This was used to acquire experimental data and validate the theoretical predictions.

5.2.1. Filter material selection and spectrum formation

A Tungsten (W) tube was used throughout this work due to its high tube loading and high photon fluxes, even at high levels of filtration (Ullman G *et al* 2005). The formation of quasi-mono-energetic beams can be achieved by taking advantage of the k-edge of high atomic number materials. However, there are some practical aspects that restrict the selection of the appropriate filter material. Among these are the toxicity, uniformity, availability and the cost of the material. With these in mind, filtrating the low energy spectrum with iodine (contrast agent) provides a good compromise. For the high energy beam, although copper (Cu) does not have the k-edge in the energy range of interest (above 33.2 keV), we have chosen this material as it fulfils all the above practical aspects (Skarpathiotakis M *et al* 2002). In particular, Cu is very attractive due to its widespread availability. It can also be produced with very high purity, with extreme uniformity, and is low cost.

5.2.2. Dual energy imaging simulation and spectral pair optimisation

A program that generates simulated tungsten spectra was used to produce energy spectra for various tube settings. It has been shown that this program generates (Nowotny R *et al* 1985) W-target spectra with accurate shape and reasonable estimates of the fluence per exposure (Meyer P *et al* 2004). The numerical values for the differential energy intensity function were taken from Birch *et al* (1979). The spectra were generated using 0.8 mm Al filtration, which was equivalent to the inherent tube filtration of the W tube available in the lab, and scaled according to photon fluencies/mA for a 60 cm source to object distance (SOD). Then the spectra were attenuated by the selected filters (I_2 and Cu) to form the low and high energy spectra with smaller energy variance. The low and high energy spectra have been scaled so that the mean glandular dose from each beam is equal to 0.2 mGy, as was explained in Chapter 1 (section 1.4.2.) The spectral pair that provided the maximum SNR was selected as optimum.

The selection of 0.4 mGy total mean glandular dose was chosen so as to be roughly equal to the fifth of the mean glandular dose found in conventional digital mammography (~3.8 mGy per examination) (Chevalier M *et al* 2004). Using this dose level, 4-5 dual energy images could be acquired in order to measure the iodine up-take from breast

tumours. In all the plots presented throughout this chapter, the total mean glandular dose is equal to 0.4 mGy unless otherwise specified. The effect of the antiscatter grid in the rejection of the scatter and its subsequent increase in patient dose has not been considered in the present study.

In the simulation the breast was composed of glandular and adipose tissue. The mass attenuation coefficients have been determined from the elemental composition and density of the breast equivalent plastics (see next section) that were used to validate the theoretical predictions. In order to perform the spectral pair optimization, 3 mg/cm^2 of iodine projected thickness has been chosen. From the discussion in Chapter 1 it is apparent that, in contrast enhanced imaging, we are interested about the iodine projected thickness. Because of this, in the simulation the mass energy absorption coefficient of the iodine has been used and its thickness has been varied to provide projected thicknesses that comply with the clinical experience. Skarpathiotakis *et al.* (2002), based on Chang's study (1982), estimated that iodine projected thickness in breast is ≥0.75 mg/cm^2. The model parameters are summarised in Table 5.1.

Table 5.1. Summary of the parameters used in the dual energy simulation

Parameter	Type	Ref
Tube	Tungsten	Birch et al 1979
Filters	Iodine, Copper	Berger et al NIST, 1999
Breast Tissue	Adipose, Glandular	Berger et al NIST, 1999
Contrast Media	Iodine	Berger et al NIST, 1999
Detector	Cesium Iodine (CsI), Gadox Superfine (Gd_2O_2S)	Vedantham at al 2000 and Samei et al 2003

Table 5.2. Summary of the parameters used in the simulation (materials composition, density and thickness)

Material	Composition	Density (g/cm^3)	Thickness (g/cm^2)
Adipose	C(0.7141),O(0.1634),H(0.0978),N(0.0201),Ca(0.0013),Cl(0.00125)	0.941	1.88, 3.76, 5.65, 7.53
Glandular	C(0.6913),O(0.1766),H(0.094),N(0.0184),Ca(0.0175),Cl(0.0014)	1.048	2.10, 4.19, 6.29, 8.38
Contrast Media	I_2	4.93	0, 0.5, 1, 2, 2.5, 3, 4, 5, 6, 8, 20..100 · 10^{-3}
Cesium Iodine	CsI:Tl	4.51	45 and 67.5 · 10^{-3}
Lanex Regular	Gd_2O_2S:Tb	7.34*	68.1 · 10^{-3}

*packing density~0.6

The geometry of the simulated phantom was such that the two materials formed a ramp in order to incorporate all the possible compositions of breast (see Fig 5.2). This geometry was chosen in order to optimise the spectral pairs and theoretically assess the dual energy images. The iodine and background signals have been extracted from the regions incorporating different breast compositions. The simulated images have been formed by weighting the transmitted beam from the breast with the quantum efficiency of

the phosphor. In all the plots presented throughout this chapter, the system gain $\left(\overline{G}_D\right)$ was set equal to unity, unless otherwise specified.

In order to study the effect of the X-ray converter in dual energy imaging, both CsI:Tl and Gd_2O_2S:Tb have been used. The X-ray absorption ratios $\left(1-e^{-\mu_{att}t}\right)$ of a 45 mg/cm^2 (100 μm) and 67.5 mg/cm^2 (150 μm) thick CsI:Tl and 48.1 mg/cm^2 (65 μm) thick Gd_2O_2S:Tb are shown in Figure 5.1.

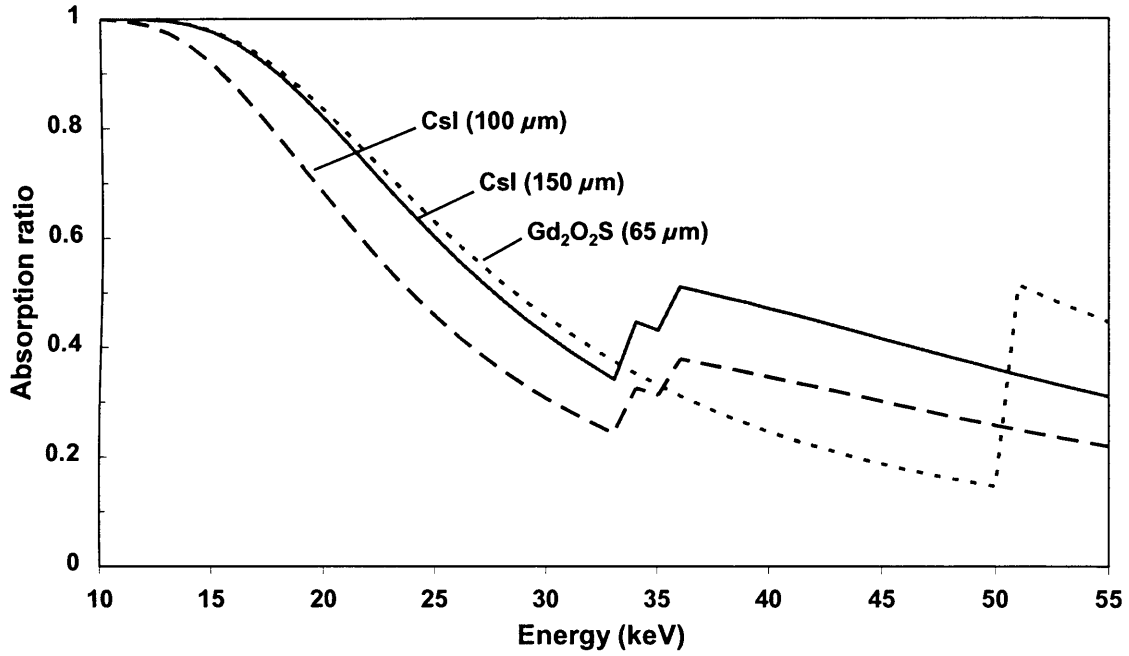

Figure 5.1. The absorption ratios of a 100 μm and 150 μm CsI and 65 μm effective thickness Gd_2O_2S. The k-edges of the two materials are seen at 32.2 and 36 keV for the CsI:Tl and at 50.2 keV for the Gd_2O_2S:Tb.

The choice of the above thicknesses was indicated from the scintillator thicknesses used in current clinical mammography units (100 μm CsI), as well as from the thicknesses of the scintillators in the detectors that we used in the experiments. For the Gd_2O_2S, 60% packing density has been used (Samei E *et al* 2003). At the energies below the k-edges of CsI the Gd_2O_2S has better absorption ratio. However, above the k-edges of the CsI at 32 and 36 keV, its absorption ratio increases significantly and exceeds that of Gd_2O_2S up to Gd_2O_2S k-edge (50.2 keV). The higher detection efficiency of CsI for X-rays generated with kVs close to its k-edges will result in much higher detected signals

than the Gd_2O_2S in the high energy image. This will increase the SNR in the final image in comparison with the image formed with the Gd_2O_2S phosphor.

Finally, in order to study the effect of scatter radiation in the iodine projected thickness measurements, scattered radiation has been added uniformly over the entire image assuming that, in the small area used, the scatter does not vary significantly. The scatter spectrum was simulated using the average transmitted spectrum and weighted by the detector response. As will be shown, the spectrum of the scatter - as long as it is reasonable - is not very critical. The scatter radiation was scaled as a fraction of the mean transmitted from the breast beam. The scatter to primary ratios found in mammography for a given breast thickness and composition were used to provide reasonable scatter amplitude. These ratios are readily available for a broad range of energies and have been estimated using Monte Carlo methods (Boone J M *et al* 2000). Concerning our work, the most important outcome of the Monte Carlo simulations apart from the amplitude of the S/P ratios, is that in the energy range around the iodine k-edge the difference in the S/P ratios is marginal. Thus in the simulations the scatter radiation from the low and high energy beams have been scaled using the same scaling factor. This resulted in an average difference between the S/P ratios from the high-energy beam from the S/P ratios and the low-energy beam equal to 0.026 (2.6%).

5.2.3. Experimental dual energy imaging

An experimental breast equivalent phantom that incorporates flow has been constructed in order to validate the theoretical predictions, and perform quantitative contrast medium kinetics measurements. The phantom is composed of overlapping layers of glandular and adipose breast equivalent plastics (014A, Ciris Tissue Simulation Tech.). Figure 5.2 shows the geometry and composition of the phantom. The phantom thickness was equivalent to a 4 cm thick compressed breast. On top of the breast equivalent plastic a 7 mm PMMA slab with a cylindrical bath of 2 mm depth and 6 mm diameter was placed. The center of the cylinder was placed at the middle of the ramp, 'A'. This geometry provides a way to estimate the degree of iodine isolation under all possible combinations of adipose and glandular tissue in the breast. In the bath, which represents a tumour, different concentrations of iodinated contrast medium solution can be injected.

Six different iodine projected thicknesses (0, 0.5, 1, 2, 3, 4, 6 and 8 mg/cm^2) were used for the assessment of the technique. A depth of 2 mm in the PMMA was chosen in order to have a size similar to tumours that develop angiogenesis. Tumours smaller than 2 mm to 3 mm do not demonstrate high microvessel density, thus the uptake of contrast medium is limited in tumours of this size (Miles K A *et al* 2003).

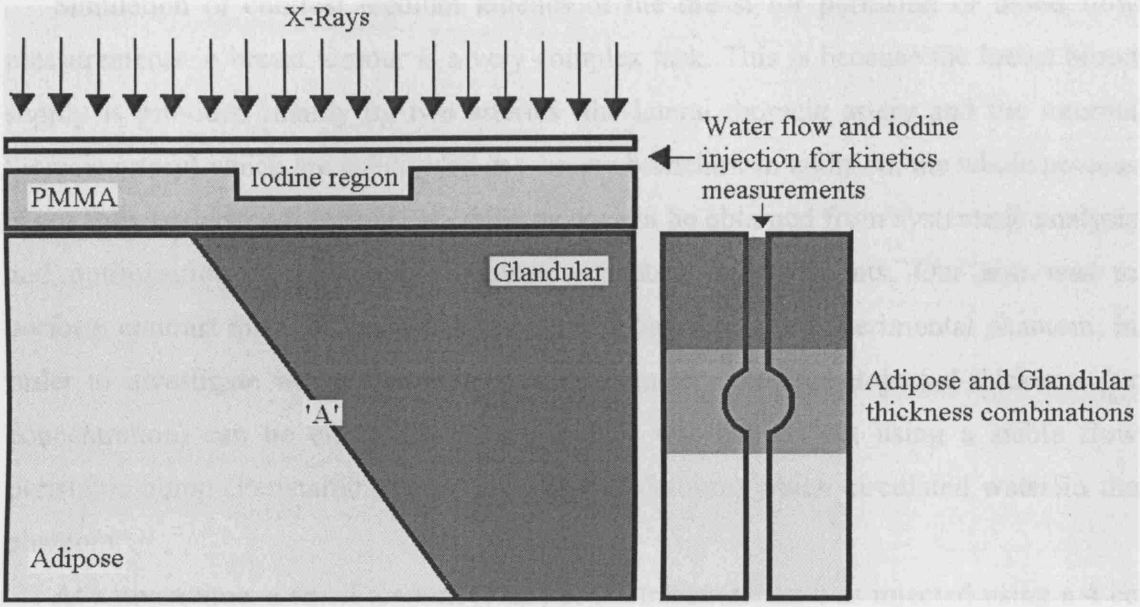

Figure 5.2. The breast phantom geometry and composition. To the left is the side view and to the right is the top view of the phantom (the two views are not at the same scale).

The low and high energy filters were mounted on a remotely controlled stepper motor. This ensured that the filters were always placed at exactly the same position during and after acquisition so that a flat field correction was sufficient to remove any spatial inhomogeneities in the filters. There was no antiscatter grid and the source to detector distance (SDD) was fixed at 65 cm. The field of view has been restricted to 10 cm using collimation. Phosphor and X-ray field nonuniformities were removed before any post-processing of the images by flat fielding, which was always performed for the two energy images independently. This was because both nonuniformities are energy dependent.

In this study two detectors were used. One was the CMOS APFPI (Vanilla) and the other was a:Si AMFPI. The a:Si AMFPI was used as a reference detector because it is a detector that has been previously used in clinical practice. This detector had a 127 μm pixel pitch and was optically coupled to a Lanex Regular (Eastman Kodak) turboid

phosphor screen (PaxScan 4030R, Varian Medical Systems). Its physical performance evaluation has been preformed by Samei *et al* (2003). The second detector was the Vanilla sensor with the 150 μm CsI (HR).

5.2.4. Contrast medium kinetics measurements

Simulation of contrast medium kinetics of the breast for perfusion or blood flow measurements in breast tumour is a very complex task. This is because the breast blood supply is provided mainly by two arteries (the lateral thoracic artery and the internal thoracic artery) which are subdivided in to many branches. In addition, the whole process is not fully understood. Insight into this process can be obtained from systematic analysis and optimization of quantitative contrast enhanced measurements. Our aim was to perform contrast medium kinetics measurements based on our experimental phantom, in order to investigate whether the temporal differences in iodine projected thickness (or concentration) can be effectively detected. This was carried out using a stable flow peristaltic pump (Peristaltic Pump 3200, Welch Vacuum) which circulated water in the phantom.

At a given time, a small amount (1 ml) of contrast medium was injected using a 4 cc syringe. The flow was measured by volume sampling and found to be 20.4 ml/min. The contrast medium kinetics was measured by acquiring the low and high energy images in two separate experiments performed under identical conditions. The kinetics were measured using i) an open flow circulation and ii) a closed flow circulation. In the first, the contrast medium after its first passage was disposed and, in the latter, the contrast medium after its injection was circulated in the flow circuit. By choosing these two different flow configurations we could simulate the two out of the three contrast media kinetics curves found in clinical conditions. The enhancement curves in tumours from MR studies have been classified into three types (Kuhl C K *et al* 2000). Type I curve that shows a gradually increasing enhancement and was simulated with the closed circulation. Type II curve shows a rapid increase in enhancement and then plateau. Type III curve shows a rapid increase in enhancement with a rapid washout and is indicative of malignancy. This curve was simulated using the open flow circulation.

It should be noted that in the kinetics measurements we did not simulate the heart as this would require a pulsatile pump. However, the flow rate was adjusted so as to provide flow rates similar to those found in breast and at the same time provide a good mixing of the contrast medium with the circulated water before the contrast medium reaches the cylindrical bath that simulated the tumour.

5.3. Results and discussion

5.3.1. Spectral pair optimisation

The spectral pair optimisation was based on the methodology developed in Chapter 1. The system gain has not been used at the spectral pair selection. The optimisation has been performed for both X-ray converters (CsI and Gd_2O_2S). Figure 5.3 shows the iodine signal to noise ratio (SNR) as a function of tube kVp.

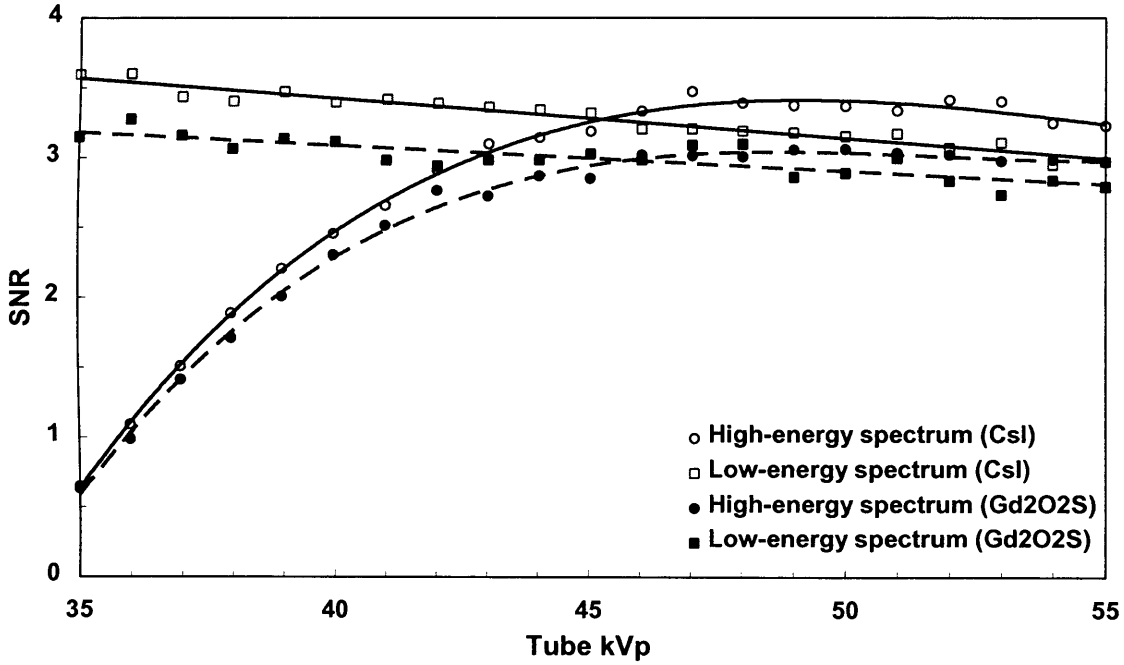

Figure 5.3. The SNR of the iodinated region as a function of tube kVp for the two different phosphors and for the two energy beams. The projected thickness of iodine was 3 mg/cm^2, the breast thickness 4 cm and the total mean glandular dose was set to 0.4 mGy. The phosphor's thickness was 100 μm and 65 μm for the CsI and Gd_2O_2S respectively. The fits to the simulated data points are also presented.

It is evident from Figure 5.3 that, for both converters, the high energy beam produces an increase in the SNR as a function of tube voltage up to a maximum value (48-50 kVp).

This increase in the SNR is because the high energy filtration is not based on the k-edge of a material; this causes the effective energy to vary with kVp more than in the low energy beam that is filtered with a k-edge material. Therefore, at low kVp where a high fraction of the beam is below the iodine k-edge, the SNR is low. At higher kVp there is a decreasing trend as the mean energy of the spectrum is moving further away from the iodine k-edge. This trend is less pronounced for the Gd_2O_2S due to the absorption edge of Gd (Fig 5.1) at energies above 50 keV. The SNR for the low energy beam decreases proportionally with the increase of the low energy beam component above the k-edge. At higher kVp the trends are similar to the trends found with the high energy beam.

Under clinical conditions the low and high-energy images should be acquired rapidly thus the small voltage separation is essential in order to switch from low to high energy beams (Ducote J L *et al* 2007). In addition, at higher tube voltages, high tube currents can be achieved from the tube. Thus for the low energy beam we chose 44 kVp as optimum and, for the high energy beam, we chose 48 kVp. It is interesting to note that since the spectra were scaled according to mean glandular dose which, in turn for the kinetics studies should be equivalent to conventional mammography the maximum tube power output will not differ significantly to "single-shot" dual energy imaging. Tube power consumption should be kept as low as possible as it is directly linked with the lifetime of the tube. Thus the low-energy beam was filtered with 3.25 mm of contrast agent (Iohexol, with 350 mg of iodine per milliliter) resulting in iodine projected thickness equal to 0.245 mm. The high energy beam was filtered with 0.3 mm of copper (Cu). These thicknesses of filtration provided reasonable tube loads. In Table 5.3 the parameters of the two beams are shown and Figure 5.4 shows the simulated optimum spectra pair normalised to unity.

Table 5.3. The spectral parameters derived from the simulation for the low and high energy beams

Parameter	Low-Energy Beam	High-Energy Beam	Units
Tube Voltage	44	48	kVp
Tube Current	7.2	26.5	mAs
Filtration	0.245 (I_2)	0.3 (Cu)	mm
Mean Energy	28.5	37.5	keV
Percent of initial spectra used	13.7	7.2	%
Percent above/below K-edge	7.1	20.9	%

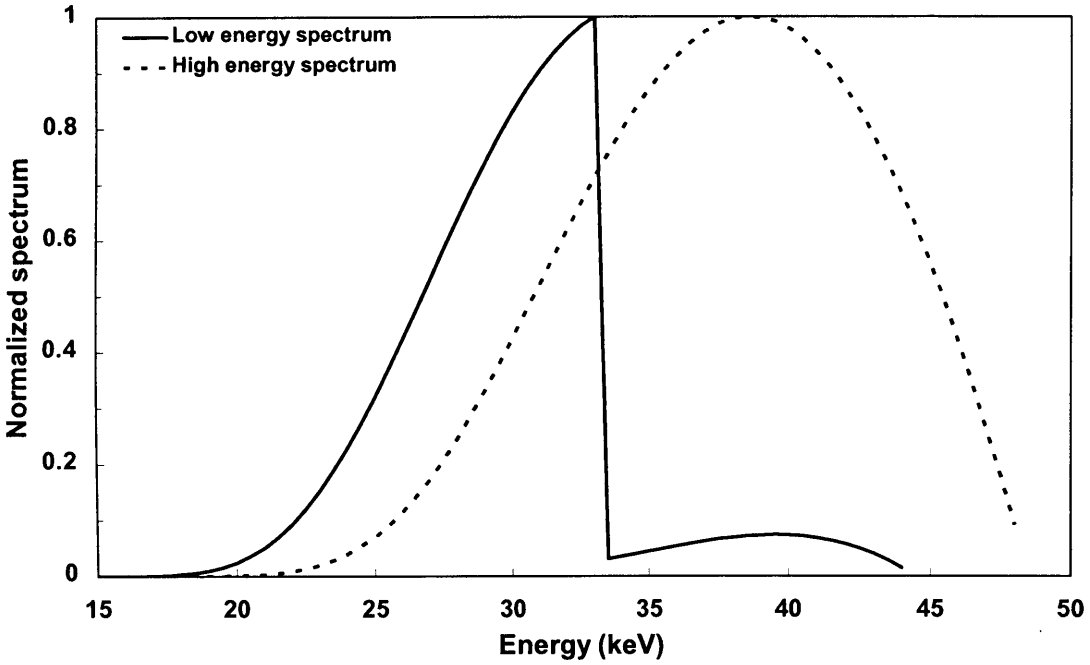

Figure 5.4. Normalised to unity simulated low- and high- X-ray spectra using a tungsten x-ray tube. The parameters of the spectrums are given in Table 5.3.

5.3.2. Low- and high-energy beams ratio assessment

The assessment of low- and high-energy spectral fluxes has been performed by studying the dependence of the SNR as a function of the ratio of the mean glandular dose of the high energy $\left(mGd^{h}\right)$ to the total mean glandular dose $\left(mGd^{h} / mGd^{tot}\right)$. This ratio is very important as it will provide optimum distribution of mean glandular dose in the two images thus maximising the dose efficiency during the image acquisition. As can be seen from Figure 5.5 there is a relatively strong dependence of the SNR with the distribution of the mean glandular dose between the low and high energy beams. This is because the iodine signal is mostly affected by its radio-opaque k-edge that is at the high energy beam. Further increase of the mGd^{h} / mGd^{tot} ratio, causes a reduction of the low energy beam fluence, which results in both high residual and quantum noise leading to significant reduction of the iodine SNR. The optimal mGd^{h} / mGd^{tot} ratio, as was determined from fits of the simulated data for 4 cm breast, was 0.60 for both CsI and Gd_2O_2S. However, for mGd^{h} / mGd^{tot} between 0.4 and 0.7 the difference is small. For given iodine SNR the optimum mGd^{h} / mGd^{tot} is independent of breast thickness and

composition. However, if the mGd^{tot} is kept constant, for thicker breasts the optimal ratio is slightly decreased (0.55) for both X-ray converters. As it was expected from the x-ray absorption ratios of the two phosphors (Fig. 5.1), the SNR of the CsI is higher than the Gd_2O_2S phosphor, and if a thicker (150 μm) CsI is used then the difference increases further.

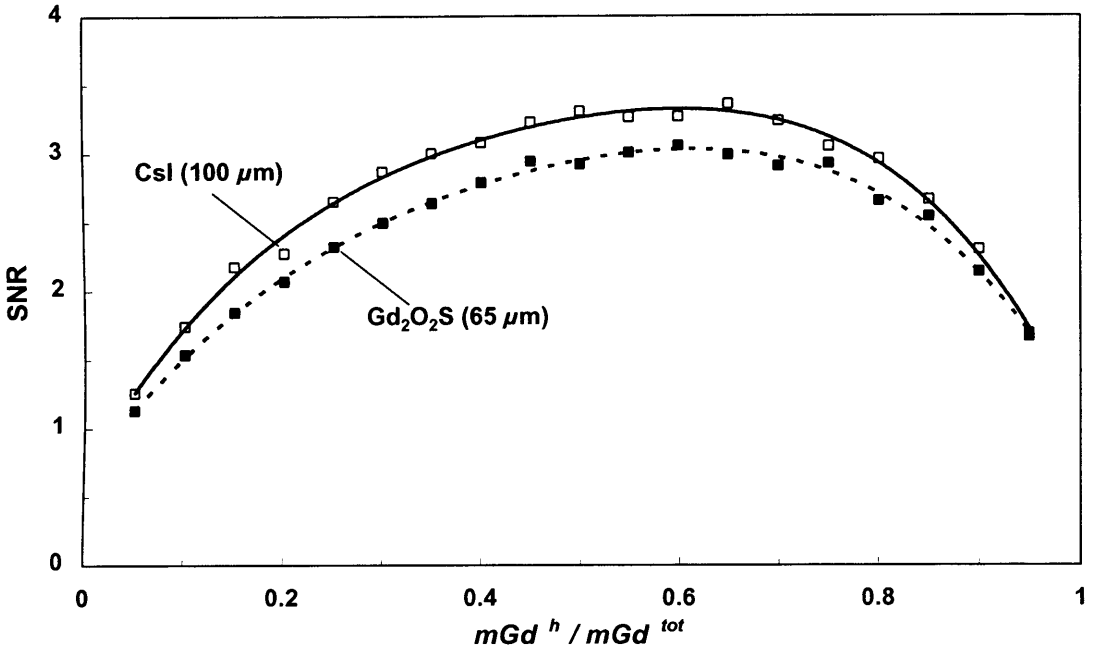

Figure 5.5. The SNR as a function of the ratio of the mean glandular dose of the high energy beam to the total mean glandular dose mGd^h / mGd^{tot} for 4 cm. The phosphors used are shown in the plot. The projected thickness of iodine was 3 mg/cm^2 and the total mean glandular dose was 0.4 mGy. The fits to the simulated data points are also presented.

5.3.3. Iodine isolation and image quality metrics

The spectral pair optimisation presented above was based on the maximisation of the iodine SNR. However, as mentioned in Chapter 1, the SNR (Eq 1.17) can be used as an efficient image quality descriptor in dual energy imaging only if complete tissue suppression has been achieved. Otherwise signal difference to noise ratio (SDNR) should be considered (Eq.1.18). Figure 5.6 shows the SNR and SDNR (excluding the background noise) as a function of iodine projected thickness. For the range of iodine projected thicknesses used, both have almost identical slope with a marginal offset difference. Both SNR and SDNR scale linearly (there is no physical meaning in the

slope) with the iodine thickness. For zero iodine thickness both were almost zero indicating that the background anatomic noise has been effectively suppressed. The small offset signal that appears in the SNR is related to errors caused by the linear subtraction. However, the error of the linear subtraction is remarkably low (~0.13 mg/cm^2 for 4 cm thick breast), indicating the good accuracy provided by the linear subtraction.

Therefore, we can say that the "equality" of SNR and SDNR signifies that the subtraction employed effectively suppresses the tissue structure, while the iodine signal is preserved. Thus, in material selective imaging the SNR provides an efficient descriptor of image quality. In addition, the SNR imposes fundamental limits in the detection of iodine projected thickness for a given breast thickness and mean glandular dose.

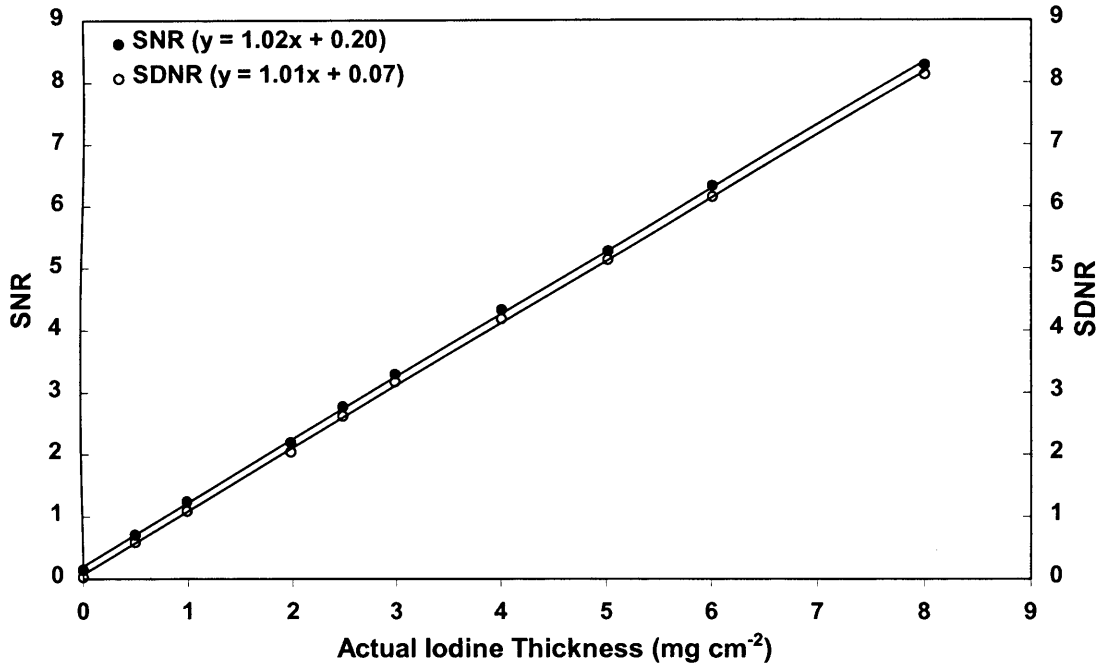

Figure 5.6. SNR and SDNR as a function of iodine projected thickness for 4 cm breast thickness at 0.4 mGy total mean glandular dose. The plot has been extracted from the simulated images using CsI phosphor with 100 μm thickness at 127 μm detector pixel size. The correlation coefficient with the linear regression was 0.999. Linear regressions were used to estimate the difference between SNR and SDNR as image quality descriptors.

In the material selective image, SNR will depend on the area of the detail and not on the pixel signal and noise. However, for accurate diagnosis using perfusion measurements, along with temporal resolution, spatial resolution is needed. The iodinated

areas in the breast are not uniform ("Rim-like" enhancements) and the fact that their morphology is crucial for accurate diagnosis, suggests that the SNR should be considered at pixel level for accurate spatio-temporal iodine selective breast imaging.

Thus optimisation in the acquisition parameters and the associated trade-offs should be tied to the SNR, with the signal averaged over a uniform area as it was suggested from Eq. 1.1. The minimum SNR for efficient detection as determined from Rose *et al* (1953) is 5. Thus SNR equal to 5 will be adopted here as a threshold when spatial resolution is the primary interest. The SNR equal to 3 can also be considered as an adequate threshold when temporal resolution is the primary interest. This is because in the iodine selective image there will be no structural noise and usually the enhanced areas are big (≥2 mm) with respect to the pixel size (~100 μm), as opposed to microcalcification selective imaging (Kappadath S. C. and Show C. C. 2005).

It is interesting to note that, with the parameters used, the iodine thickness which provides SNR=5 is 5 mg/cm^2 (Fig. 5.6). This is relatively high value considering the iodine projected thickness (~2 mg/cm^2) reported for contrast enhanced mammography (Jong R A *et al* 2003 and Skarpathiotakis M *et al* 2002). In the next section the relevant trade-offs in order to increase the "detectability" of the iodine is presented.

Figure 5.7 shows the SNR for the CsI (100 μm and 150 μm thick) and Gd_2O_2S (65 μm thick) phosphors as a function of the actual iodine projected thickness. As was expected from the absorption ratios (Fig. 5.1), the SNR of the 150 μm thick CsI was the higher and the SNR for Gd_2O_2S was the lower. Note that the offset at zero iodine signal is the same irrespective (~0.13 mg/cm^2) of the phosphor or absorption ratio of the detector used.

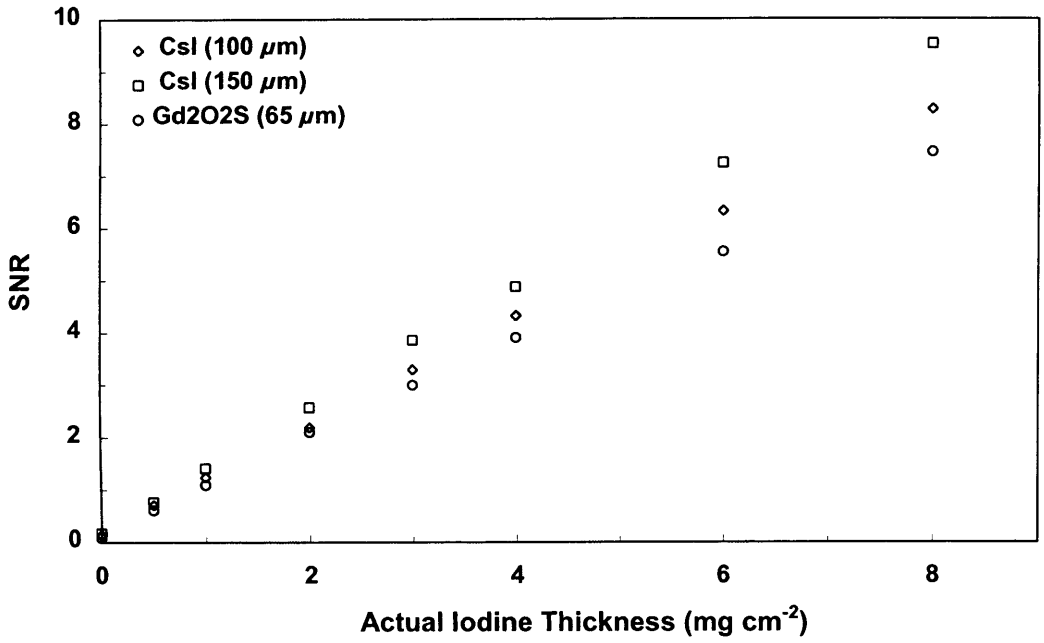

Figure 5.7. The SNR for the CsI (100 μm and 150 μm thick) and Gd2O2S (65 μm thick) as function of the actual iodine projected thickness. The breast thickness was 4 cm and the mean glandular dose was 0.4 mGy at 127 μm detector pixel size.

5.3.4. Effect of pixel size, system gain, and mean glandular dose on the SNR

The uncertainty in the estimation of iodine projected thickness depends on the integrated signal from the detector photon fluence. This in turn, is proportional to the mean glandular dose or the breast entrance exposure. Thus, the higher the mean glandular dose the more accurate the estimation in the iodine projected thickness measurement will be. In addition, the integrated photon fluence is proportional to the pixel size (Eq 1.1). Thus the noise in the dual energy image will be inversely proportional to the detected photon fluence (Eq. 1.16). Finally, the system gain will define the accuracy of the system in recording the integrated photon fluence. As explained above, the signal to noise ratio (SNR) can be used as an efficient estimator of minimum detectable iodine signal and provides the means to quantify the above dependences.

Figure 5.8 shows the SNR as a function of pixel size and mean glandular dose using CsI phosphor with 100 μm thickness for 3 mg/cm^2 iodine projected thickness at 4 cm thick breast. The SNR at constant total mean glandular dose (0.4 mGy) scales linearly with the pixel size, as can be seen from the linear regression. This is because in the

material selective image the signal will be constant and the SNR or the noise will be inversely proportional to the pixel size $(\sigma \quad 1/a_{pix})$. The SNR squared scales linearly with the total mean glandular dose indicating the independence of the ratio SNR^2 / mGd^{tot} from the exposure. Thus the higher the mean glandular dose the smaller the uncertainty in the iodine thickness measurements will be. In the same figure the SNR equal to 3 and 5 is indicated with vertical lines.

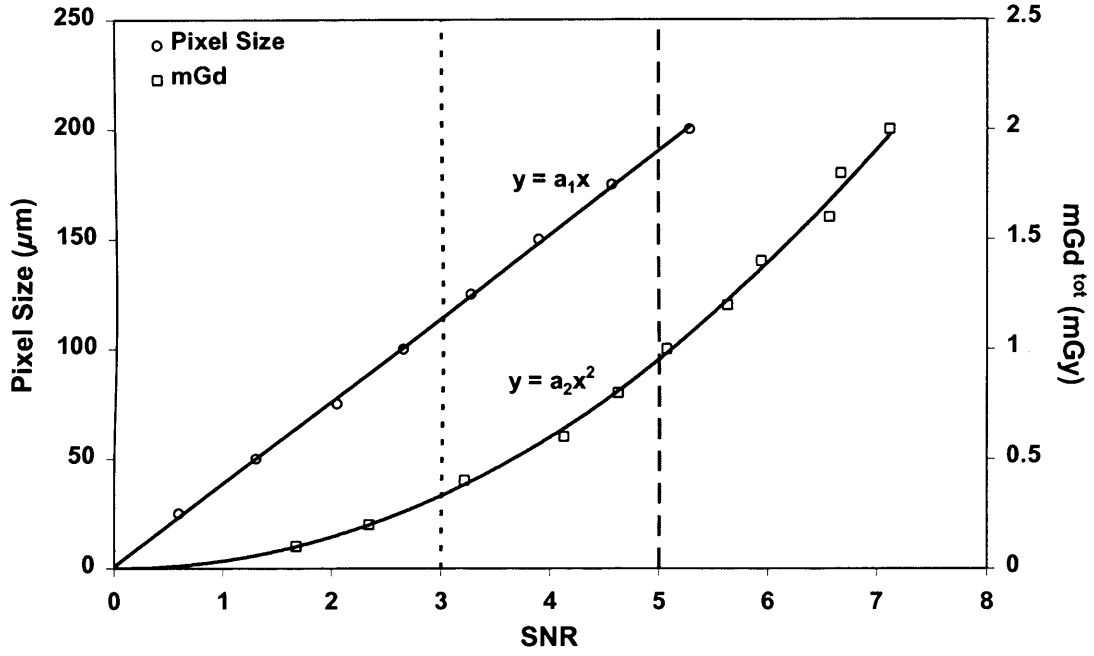

Figure 5.8. SNR as a function of total mean glandular dose (at 127 μm pixel size) and pixel size (at 0.4 mGy, mGd). The plot has been extracted from the simulated images using CsI phosphor with 100 μm thickness at 3 mg/cm^2 iodine projected thickness. The correlation coefficient with the linear regressions was 0.999. The linear regressions were used to estimate the dependence of pixel size and mean glandular dose in the dual energy image as a function of SNR.

Figure 5.9 shows the SNR as function of system gain. The system has been expressed as a number of electrons that the detector reads per keV of deposited energy on the X-ray converter. The three different curves shown (Fig 5.9) are for 1 mg/cm^2, 2 mg/cm^2, and 3 mg/cm^2 of iodine projected thickness. The strong dependence of the system gain with the SNR indicates the importance of the system gain in eliminating the uncertainty in the iodine projected thickness estimation. Very low gains indicate quantum sinks in the detector, and limiting its application to iodine selective imaging in the breast. This

explains why the first attempts in the 1980s (Chang C H J *et al* 1981, Watt C *et al* 1985) to perform contrast enhanced breast imaging using detectors with low gains was not fruitful. For the 127 μm pixel used it seems that system gains between 1 e^-/keV and 5 e^-/keV can provide the required conditions to perform iodine selective imaging with the required accuracy and sensitivity. It is interesting to note that the sensitivities measured for the APFPIs presented (Figs. 4.14 and 4.15) are between 2 e^-/keV and 10 e^-/keV (assuming that the mean energy of the Mo/Mo tube at 30 kVp is approximately 19 keV). However, the dependency of SNR with pixel size (Fig. 5.8) should not be underestimated. Finally, gains above 10e^-/keV do not provide any additional benefit unless a smaller pixel size is used. It should be noted that high gain systems might be susceptible to high levels of X-ray converter nonuniformities (fixed pattern noise).

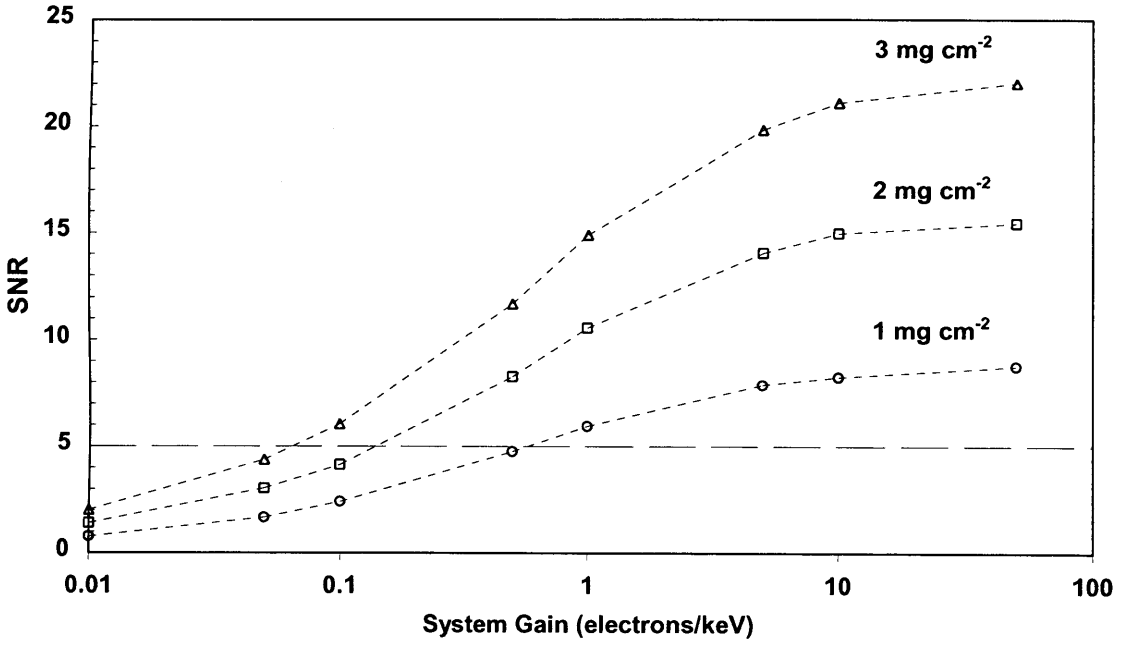

Figure 5.9. Linear-log plot of the SNR as a function of system gain expressed in electrons read by the detector per keV of energy deposited on the phosphor. The plot has been extracted from the simulated images using CsI phosphor with 100 μm thickness and 127 μm pixel size for 3 mg/cm^2 iodine projected thickness. The breast thickness was 4 cm and the total mean glandular dose was set to 0.4 mGy.

From the above analysis, and by considering that the pixel size is very small with respect to the iodinated areas, it is evident that for the development of quantitative

contrast enhanced mammography the most crucial requirement of the system is the sensitivity rather than the resolution. It is important to note that using the simulations one should take into account the system, additive electronic noise, blurring, resolution and influences of the human visual system in order to make any predictions about absolute visibility. However, based on the high score of sensitivity achieved in MR studies using 0.65 mm x 0.45 mm x 3 mm voxel size (acquisition time 2 min/image) (Pediconi F *et al* 2007), we can say with confidence that the system blurring and resolution is not a detrimental factor in the development of perfusion mammography. Even with 200 μm pixel size the Nyquist frequency will be at 2.5 lines/mm, which is higher than the smallest voxel dimension in the MR imaging. In addition, the total additive electronic noise can be neglected since less than 100 electrons can be achieved with APFPIs.

Thus, if a system with high gain is not used, higher temporal resolution can be achieved at the cost of lower spatial resolution and *vice versa*. Taking into account that a compromise in the spatial resolution is acceptable, higher pixel sizes (>50 μm) can be used in order to increase the iodine SNR. Accurate enhancement thresholds and the trade-off between pixel size, SNR, and mean glandular dose can be further determined with the aid of clinical data (not available at the time of this study) in order to tighten the optimisation to specific requirements. However, a system with high gain imposes that a minimum compromise is feasible. This reveals the strong potential of APFPIs for high accuracy spatio-temporal medical imaging and in particular for the development of contrast enhanced mammography.

It is worth pointing out that the spatial and temporal resolution trade-offs between contrast enhanced MR breast imaging and X-ray breast imaging are completely different in nature. In particular, in MR studies the temporal resolution is limited by the acquisition hardware. Thus any decision about spatial and temporal resolution should be taken before the image acquisition. In X-ray imaging the temporal resolution is limited by the mean glandular dose not by the hardware. Thus, in X-ray imaging high spatial resolution images can be acquired very rapidly and then the trade-offs between resolution and sensitivity can be performed along with the post processing of the dual energy images. This property of X-ray digital detectors reveals one of the main benefits of quantitative contrast enhanced mammography. It is important to stress that the minimum pixel signal

should always be above signal levels where the performance of the detector is not affected by the detector electronic noise

5.3.5. Iodine projected thickness measurements

The determination of the maximum enhanced signal and the rate of enhancement in physical units are important requirements for the development of quantitative contrast enhanced mammography. This can be obtained from the measurement of the projected thickness of the iodinated vascular contrast agent expressed in mg/cm^2. Figure 5.10 displays the measured (detail) iodine projected thickness from the iodine selective image as a function of the actual iodine projected thickness for different breast thicknesses using CsI phosphor. The data have been extracted from the simulated images. Similar results have been obtained with the Gd_2O_2S:Tb phosphor. Thus, for clarity these have been excluded from the plot. The measured iodine projected thickness scales linearly with the actual iodine thickness irrespective of breast composition and thickness, as can be seen from the linear regressions. The slope equal to one signifies that the detail iodine thickness can be measured from the iodine selective image. Thus, the linear subtraction of logarithm transformed images provides accurate measurements of the iodine projected thickness. In addition, at the range of iodine projected thicknesses used, the measurements are not affected by the beam hardening. Error bars in the figures with iodine projected thickness measurements indicate the standard error of the measurement, unless the size is too small to be visible. In the simulated images (Fig. 5.10) the standard error in the measurement of iodine thickness was approximately equal to 0.14 mg/cm^2 when the system gain was set equal to unity.

As explained above (Fig. 5.6), the small offsets in linear regressions (expressed in mg/cm^2) are related to the errors associated with the linear subtraction and is independent of exposure. Thus the thicker the breast the higher the offset in the detail iodine projected thickness. We expect that nonlinear subtraction could further suppress this value. However, as can be seen, it is reasonably small and will not be considered as significant in the present study.

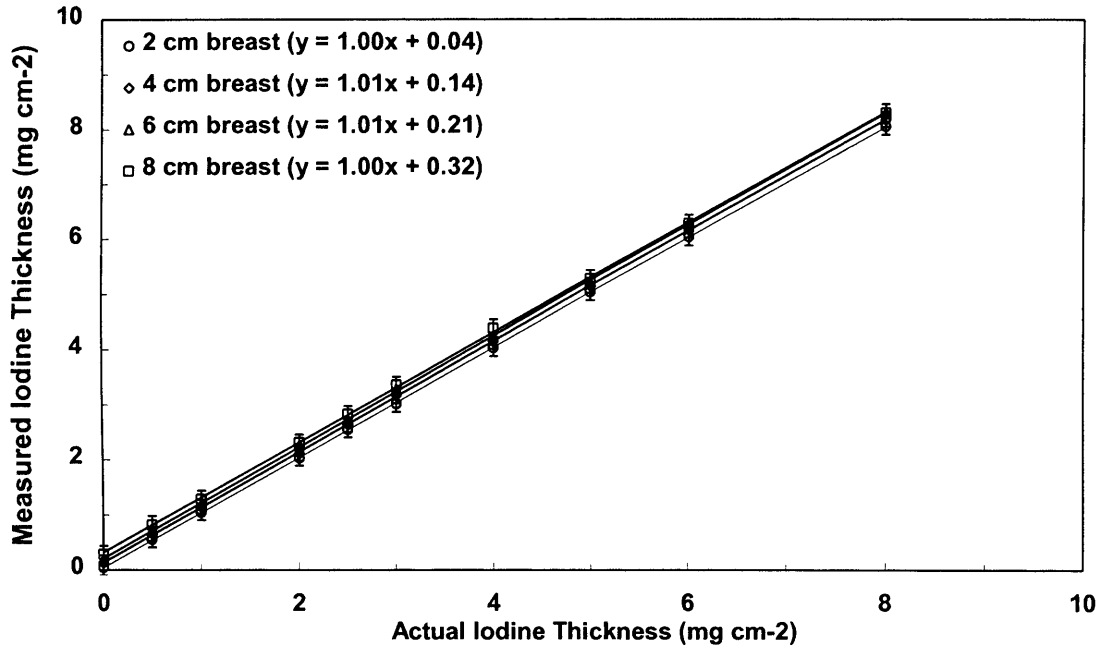

Figure 5.10. Iodine thickness measurement for 4, and 8 cm breast thicknesses for Gd_2O_2S:Tb and CsI:Tl converters. The mean glandular dependent exposure was fixed at 0.4 mGy for all breast thicknesses. The pixel size was 127 μm and the phosphor thicknesses was 100 μm thick CsI:Tl. The correlation coefficient with the linear regression was 0.9999.

It is interesting to note that nonlinear response due to beam hardening becomes apparent at very high iodine thicknesses (40 mg/cm^2) and is more pronounced with the Gd_2O_2S phosphor. These deviations from linearity (slope<1) are related to the beam hardening and originated from the presence of the iodine in the high-energy beam path. This is because in the high-energy beam, the spectrum is broader and its attenuation from the iodine higher. Although the beam hardening is also present when employing the CsI phosphor it becomes more apparent at much higher iodine projected thicknesses than 40 mg/cm^2. This might be due to the higher quantum efficiency of the phosphor at energies close to the k-edge, which compensates for the small changes in the mean energy of the beam. However, under clinical conditions the dilution of the contrast agent is of the order of 1/40 of the injected concentration, leading to a concentration less than 10 mg/ml, for contrast media with 350 mg of iodine per milliliter. Thus, there is no reason to study iodine projected thicknesses above 10 mg/cm^2. Therefore, we can say that for the spectral pair selected, and at iodine projected thicknesses relevant to clinical values, beam

hardening does not introduce nonlinearities in the measurement of iodine projected thickness.

5.3.6. Effect of scattered radiation in the iodine projected thickness measurement

The above analysis formed the basis to optimise the acquisition parameters, the post-processing of the images, and the detector requirements for the development of quantitative contrast enhanced mammography. However, under realistic conditions the scatter radiation will be present and will inflate the measurements of the transmitted beams through the breast made by the detector. This will lead to erroneous measurement of the line integrals, leading to false estimation of the iodine projected thickness and breast composition.

In order to study the effect of scattered radiation, scatter radiation has been added to the simulated images, as explained in section 5.2.2. Based on the geometry of the simulated breast, the S/P ratios varied across the breast according to its composition. Higher S/P ratios were found beneath the more attenuated materials (iodine and glandular tissue). Boone *et al* (2000) has shown, using Monte Carlo simulations, that at the energy range around the iodine k-edge the scatter to primary ratio is reasonably constant and approximately 0.45 for a 4 cm thick breast composed of 50% glandular and 50% adipose tissue. Thus the scatter radiation has been scaled so that the average S/P ratios from the low- and high- energy images over the entire image were equal to 0.45. The average values of the S/P ratios have been determined in the absence of iodine.

It was established in Chapter 1 (section 1.2.3) that in the presence of scatter the measured iodine projected thickness will be erroneous and will vary in a nonlinear manner depending on the S/P ratios beneath adipose tissue and breast. Thus the following two approaches have been applied to the simulated data in order to compensate for the nonlinearities introduced from the scatter radiation. In the first, the scatter signal but not the Poisson distributed noise, has been removed from the low- and high-energy images before any post-processing and the detail iodine signal has been measured. In the second, the detail projected thickness has been corrected from the dual energy image using the Eq. 1.14. Figure 5.11 shows the detail signal as a function of actual iodine signal in the absence of scatter, in the presence of uniform distributed scatter, and when

the two different approaches to compensate for the scatter have been applied. As can be seen in the presence of scatter, the deviations from the actual iodine thickness measurements are nonlinear. In addition, although the scatter contribution is the same in all images, at higher iodine thicknesses it becomes more significant due to low detected exposure, resulting in a higher scatter fraction (high S/P ratios). The data of no scatter, scatter corrected ad scatter removed are overlapping.

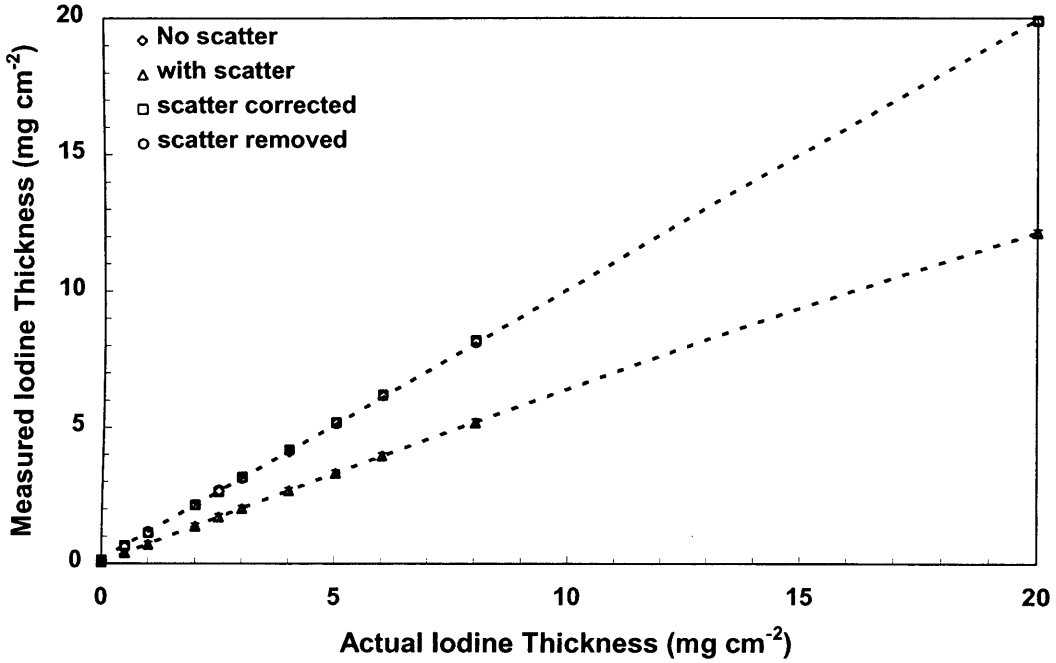

Figure 5.11. Measured iodine signal as a function of actual iodine signal in the absence of scatter, in the presence of uniform scatter and when two correction methods have been applied. The data have been extracted from the simulated images using CsI phosphor with 100 μm thickness and 127 μm pixel size. The breast thickness was 4 cm and the total mean glandular dose was set to 0.4 mGy. The data points from the measured iodine thickness in the absence of scatter and when two correction methods have been applied are overlapping. The correlation coefficient with the linear regression was 0.9999 and was performed for the scatter corrected data.

From Figure 5.11 it is evident that both approaches applied to compensate for the scatter were able to restore the measured (detail) iodine thickness to the actual iodine thickness. Based on the effectiveness of the scatter correction approach it is apparent that the deviations from linearity depend on the S/P ratios and not on the actual scatter fraction in the images. Thus the analytical expressions derived in Chapter 1 provide an accurate description of the effect of scatter in dual energy imaging. It is interesting to

note that using the scatter correction approach based on the analytical expression, one needs to know the S/P ratios on a pixel-by-pixel basis and not the actual scatter fraction in the images.

Although, the above corrections provide accurate iodine thickness measurements, it is interesting to study their effectiveness to detect the detail iodine thickness. Figure 5.12 shows the SNR of 3 mg/cm^2 at different iodine S/P ratios in the presence of scatter when scatter has been corrected and when the scatter has been removed, normalised to the SNR in the absence of scatter. In the Fig 5.12 a $SNR/SNR(S/P=0)$ above one denotes that the SNR of the iodine has been improved compared to the absence of scatter. When it is below one the SNR of the iodine has been degraded. As can be seen, the scatter correction approach improves the SNR whereas the scatter removal does not provide any benefit in terms of iodine SNR. This is due to the properties of noise in the log transformed images that is inversely proportional to the detected signal. Thus, although in the scatter corrected images the scatter is present in the low-and high-energy beams thereby reducing the detected SNR, in the iodine selective image its effect is reversed.

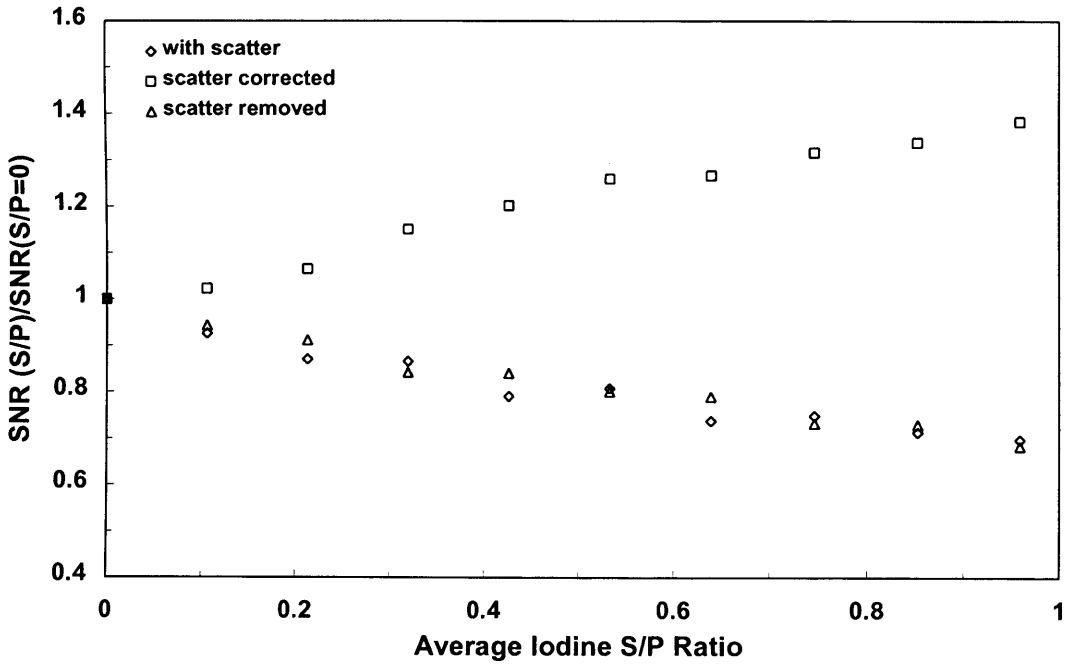

Figure 5.12. $SNR / SNR(S/P=0)$ of 3 mg/cm^2 in the presence of scatter when scatter has been removed and when scatter has been corrected, normalised to the SNR in the absence of scatter for different iodine S/P ratios.

As shown in Figure 5.11, both approaches result in an accurate estimation of the iodine projected thickness. However, the noise associated with the scatter radiation can not be removed and will be present in the image. Thus if the scatter removal approach is used it will provide accurate iodine projected thickness measurements but will not improve the SNR of iodine signal at lower thicknesses.

It is important to emphasise that the SNR degradation depends not on the scatter component, but rather on the scatter to primary ratio, and in a nonlinear and nonuniform manner (Fig. 5.12). In addition, even though the scatter in breast may be almost constant as a function of position (excluding the breast periphery) the degradations may vary sharply from one location to another due to large differences in primary radiation (Fig. 5.11).

The above discussion provides an important insight into the SNR properties of the dual energy imaging. However the fact that noisier images provide better SNR does not mean that the detectability of the iodine will be better. Figure 5.13 shows the same data as Figure 5.12 but now the CNR is considered as image quality metric. In this plot the $CNR / CNR(S/P=0)$ in the presence of scatter improves when compared with the absence of scatter. This indicates that the erroneous estimation of iodine and breast composition is less significant as compared to noise reduction in the iodinated area. This is one of the most important properties of material selective imaging, where not the isolation of material, but the noise in the isolated material imposes the fundamental limitations of this imaging approach. The $CNR / CNR(S/P=0)$ when the scatter is removed remains unaltered as compared with the $SNR / SNR(S/P=0)$ so the same observations hold true. Conversely, the $CNR / CNR(S/P=0)$ results have almost been reversed in the case of the scatter correction approach. This is because the scatter correction approach corrects for the errors in the estimation of iodine projected thickness but not the errors associated with the estimation of breast composition. Thus at high S/P ratios, the CNR in the iodine selective image will be reduced. This is because, the contrast of the iodine is limited by a positive offset related to errors in the breast

composition estimation. Thus the scatter correction restores the iodine projected thickness to its actual value but at the same time decreases the image contrast, possibly limiting this approach despite the superior iodine SNRs achieved.

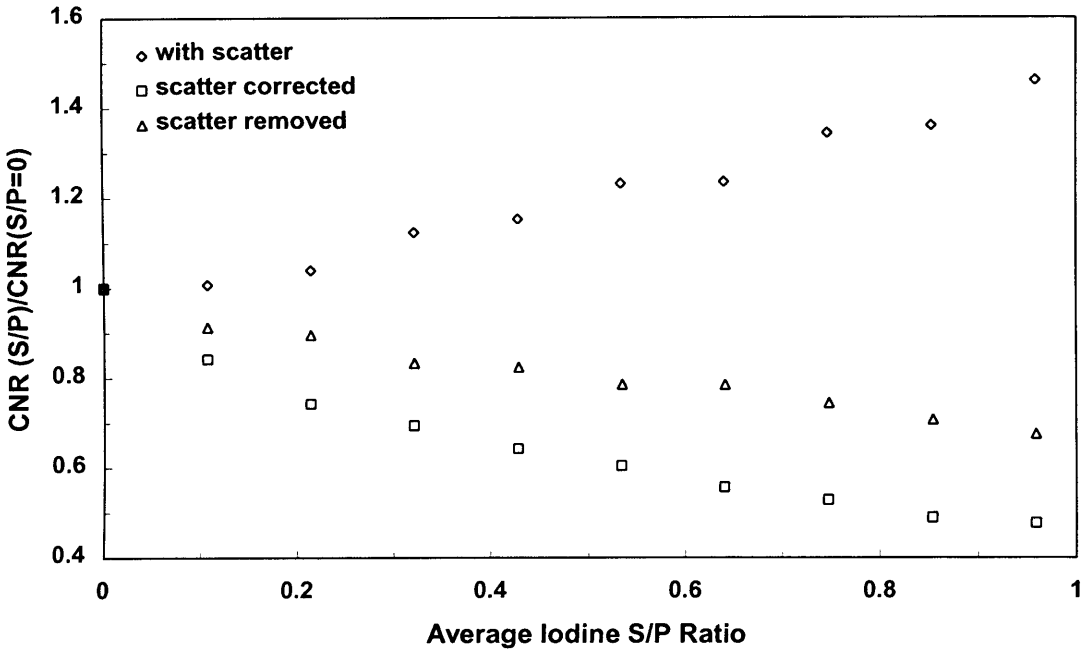

Figure 5.13. $CNR/CNR(S/P=0)$ of 3 mg/cm^2 in the presence of scatter when scatter has been removed and when scatter has been corrected normalised to the CNR in the absence of scatter for different iodine S/P ratios.

Finally, the last image quality descriptor is the SDNR. Figure 5.14 shows the $SDNR/SDNR(S/P=0)$ for the same data and combinations as in Figure 5.12. The $SDNR/SDNR(S/P=0)$ for the all the combinations examined shows the same degradation. This indicates that in material selective imaging in the presence of scatter there will always be some degradation in the image quality. This also suggests that if one tries to correct for the signal nonlinearities (scatter removal) the noise will become important. Conversely, if no measures are taken to correct for the scatter the image will be less noisy but signal nonlinearities will be present. If both noise and signal are improved (scatter correction) then the background signal offsets will appear in the material selective image.

It is interesting to note that the scatter removal approach was remarkably stable irrespective of image quality metric used and, although in all cases was below the ideal

response it showed the minimum degradation as compared to the scatter correction approach. Therefore, this approach can be selected as the most robust in tackling the detrimental effect of scatter radiation in material selective imaging. Last but not least, from the above discussion it is interesting to note that in the presence of scatter the SDNR provides a good and accurate descriptor of image quality in material selective imaging.

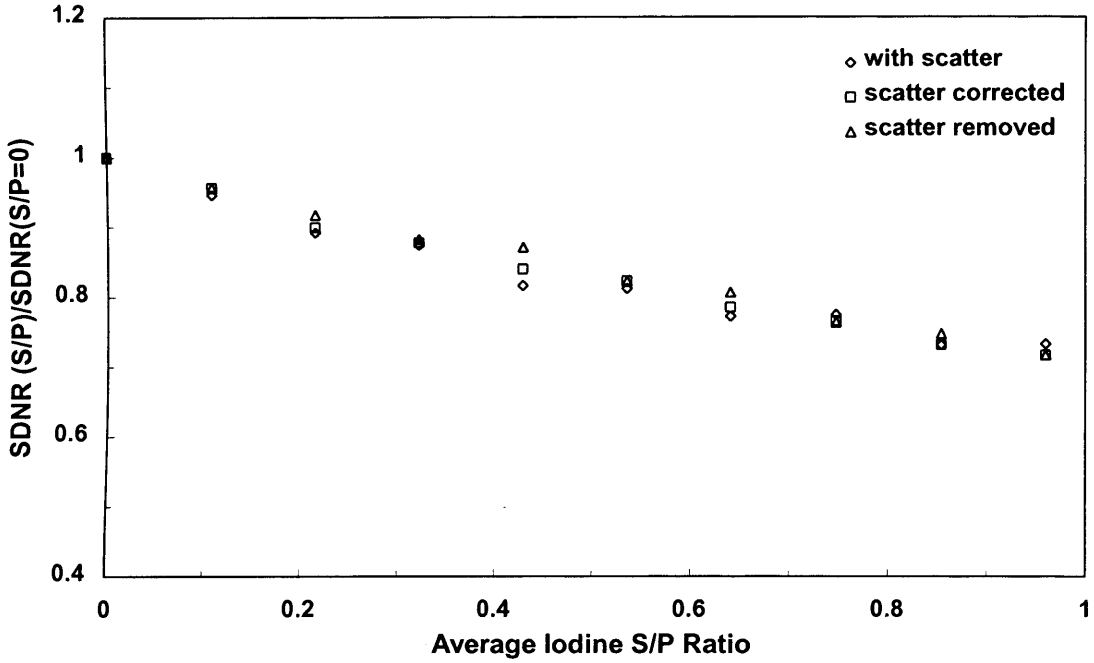

Figure 5.14. $SDNR/SDNR(S/P=0)$ of 3 mg/cm^2 in the presence of scatter when scatter has been removed and when scatter has been corrected normalised to the CNR in the absence of scatter for different iodine S/P ratios.

5.3.7. Simulated and experimental iodine selective images

Figure 5.15 shows the low-, the high-energy and the iodine selective images of the simulated and experimental breast equivalent phantoms. The iodine projected thickness was 3 mg/cm^2 apart from the Vanilla which was 8 mg/cm^2. The mean glandular dose with the of was ~0.1 mGy. The selection of so low total mean glandular dose was because the Vanilla sensor was very sensitive and could not accommodate exposures at signal values that deviations from linearity where not significant. To the left of each image is the adipose tissue equivalent plastic and to the right of each image is the glandular tissue equivalent plastic. As can be seen in the iodine selective image (Fig. 5.15(c)), the iodine signal is not affected by the ramp, which formed the background breast structure

incorporating all possible compositions of adipose and glandular tissue. In the experimental image there is some remnant fixed pattern noise (phosphor nonuniformities) that has not been corrected through flat fielding. This is because the effectiveness of flat fielding was limited due to the EMI noise observed in both detectors (Fig. 4.22). The nature of this noise component is non-stationary and alters the amplitude of the phosphor fixed pattern noise from frame to frame, limiting the effectiveness of flat field image averaging (Eq. 3.6). The contrast with the Vanilla detector (CsI) is lower than the contrast with the PaxScan 4030R flat panel (Gd_2O_2S). As shown above (Figs. 5.1 and 5.5), with the CsI phosphor the visibility of the iodine should be better than with the Gd_2O_2S. However, the fact that the sensor has much smaller pixel size results in lower SNR, as explained above (Fig. 5.8). In addition, Vanilla had higher EMI noise that did not allow effective suppression of the fixed pattern noise. Thus, in the iodine selective image this type of noise was even higher, limiting the visibility of the iodinated cylinder.

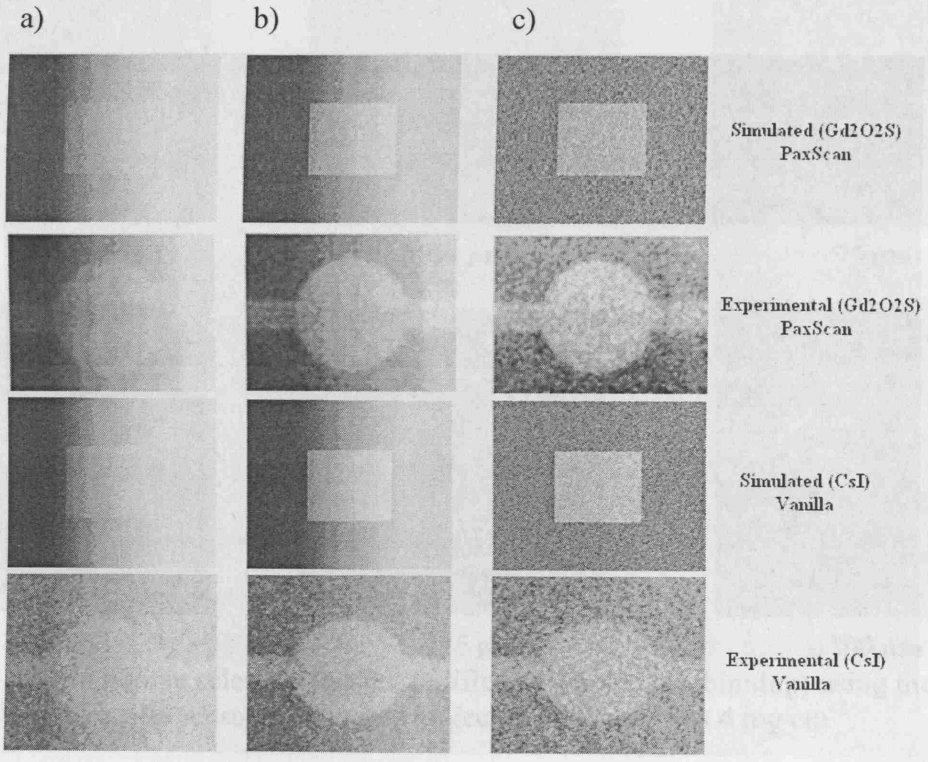

Figure 5.15. Dual energy images of the experimental and simulated phantom. In column a) and b) are the low and high energy images of iodinated solution and in c) are the structured noise suppressed images. The images in the odd rows are the simulated and in the even are the experimental for Gd_2O_2S:Tb and CsI:Tl based phosphors. For all the

images the iodine thickness was 3 mg cm^{-2} apart from the Vanilla which was 8 mg cm^{-2}. The thickness of the phantom was 4 cm and the total mean glandular dose was ~0.1 mGy.

Figure 5.16 shows the iodine selective images at different pixel sizes (binning) for the Vanilla sensor. In the data presented there was no measure taken to suppress the noise in the iodine selective image. It is shown that the visibility of the iodinated area is proportional to the pixel size. This is in agreement with the simulation presented above. In the section 5.3.9 (Fig. 5.20) a quantitative analysis of this dependency is presented. However, it is evident that the visibility of the iodine projected thickens is very low as compared to the PaxScan 4030R flat panel imager even at the same pixel size. This could be due to the inefficient flat fielding of low- and high-energy images acquired with the Vanilla.

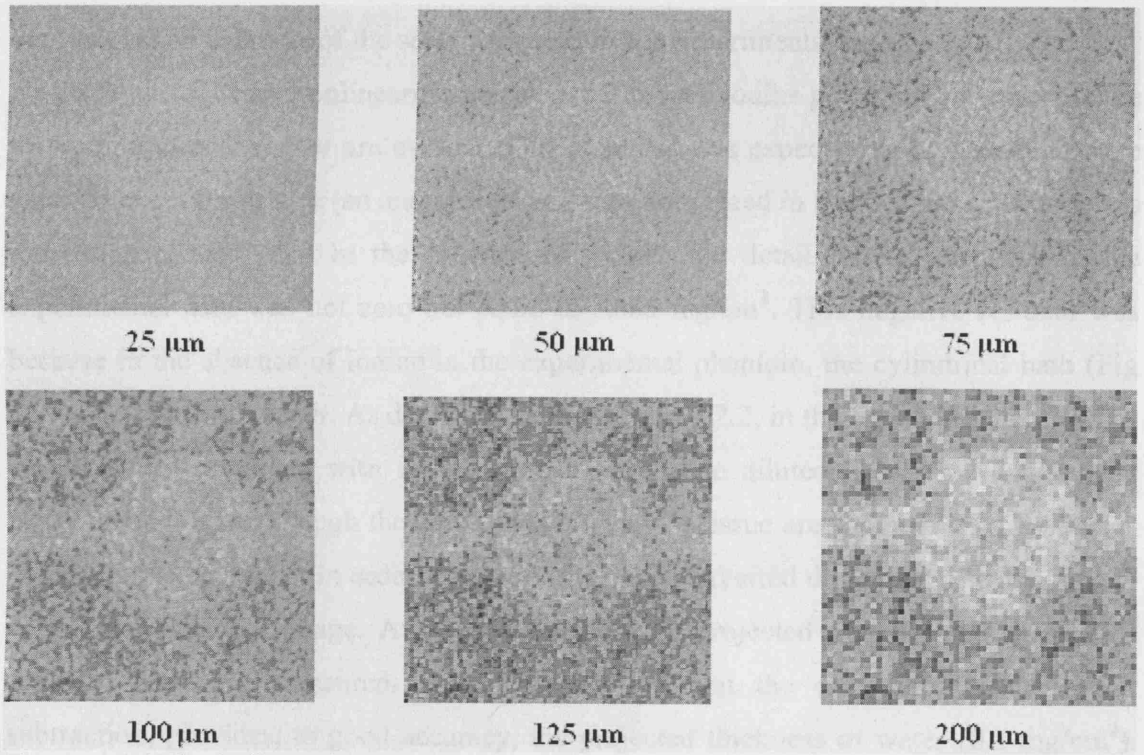

Figure 5.16 The iodine selective images at different pixel sizes (binning) using the vanilla sensor for the Vanilla sensor. The iodine projected thickness was 4 mg cm^{-2}.

5.3.8. Experimental iodine project thickness estimates with AMFPI

Figure 5.17 shows the measured iodine projected thicknesses using the PaxScan 4030R (Gd_2O_2S based) detector as a function of the actual iodine projected thickness. The same plot shows the simulated thickness with scatter, and also with scatter removed.

The simulated data are the same as in Fig 5.11 and from those data we estimated the scatter fraction (32% of the total detected signal) in the experimental images. The experimental iodine projected thicknesses after the scatter fraction has been removed are also shown in Figure 5.17.

The scatter fraction estimate in the experimental data was based on the assumption that in area (~3 cm) that surrounds the small iodinated (6 mm) cavity the spatial distribution of scatter was uniform. An additional reason for performing such correction is that both the simulated and the experimental phantom were "constructed" so as to have the same geometry. Thus the scatter fraction should be approximately the same in both. In particular, the scatter fraction in the simulated images was altered so as to achieve similar degradation in the nonlinearity with the experimental data. Thus, under the assumption of the uniform spatial distribution of the scatter, the simulated scatter fraction was used as an estimate of the scatter fraction in the experimental images.

In Figure 5.17 the nonlinearities in the experimental iodine projected thicknesses, due to the presence of scatter are evident. This response was expected as no measures were taken to reject the scatter (an anti-scatter grid was not placed in front of the detector). It is interesting to note that in the absence of iodine, the detail iodine thickness in the experimental data was not zero but equal to -0.65 mg/cm^2. This negative residual was because in the absence of iodine in the experimental phantom, the cylindrical bath (Fig 5.2) was filled with water. As described in the section 5.2.2, in the simulation the contrast medium was simulated with iodine and not as iodine diluted in water. Thus in the experimental data, although the adipose and glandular tissue are suppressed, the water is considered to be iodine. In order to quantify this, we converted the iodine selective image to a water selective image. After the conversion, a projected thickness equal to 0.13 mg/cm^2, has been measured. By taking into account the error due to the linear subtraction, provides, to good accuracy, the projected thickness of water (0.2 mg/cm^2). Thus this value has been removed from the data.

By removing the scatter fraction from the experimental images, the detail iodine thickness, within experimental precision, is restored to its actual value. It is interesting to note the remarkable agreement of S/P ratios estimates of the data presented with these by Boone et al (2000) using the same breast composition (50% glandular and 50 % adipose)

and thickness (4 cm thick). We feel that the main reason for this agreement is that both the field of view (FOV) and source to object distance (SOD) where similar with those used in the simulations. In addition, this signifies that of S/P ratios in breast are more affected by the breast thickness rather than the breast composition.

The effectiveness of the scatter removal in restoring the detail iodine projected thickness signifies the importance of simulation in the development of quantitative imaging. Thus, although scatter rejection will always be the gold standard in tackling scatter for the development of quantitative contrast enhanced mammography, estimation of the scatter fraction through simulation or modeling can provide a viable and dose affective alternative.

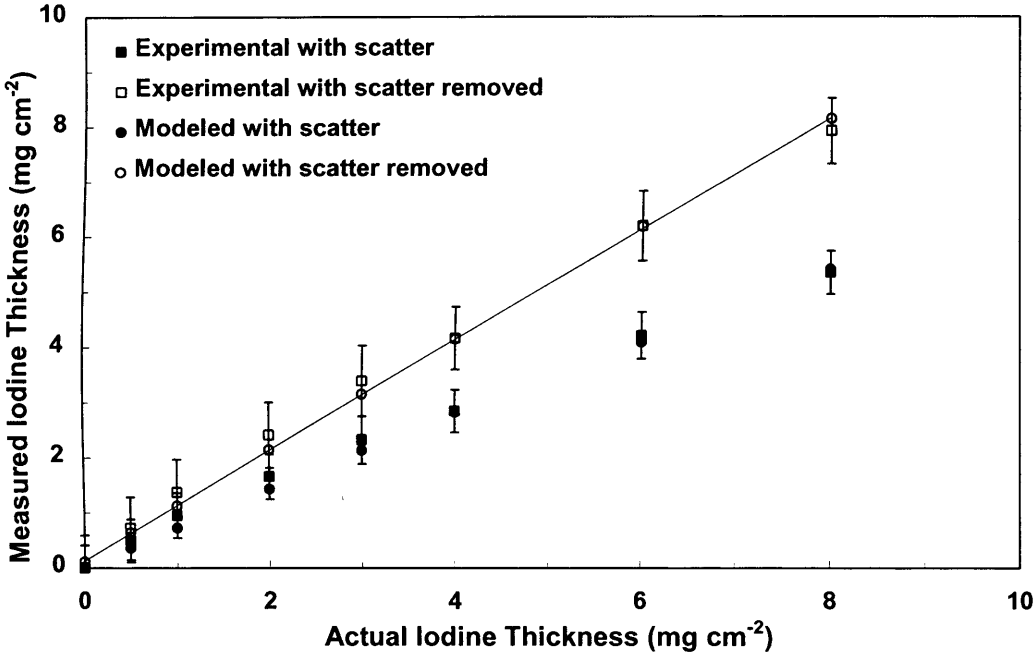

Figure 5.17. The experimental iodine thickness measured with the PaxScan 4030R detector. The measured thickness from the simulated phantom incorporating scatter radiation and the same data after the scatter fraction has been removed as a function of the actual iodine thickness is also shown The breast thickness was 4 cm and the total mean glandular was ~0.4 mGy.

5.3.9. Experimental iodine project thickness estimates with APFPI

Figure 5.18 shows the experimental iodine projected thicknesses using the Vanilla HR (150 μm) detector as a function of the actual iodine projected thickness. In the same plot is shown the simulated iodine projected with scatter removed. The simulated data

have been estimated after removing the same scatter fraction with the experimental data as above (Fig 5.17). As can be seen the removal was able to restore the detail iodine thickness, within experimental precision, to its actual value.

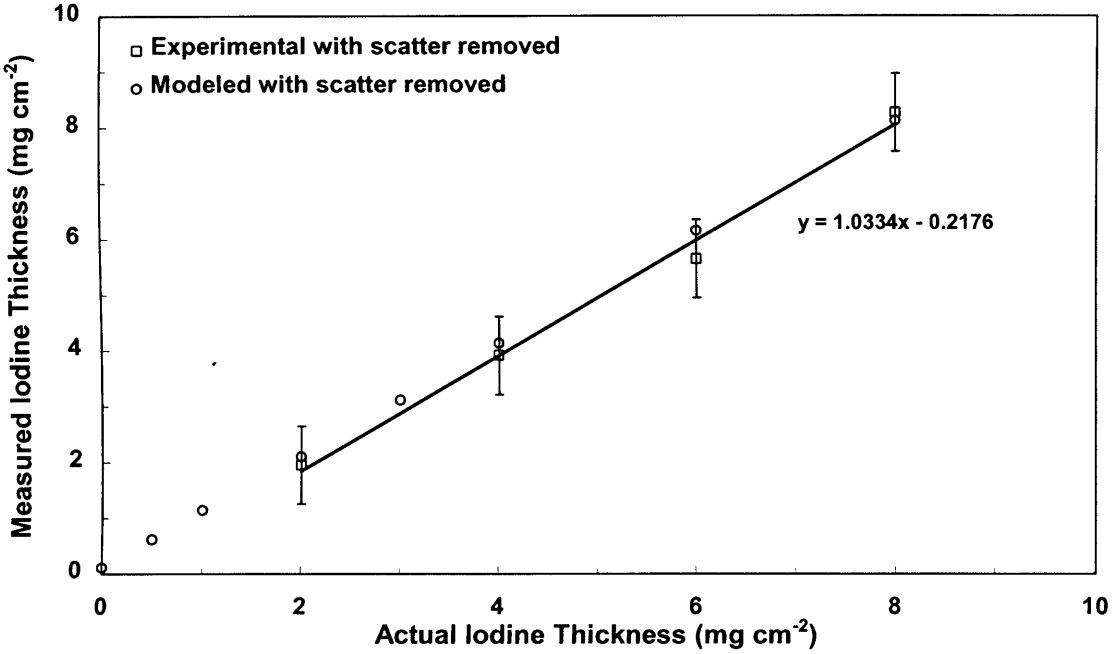

Figure 5.18. The experimental iodine thickness measured with the Vanilla HR (150 μm) detector. The measured thickness from the simulated phantom incorporating scatter radiation as a function of the actual iodine thickness is also shown. The breast thickness was 4 cm and the total mean glandular was ~0.1 mGy. The correlation coefficient with the linear regression was 0.99 and was performed for the experimental data.

Figure 5.19 shows the experimental SNR as a function of iodine projected thickness for the PaxScan and Vanilla sensor. The simulated SNR is also shown. The mean glandular dose for the PaxScan was equal to 0.1 mGy. Scatter radiation has been incorporated in the simulated data and corrected as explained above. The vanilla data have been binned in order to provide pixel size equal to 125 μm. The system gain of the simulation was the only parameter that was adjusted in order to achieve comparable SNRs between the experiment and the simulation. For the PaxScan detector was set equal to 0.38 electrons per keV deposited on the sensor (electrons/keV) and for the vanilla was 0.2 electrons/keV. This results approximately to 11 electrons per X-ray photon with 30 keV energy for the PaxScan sensor and 6 electrons for the Vanilla sensor. The system gain for the PaxScan sensor is reasonable and as can be seen from Fig. 5.19 the simulated

and experimental data have similar trends. The differences at higher iodine projected thicknesses are possibly due to the higher contribution of the detector fixed pattern noise. In addition iodine projected thickness lower than 3 mg/cm^2 can be effectively detected (SNR>5).

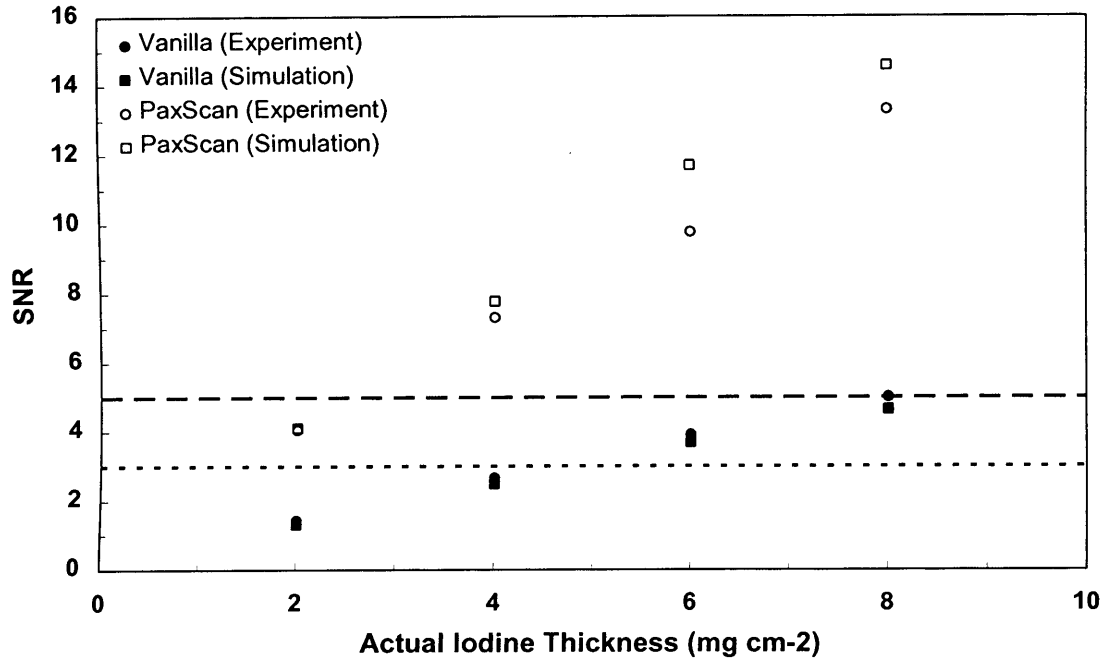

Figure 5.19. The experimental SNR as a function of iodine projected thickness for the PaxScan and Vanilla sensor. The simulated SNRs are also shown. The breast thickness was 4 cm and the total mean glandular was 0.1 mGy. The Vanilla data have been binned in order to provide pixel size equal to 125 μm.

However, for the Vanilla sensor the system gain and the resulted SNRs are much smaller than it was expected. The difference between the simulated results and the experimental for the Vanilla sensor might be due the high remnant fixed pattern. The effectiveness of the flat fielding was limited because the sensor used had high EMI noise (Fig. 423(a)). We have to note that this noise component can be effectively removed if the EMI noise is eliminated. Thus, although the performance of the Vanilla sensor in terms of sensitivity is superior, as compared with currently available digital X-ray detectors (see next Chapter), the incomplete FPN removal limits its applicability to quantitative contrast enhanced mammography. In addition this plot demonstrates the characteristics of dual energy imaging where noise components which are negligible in

conventional mammography can be 'magnified' in dual energy imaging. This is due to the logarithmic transformation and the consequent subtraction that adds the noise variances from the two images in the way that described in Chapter 1 (section 1.2.4). Therefore, for material selective imaging, beyond the quantum noise, all the noise components in the low- and high-energy images should be effectively suppressed, otherwise excessive noise will appear in the final image.

Figure 5.20 shows the detail SDNR as a function of pixel size for the Vanilla sensor. The iodine projected thickness was 4 mg/cm^2. The pixel has been binned in similar way that used for the empirical performance evaluation in section 4.3.2.5. As can be seen, the SNR increases linearly with the pixel size. This is in agreement with the simulated data presented in Figure 5.8. A comparison of the slope and the amplitude between simulation and theoretical estimates is not reasonable due to the high fixed pattern of the Vanilla sensor. As it was explained above this noise component was not included in the simulation.

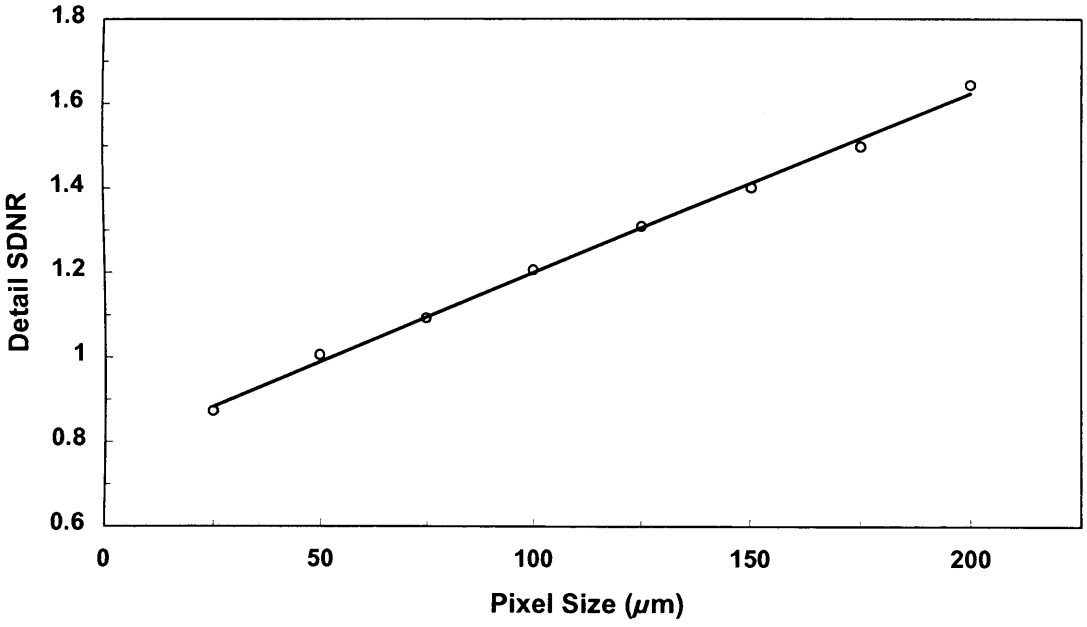

Figure 5.20. The experimental SDNR as a function of pixel size for the Vanilla sensor. The iodine projected thickness was 4 mg/cm^2. The breast thickness was 4 cm and the total mean glandular was ~0.1 mGy.

5.3.10. Contrast medium kinetics measurements

The contrast medium kinetics measurement based on the experimental phantom is presented in Figures 5.21 and 5.22 for the two different circulation configurations using the PaxSan detector. It is evident that temporal differences in iodine concentration can be effectively detected. The open circulation (Fig 5.21) was used for contrast media up-take measurement, as the flow rate could be measured with high accuracy through volume sampling. The closed circulation (Fig 5.22) was used to measure the maximum iodine projected thickness, as the amount of the circulated water and the injected contrast media could measured with high accuracy. Although the closed circulation could be also used for up-take measurement it was not possible to confirm that the flow rate was constant. The only corrections that were applied to the data were the water offset and the scatter removal. It is important to note that the calibration data were only used for the scatter fraction estimates and not for the iodine projected thickness measurements shown in the kinetics plots. The data without scatter removal are also shown in the plots.

As can be seen in Figure 5.21, the very sharp increase and decrease of the iodinated signal maps the passage from the simulated tumour of the injected bolus of the contrast medium. Using the first passage the flow rate was measured to be 0.27 ml/sec that resulted in only ~20% error as compared with actual flow rate (0.33 ml/sec). It is interesting to note that without the scatter correction the error in the flow rate measurement is as high as ~45%. This indicates the importance of the scatter correction in measuring the contrast medium kinetics. The same holds for the maximum enhancement measurement that was underestimated by 33%.

It is important to note that the enhanced signal recorded from the dual energy imaging will be affected by the thickness of the iodinated area or tumour size as well as from iodine present in the beam path but not in the tumour. Thus, if the thickness of this area is large then the enhanced signal will not be directly proportional to neovascularisation and will be inflated from the underlying up-take of iodine. In order to correct for this a dual energy Tomosynthesis has been recently proposed (Carton A-K *et al* 2007). However, the incorporation of Tomosynthesis automatically limits the examination to static imaging (maximum enhancement) as the dose level will be considerably higher than the conventional mammography if kinetics information is needed. We feel that this problem

can be addressed by simply acquiring an image pair at 90 degrees with respect to image pairs used for the kinetics measurements. This will provide adequate information regarding the underlying iodinate areas and tumour actual thickness while the dose will be kept at very low levels (~0.4 mGy).

Adopting this approach blood flow per unit volume of tissue measurements can be performed and direct link of the enhanced areas with the tumour microvessel density and perfrusion can be established. The units of blood flow using this approach can be reported as millilitre of blood per minute per millilitre of tissue (ml min^{-1} ml^{-1}). From the Figure 5.21 the units are expressed in $mg \times cm^{-2} \times sec^{-1}$. Using the thickness of the iodinated cylinder and the iodine density yields 1.7×10^3 ml min^{-1} ml^{-1}, millilitre of water per minute per millilitre of tissue assuming that the tissue density is ~1 mg/cm^3.

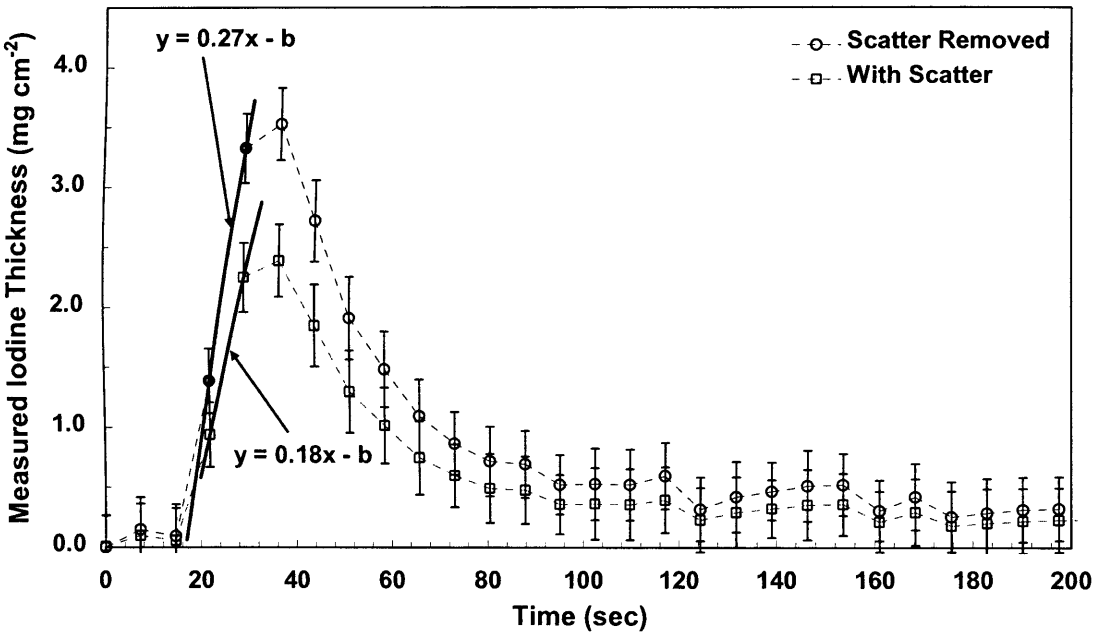

Figure 5.21. Open circulation contrast medium kinetics measurements based on experimental phantom (4 cm thick) using the PaxScan 4030R detector. Approximately one image every 7 seconds was acquired.

In addition, the high correlation between microvessel density and uptake of perfusion radiotracer technetium 99m methoxyisobutyl isonitrile demonstrated that breast tumour microvessel density is associated with an increase in blood flow or perfusion (Omar W S *et al* 1997). Similar correlations have been reported using iodinated contrast media (Jong

R A *et al* 2003, Lewin J M *et al* 2003, and Dromain C *et al* 2007). It is important to note that the first pass of the contrast media from the tumour is of interest. Although, the required temporal resolution has not been determined yet it is evident that X-ray contrast enhanced mammography can provide adequate temporal resolution with minimal compromise in the spatial resolution.

In the kinetics measurements using the close circulation (Fig. 5.22), without the scatter correction, the detail iodine projected thickness is also underestimated. However, after the scatter correction has been applied the expected maximum iodine projected thickness, as measured 10 minutes after the contrast medium administration, was 2.4 mg/cm^2. At that time the curve reaches a plateau indicating that the contrast media has been uniformly diluted with the circulated water. The maximum actual iodine projected thickness after uniform dilution is 2.6 mg/cm^2. Thus, the maximum measured iodine projected thickness value corresponds to the maximum actual iodine projected thickness. Furthermore, 4 to 5 data points can provide adequate information regarding the contrast media kinetics. This is particularly relevant to clinical conditions where 5 image pairs will provide total mean glandular dose less than 1.8 mGy that is equivalent to doses found in conventional digital mammography.

In neither of the kinetics plots has other correction been applied, nor has the calibration data been used to convert the pixel values to iodine projected thickness. Considering this, these plots clearly demonstrate that quantitative contrast enhanced measurements using the dual energy approach can be performed. In addition, these plots demonstrate that if scatter corrections are applied, unbiased attenuation measurements from the detector can be performed and absolute enhancement measurements can be provided, independent of calibration data at any point in the time domain without the need of an image mask.

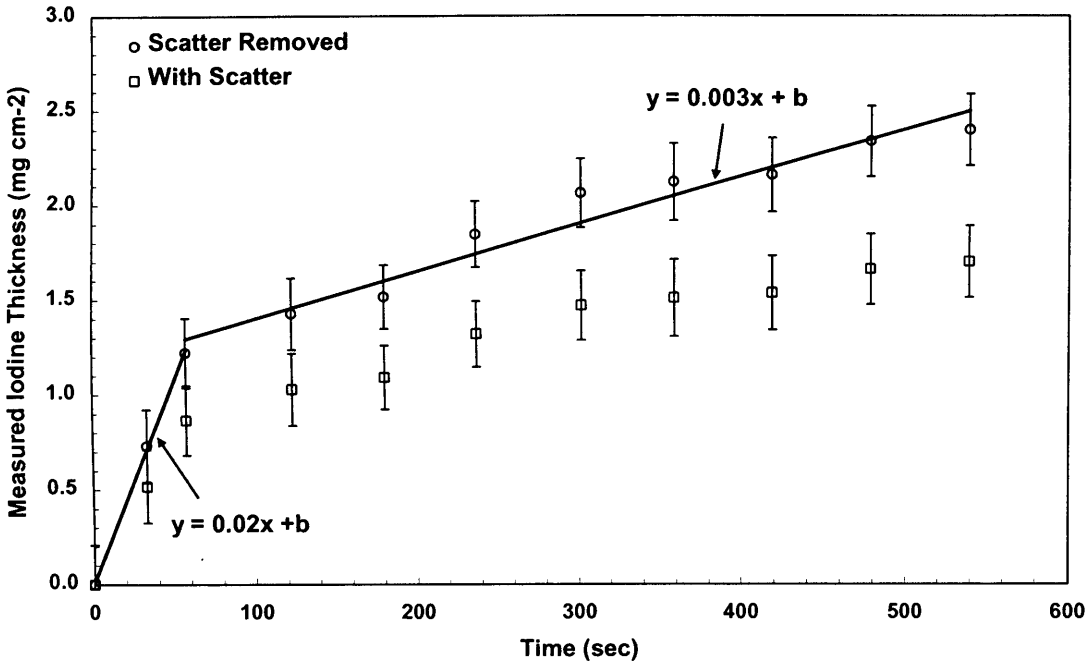

Figure 5.22. Close circulation contrast medium kinetics measurements based on experimental phantom (4 cm thick) using the PaxScan 4030R detector. Approximately one image every 60 seconds was acquired.

5.4. Summary

This Chapter explored the experimental and theoretical analysis of quantitative contrast enhanced mammography. Optimisation of critical performance parameters was presented. The minimum detectable iodine projected thickness for different breast thicknesses has been estimated using the iodine SNR and SDNR. The measured iodine image signal and the actual iodine projected thickness scale linearly, irrespective of breast composition, breast thickness, energy fluence and detector. The effect of beam hardening was insignificant in the iodine projected thicknesses relevant to those found in clinical conditions. Strong deviations from linear response appeared to be due to the presence of scattered radiation. However if the scatter fraction in the image is removed before any post-processing of the images the detail iodine thickness measurements are restored to their actual value. When the Vanilla sensor was employed the SNRs obtained were unreasonably low for the iodine projected thicknesses studied. For the PaxScan detector a reasonable correlation between the experimental and simulated data has been achieved. Using this detector SNR higher than 5 has been obtained for iodine projected equal to 3 mg/cm^2. Finally, the results suggest that contrast medium kinetics

measurements can be performed and the up-take and wash out of contrast media can be measured. The results suggest that the development of quantitative contrast enhanced mammography based on quantitative spatio-temporal iodine selective imaging can be performed.

Chapter 6

System Integration and Consideration of its Clinical Potential

6.1. Overview

This chapter is divided into three sections. In the first, we discus the potential benefits and current limitations of APFPI for digital mammography (conventional and quantitative contrast enhanced). Comparison of the physical performance with currently available digital detectors is presented. In the second, we discuss development of quantitative contrast enhanced mammography along with the system integration and the clinical potential of the system developed. Finally, the third section provides the conclusion and the future work.

6.2. Active pixel flat panel imager -APFPI- for digital mammography

The empirical electro-optical and X-ray performance evaluation of the developed active pixel flat panel imagers has been performed, offering unique insight to the detectors' performance. The methods presented can help to analyze the properties of digital sensors and lead to optimised performance by achieving shot limited response.

The sensors presented offer very high fill factor and good interacting quantum efficiency. In the 3T APS, incorporation of 4 nwell photodiodes in the pixel provides high charge collection efficiency with almost uniform round distribution, and low pixel cross talk. Low noise (114 electrons), high full well capacity (10^5 electrons), good interacting quantum efficiency (33% at 540 nm), high signal-to-noise ratio and dynamic range are some of the key benefits of this sensor, that also offer good spectral matching with CsI:Tl scintillators. The nonlinearity observed is an inherent characteristic of CMOS APS and is observed at high signal levels. This property of this sensor can be very important for medical imaging as a linear response of the detector does not suppress the contrast of high or low intensity (or pixel values) areas as opposed to screen film mammography.

The Vanilla sensor, offered a way to compensate for the high kTC noise, through 'flush' reset. However, the observed superlinearity, limited the use of this property. In practice this sensor was operated under standard 'hard' reset. The benefit of this sensor is its very high interacting quantum efficiency (63% at 540 nm) as a result of an optimised CMOS process. One PD was incorporated per pixel, thus the linear range of the sensor was limited to $\sim 2\times10^4$ electrons, almost 4 times lower than the 3T APS. However, as a result, the optimized process used and the one PD per pixel lead to a reduction in the leakage current of more than one order of magnitude. The nonlinearity observed needs to be corrected before any processing of the images.

Detector performance for mammography and other radiographic applications is widely measured using observer-independent performance variables (MTF, NPS and DQE). However, as the tube anode, beam energies and filtration are not identical among the measurements performed from different researchers care should be taken when comparing different systems. These differences may be less critical when MTF is considered as the energy range investigated for detectors in digital mammography usually is below the CsI k-edges, however the comparison of DQE curves should be performed more carefully.

The two CMOS APS, were coupled with structured CsI, providing a high performance indirect X-ray detector, i.e., an active pixel flat panel imager (APFPI). At detector entrance exposure levels up to 10 μC/kg the sensor was demonstrated to be linear. The low total additive electronic noise and the high full well of the sensor presented offer an X-ray detector with wide dynamic range that can accommodate up to 25.8 μC/kg detector exposures beneath the breast. The vanilla system configurations due to their high sensitivity could accommodate from 2.0 μC/kg to 3.5 μC/kg detector exposures. Although it is desirable to have detector with high sensitivity the results demonstrate that X-ray imagers with very high sensitivity their application to conventional mammography is limited from their dynamic range. Nevertheless X-ray imagers with so high sensitivity can be extremely useful to low dose imaging such as advanced mammographic techniques and fluoroscopy. In addition, the Vanilla sensor was sensitive to compression thus the resolution of these system configurations was limited from the relatively poor coupling efficiency. In the following discussion a thorough

comparison of the 3T APS system configurations with X-ray imagers based on other detector technologies will be presented as this sensor full fills most of the detector requirements for digital mammography.

High resolution has been achieved for the 3T APS system configurations employed in this study and compared favourably with a:Si AMFPI that currently exist in clinical practice (Vedantham S *et al* 2000). Although at 50 μm pitch the system resolution of the 3T APS did not alter significantly, the better performance of the sensor compared to the a:Si based imager (Vedantham S *et al* 2000) (100 μm pixel pitch) could be attributed to the smaller pixel size employed. It should be noted that for indirect X-ray detectors the system MTF apart from the aperture and scintillator MTF is affected by the "optical" MTF that describes the degradation of system's MTF due to the imperfect coupling of the scintillator with the sensor (Jee K-W *et al* 2003). This type of degradation is a concern in indirect detection imagers and if not minimised can have a significant contribution to the system's MTF especially at higher frequencies. The system configuration with 95 μm CsI has comparable resolution with numerous proposed detectors for indirect detection (El-Mohri Y *et al* 2006 and Jee K-W *et al* 2003, Williams M B *et al* 1999 and Suryanarayanan S *at al* 2005). The system MTF of these detectors that were either based on a:Si AMFPIs (El-Mohri Y *et al* 2006 and Jee K-W *et al* 2003) or on CCD based imagers (Williams M B *et al* 1999 and Suryanarayanan S *at al* 2005) was 10% at ~10 cycles/mm when high resolution CsI or Gd_2O_2S was employed.

The DQE of X-ray imagers in other studies was measured using Mo/Mo spectra and beam filtration similar to our study (~4 cm PMMA), however, the tube kVp was slightly lower (26-28 kVp) than the one employed here. The variations in DQE due to small spectra differences are expected to be marginal (Suryanarayanan S *at al* 2005). Therefore a comparison of the systems DQE can be performed. At exposure levels of 0.44 μC/kg (1.72 mR) the DQE approaches quantum limited response in both 3T APS system configurations, and compared favourably with other detector technologies. In particular the DQE of the presented detector was found to be higher than the DQE of a:Si AMFPI that currently exist in clinical practice (Vedantham S *et al* 2000) measured at ~0.34 μC/kg (~1.3 mR) and similar at higher exposures ~8.55 μC/kg (~33 mR). However at high frequencies the detector presented here has higher DQE, mainly due to smaller pixel

size employed. The DQE of another a:Si AMFPIs system coupled to high resolution (HR) and high light (HL) output CsI has been investigated by Jee et al 2003 . Both system configurations at similar exposures with our study had lower DQE than our current system. At an exposure of ~9.3 μC/kg (~36 mR) when the HR configuration was employed the DQE was similar, whereas their HL configuration appeared to have higher DQE than our current system. However the HL system configuration had lower MTF. The DQE at 0.26 μC/kg (1 mR) detector entrance exposure of a recently proposed high fill factor a:Si AMFPI by El-Mohri et al 2006 was lower than our current system when HR CsI was employed, and similar when HL CsI was employed. Both system configurations approach quantum limited response at exposures higher than 2.2 μC/kg (~8.5 mR) and appeared to have higher DQE than our current system at low frequencies. At high frequencies and at exposures below 2.2 μC/kg (~8.5 mR) our current system had better DQE. In addition, the total additive electronic noise (1200-2200 electrons) of this a:Si based detector is more than an order of magnitude higher than our current system. This noise level could reduce the SNRs at denser areas of the breast especially if the HR configuration is employed.

As compared with a:Se based imagers that exist in clinical practice the detector presented here has lower MTF but better DQE at 0.62 μC/kg (~2.4 mR) (Marshall N W 2006). At higher exposures, the a:Se based imager had slightly higher DQE at low frequencies (~0.6). Similar results have been obtained with other a:Se based imagers (Saunders R S *et al* 2005). At low exposures the DQE of AMFPIs is diminished by the high total additive electronic noise (~1000 electrons). Conversely the good performance at low exposures of the CMOS based detector presented is both due to its low total additive electronic noise and its high sensitivity. Despite the small contribution of the electronic noise on the DQE of the 3T APS configurations presented, a broader range of exposures would be more appropriate to show the response of the sensor.

The DQE of the detector was also better than, or comparable to, CCD based imagers. A CCD based detector proposed by Williams et al 1999 that was coupled to Gd_2O_2S scinitllator had lower DQE irrespective of exposure as compared with the sensor presented here. This was mainly due to the low system gain (~3 electrons/incident X-ray) of that imager. A recently proposed high resolution CCD based imager that was coupled

to CsI scintillator (Suryanarayanan S *at al* 2005), under quantum limited conditions it appeared to have similar DQE response with our current system over all frequencies. However it is interesting to note that for X-ray imaging, CCDs are susceptible to radiation damage (Janesick J *et al* 2001). Additionally, CCDs are serial devices, this means that all the charge has to pass from the same sense node before read out. For large area formats this limits the frame rate of the sensor since for higher readout speeds, the noise in CCDs becomes unacceptably high (Janesick J *et al* 2003). This limitation causes a bottleneck in large area CCD detectors, possibly restricting these devices to integration times higher than 2 sec or to static imaging in order to maintain low read out noise. On the other hand in CMOS APS massive parallel readout means that high frame rates can be used with minimal effect on the system performance. We should note that is desirable to see more research and development in this area in order to fully explore the benefits of the CMOS sensors as compared to CCDs for X-ray medical imaging.

Although the detectors were studied in the mammographic energy range, it demonstrates their low noise performance as compared to AMFPIs, so they could also be used for fluoroscopy. It has been shown that under fluoroscopic conditions, only a detector with very small additive electronic noise or very high on-pixel gain can be used for efficient detection, irrespective of the converter material used (Antonuk L E *et al* 2000 and El-Mohri Y *et al* 2006). Present generation direct and indirect AMFPIs have electronic noise as high as 10^3 electrons r.m.s. which is further increased at high frame rates. Another reason why CMOS APS could be suitable for fluoroscopic applications, that it has minimal image lag. In AMFPIs, especially under fluoroscopic mode, the charge carryover, visually perceived as image lag, is becoming very significant (Siewerdsen J H *et al* 1997), although in recent years significant progress has been made (Bloomquist A K *et al* 2006). In CMOS APS, image lag is observed when the reset bias is not high enough to effectively reset the sensor, however under appropriate biasing, image lag can be eliminated.

The sensors presented offer high resolution and an order of magnitude lower read noise as compared to AMFPIs. Response comparable with new detector designs has been achieved. The results suggest that CMOS detector technology is worth a further

investigation and that it can be used to conventional, advanced and fluoroscopic imaging tasks.

6.3. Quantitative contrast enhanced mammography

Optimization of critical parameters for the development of quantitative contrast enhanced mammography based on the dual energy approach has been presented. These include: (i) effective isolation of iodinated contrast medium from breast clutter background (ii) optimization of the energy pair (iii) assessment of low to high energy beam photon flux ratio, (iv) vascular contrast medium kinetics measurements, (v) restriction of total mean glandular dose from the series of images to the equivalent of conventional mammography (vi) measurement of iodine projected thickness and (vii) evaluation of the effect of beam hardening and scatter radiation.

It was shown that using the dual energy approach, measurement of the iodine projected thickness can be achieved irrespective of breast thickness or composition using polychromatic beams. The polyenergetic beams were provided by a commercially available Tungsten tube and shaped using materials (contrast medium and Cu) readily available in hospitals. For the measurement of the vascular contrast agent up-take a total of 4-5 image pairs should provide adequate information about the contrast medium kinetics within the breast tumour. A mean glandular dose of 0.2-0.4 mGy per image pair could provide kinetics information without exceeding mean glandular doses found in conventional mammography (Chevalier M *et al* 2004). At that exposure SNRs higher than 5 was achieved for iodine projected thicknesses less than 3 m/cm^2. Iodine selective images expressed in mg/cm^2 providing information about the iodine projected thickness have been produced, providing the means to develop quantitative contrast enhanced measurements. This is a very important requirement for intradepartmental comparisons of the examinations between hospitals. In addition, it will help to extract enhancement thresholds and investigate its relevance to the tumour formation.

The effect of beam hardening introduces nonlinearities into the final measurement of iodine. However these appear to only have a significant contribution at iodine thicknesses that are irrelevant to those found in clinical conditions or at iodine thicknesses that are representative of tumours of large size. The presence of scattered radiation is the only

factor that seriously degrades the measurement of the iodine projected thickness. It should be removed effectively before any analysis of the energy pair images. From the discussion in the previous chapter it is apparent that for the development of quantitative contrast enhanced mammography, it is essential to develop methods to eliminate the nonlinearities in the iodine projected thickness in the presence of scatter.

Elimination of scatter can be achieved in two ways; either by employing aggressive methods to reject scatter, or by simulations to estimate S/P ratios for a given breast thickness and composition. The first approach can be achieved using either anti-scatter grids with high bucky factors or using scanning systems. The use of an anti-scatter grid will result in a substantial increase in the mean glandular dose, possibly limiting the temporal resolution, and scanning systems are potentially susceptible to patient motion artifacts. Thus, simulation methods are the method of choice to correct the data and this can be done with adequate accuracy.

Plots of contrast medium kinetics, expressed in physical units, have been provided here. These plots demonstrate that if scatter corrections are applied, quantitative contrast enhanced measurements can be provided independent of calibration data at any point in the time domain, without the need of an image mask. Changes in the rate of enhancement can be effectively performed making it possible to measure the up-take and wash out of the iodinated vascular contrast agent. In addition, using the dual energy approach means the elimination of a mask image and makes the beginning of image acquisition for the assessment of the vascular contrast agent up-take less restricted. Enhanced measurements can be made at any point during the examination.

However, for the determination of the vascular contrast agent up-take at least one measurement before the maximum enhancement has been reached must be acquired. The visibility of the iodinated areas for accurate spatio-temporal iodine selective imaging can be further improved using either high gain detectors or off chip pixel binning or combination of both. Quantitative contrast enhanced mammography is limited neither from a medical nor from a physical point of view; however it is important to note that when performing blood flow or perfusion measurements one should take into account physical and physiological parameters related with patient undergoing the clinical

examination (haematocrit, weight etc). For perfusion measurements possibly the use of pick aortic enhancement might be needed.

Both breast MR imaging and digital X-ray mammography using temporal subtraction can isolate the contrast enhanced signal. However patient motion artifacts, especially using X-ray imaging where breast compression is inevitable, introduces additional motion artifacts, and limits the effective isolation of the iodinated region of the breast. If the breast compression is not released after each acquisition it is likely that the vascular contrast media cannot flow in the breast. Conversely, using the iodine-only images provided by the dual energy approach, even in the presence of patient motion artifacts during the examination, would make it much easier to register these images as the iodinated areas will provide an additional registration marker. This will provide a map of the vascular contrast media up-take on a pixel-by-pixel basis.

The systematic analysis and optimisation of quantitative contrast enhanced measurements in the breast facilitated by contrast agents may help with (i) an improvement of tumour detection in dense breasts, (ii) tissue characterisation, (iii) a reduction of false biopsies, (iv) clearer delineation of tumours, and (v) chemotherapy up-take.

Comparison with the findings presented from breast MR studies will reveal the clinical potential of the quantitative contrast enhanced mammography. I feel that both modalities will co-exist in future clinical practice and will be used where it is essential. With MR possibly having a small advantage in the "high-risk" young female population due to dose constraints, and quantitative contrast enhanced mammography to tissue characterisation due to its wide spread availability.

6.4. Conclusion and future work

Empirical electro-optical and X-ray evaluation of CMOS active pixel sensors has been performed. The sensor demonstrated the very good electro-optical properties currently available from this technology. The CMOS APS, when coupled with structured CsI, can yield a high performance indirect X-ray detector. These sensors offer high resolution and an order of magnitude lower read noise compared to AMFPIs. Response better or comparable with new detector designs has been achieved.

Based on the work presented some design characteristics and possible improvements could be suggested. The results demonstrate that the performance of the sensor does not alter significantly between 25 μm and 50 μm pixel pitch and therefore suggests that future CMOS APS developed specifically for conventional mammography could function at 50 μm pitch. In addition, improvement of the current system's performance could be obtained at larger (50 μm) pixel sizes (i.e. larger pixel active area) and by eliminating of the second fibre optic plate (i.e. better coupling efficiency). The larger pixel size along with ADC with resolution greater than 10 bits will increase the dynamic range of the sensor to accommodate higher raw exposures. The maximum skin entrance exposures found in digital mammography are approximately 750 μC/kg (~3.0 R) (Chevalier M. et al 2004). By taking into account the use of antiscatter grid and breast thickness this will result in approximately 256 μC/kg (~1.0 R) raw exposures. This would require a CMOS APS with $\sim 10^6$ electrons full well at similar system gain with our current system. This full well is more than feasible at 50 μm pixel size. The sensor nonlinearity appears only at high exposure levels and it might be beneficial as it extends the sensor dynamic range. Lower noise can be obtained with an optimized design, for example by using noise reduction techniques and can further improve the performance of the sensor at lower exposures. Additionally, a recent feasibility study performed on an eight inch wafer showed minimal degradation in the overall performance of the sensor. Tiling only four 10cm x 12cm detectors can provide an active area suitable for mammography (20cm x 24 cm). Such tiling of four detectors is a concern and would need to be carefully addressed.

An interesting future development in the CMOS APS will be the ability to bin pixels on chip; this will give the flexibility to use multiple resolutions and the required reduction in data transfer and storage for imaging applications where multiple images are required (Niklason L T *et al* 1997, Wu T *et al* 2003, Boone J M *et al* 2001, and Chen B and Ning R 2002). Although, it does not seem to be very difficult to address the problems associated with grounding (high EMI noise) and DAQ read out, these problems need careful consideration. The extent to which CMOS APS will be adopted for medical imaging tasks depends on many factors. In this study we performed a thorough performance evaluation of this detector technology and presented its potential benefits for digital mammography.

The theoretical and experimental analysis of the dual energy approach with application to contrast enhanced mammography has been performed. The results suggest that quantitative contrast enhanced mammography based on the dual energy approach can extract quantitative and temporal information from the enhanced tumour in order to indirectly measure the tumour microvessel density and blood flow.

Development of subtraction techniques using nonlinear functions to investigate whether the residual signal can be further suppressed should be examined. Improved experimental phantoms incorporating more complex structures and pulsutile flow could help to further support the data presented under more realistic conditions. Methods to correct for phosphor and X-ray field nonuniformities should also be examined. In addition, different materials to filter the low- and high-energy beams should also be investigated in order to further increase the iodine SDNR. Mammography units should also be equipped with dual target tubes that incorporate Tungsten target, as Tungsten target offer increased lifetime under heavy loads.

Ways to remove the scatter fraction from the low- and high-energy images are essential. Otherwise erroneous quantitative measurements will be performed. The scatter to primary ratio in mammography does not show a strong dependence with the breast composition. However, for high accuracy spatio-temporal imaging, Monte Carlo simulations should be further optimized, to provide accurate spatial information of scatter to primary ratios in the breast. Thus, along with contrast media isolation and kinetics measurements, accurate estimation of the breast composition on a pixel-by-pixel basis can be obtained. This will also provide breast density estimates. Clearly the composition of the breast will be biased from the scatter component in the initial low- and high-energy images however, we feel, that iterative approaches can be used to improve accuracy.

As Moore's law about the growth rate of the number of transistor fitting on a single integrated circuit holds true, computers will steadily increase in performance and the computational power will continue to increase. Thus, S/P ratio estimation techniques, possibly based on iterative methods, using Monte Carlo simulations, will become more efficient reducing the associated errors. The most viable alternative to deal with scatter radiation, is the use of scanning systems. These systems can provide the more effective scatter rejection (Jing Z *et al* 1998) leading to less noisy material selective (iodine or

glandular ratio) images, although they will increase the acquisition time and will be more susceptible to motion artefacts and tube loading. An interesting future development is to investigate whether tuned aperture Tomosynthesis can be used along with perfusion mammography in order to perform tissue volume measurements. The dose penalty could be possibly eliminated by the use of collimation to restrict the field only to the enhanced area. This approach is likely to be more effective when the enhanced areas are relatively small.

In conclusion, we feel the need to clarify that although the conditions under which the above measurements were made are similar to those found in real examinations, the findings of this study regarding either APFPI or quantitative contrast enhanced mammography can only be validated through clinical trials.

References

Alvarez R E and Mascovski A 1976 "Energy selective reconstructions in X-ray computerized tomography" Phys. Med. Biol. 21, 733-744

Antonuk L E, Jee K-W, El-Mohri Y, Maolinbay M, Nassif S. Rong X, Zhao Q, Siewerdsen J H, Street R A and Shah K S 2000 "Strategies to improve the signal and noise performance of active matrix, flat-panel imagers for diagnostic X-ray applications" Med. Phys. 27, 289-306

AST Ltd, 8 Roydonbury Industrial Estate, Harlow CM19 5BZ, UK. www.appscintech.com.

Aus R J, DeWerd L A, Pearson D W, Micka J A and Nag K H 1999 "Dependence of scatter on atomic number for x-rays from tungsten and molybdenum anodes in the mammographic energy range" Med Phys. 26, 1306-1311

Baldelli P, Bravin A. Di Maggio C. Gennaro G, Sarnelli A, Taibi A and Gambaccini M 2006 "Evaluation of the minimum detectable iodine concentration for contrast-enhanced subtraction mammography" Phys. Med. Biol. 51, 4233-4251

Barrett H H and Swindell W, 1981 *Radiological Imaging: The theory of image Formation, Detection and Processing*, Academic, New York

Berger M J, Hubell J H, Seltzer S M, Coursey J S and Zucker D S 1999 "XCOM: Photon cross section database". Technical report, NIST, http://physics.nist.gov/xcom.

Bernhardt P, Mertelmeier T and Hoheisel M 2006 "X-ray spectrum optimization of full field mammography: simulation and phantom study" Med. Phys. 33, 4337-4349

Birch R and Marshall M 1979 "Computation of bremsstrahlung X-ray spectra and comparison with spectra measured with Ge(Li)-detector" Phys. Med. Biol. 24, 505-517

Bliznakova K, Bliznakov Z, Bravou V, Kolitsi Z and Palikarakis N 2003 "A three dimensional breast software phantom for mammography simulation" Phys. Med. Biol. 48, 3699-3719

Bliznakova K, Kolitsi Z and Palikarakis N 2006 "Dual energy mammography: simulation studies" Phys. Med. Biol. 51, 4497-4515

Bloomquist A K, Yaffe M J, Mawdsley G E and Hunter D M 2006 "Lag and ghosting in a clinical flat-panel selenium digital mammography system" Med Phys 33, 2998-3005

Boets C, Barentsz J O, Mus R D, van der Sluis R F, van Erning L J, Hendriks J H, Holland R and Ruys S H 1994 "MR characterization of suspicius breast lesions with a gadolinium-enhanced TurboFLASH subtraction technique" Radiol. 193, 777-781

Bogaerts J, Dierickx B, Meynants G and Uwaerts D 2003 "Total Dose and Displacement Damage Effects in a Radiation-Hardened CMOS APS" IEEE. Trans. Elect. Dev. 50, 84-90

Boone J M 2002 "Normalized glandular dose (DgN) coefficients for arbitrary x-ray spectra in mammography: computer fit values of Monte Carlo derived data" Med. Phys. 29, 869-875

Boone J M, Lindfors K K, Cooper III V N and. Seibert J A 2000 "Scatter/primary in mammography: comprehensive results" Med. Phys. 27, 2408-2416

Boone J M, Nelson T R, Lindfors K K and Seibert J A 2001 "Dedicated breast CT: radiation dose damage and image quality evaluation" Radiology 221, 657-667

Boone J M, Shaber G S and Tecotzky M 1990 "Dual energy mammography: a detector analysis" Med. Phys. 17, 665-675

Brettle D S and Cowen A R 1994 "Dual energy digital mammography utilizing stimulated phosphor computed radiography" Phys. Med. Biol. 39, 1989-2004

Brody W R, Butt G, Hall A and Macovski A 1981 "A method for selective tissue and bone visulazation using dual energy scanned projection radiography" Med. Phys. 8, 353-357

Byng J W, Critten J P and Yaffe M J 1997 "Thickness-Equalization Processing for Mammographic Images" Radiology 203, 564-568,

Carton A-K, Lindman K, Ullberg C, Francke T and Maidment A D A 2007 "Dual-energy subtraction for contrast-enhanced digital tomosynthesis. Proc of SPIE 6510 6510071-11

Chakraborty D P and Barnes G T 1989 "An energy selective cassette for dual energy mammography" Med. Phys. 16, 7-13

Chang C H J, Nesbit E D, Fisher D R, Fritz S J, Dwyer S J, Templeton A W, Lin F and Jewel W R 1982 "Computed tomographic mammography using a conventional body scanner" AJR 138, 553-558

Chen B. and Ning R. "Cone-beam CT breast imaging: feasibility study" Med. Phys. **29**, 755-770 (2002)

Chevalier M, Moran P, Ten J I, Soto J M F, Cepeda T and Vano E 2004 "Patient dose in digital mammography" Med. Phys. 31, 2471-2479

Cunningham I A and Shaw R 1999 "Signal-to-noise optimization of medical imaging systems" J. Opt, Soc. Am. A 16, 621-632,

Cunningham I A 2000 ''Applied linear systems theory'' in Medical Imaging. Volume 1 Physics and Psychophysics, edited by J. Beutel, H. L. Kundel, and R. L. Van Metter (SPIE, Bellingham), pp. 79–159

Dierickx B, Meynants G and Scheffer D 1997 "Near 100% fill factor CMOS active pixels," in Proc. IEEE Workshop on CCD's and AIS's

Dobbins J T 1995 "Effects of undersampling on the proper interpretation of modulation transfer function, noise power spectra, and noise equivalent quanta of digital imaging" Med. Phys. Vol. 22, pp. 171-181

Dobbins J T, Ergun D L, Rutz L, Hinshaw D A, Blume H and Clark D C 1995 "DQE(f) of four generations of computed radiography acquisition devices" Med. Phys. 22,1581-1593

Dobbins J T, Samei E, Renger N T and Chen Y 2006 "Intercomparison of methods for image quality characterization. II. Noise power spectrum" Med. Phys. 33, 1466-1475

Doi K 2006 "Diagnostic imaging over the last 50 years: research and development in medical imaging science and technology" Phys. Med. Biol. 51, R5-R27

Dorenbos P, De Haas J T M, Van Eijk C W E 1995 "Non proportionality in the scintillation response and the energy resolution obtainable" IEEE Trans. Nucl. Sc., 42, 2190-2202

Dromain C, Balleyguier C, Muller S, Mathieu M-R, Rochard F, Opolon P and Sigal R 2006 "Evaluation of tumour angiogenesis of breast carcinoma using contrast-enhanced digital mammography" AJR 187, 528-537

Ducote J L, Xu T and Molloi S 2007 "Dual energy cardiac imaging: an image quality and dose comparison for a flat-panel detector and x-ray image intensifier" Phys. Med. Biol. 52, 183-196

El-Mohri Y, Antonuk L A, Zhao Q, Wang Y and Li Y 2006 "Performance of high fill factor, indirect detection prototype flat-panel imager for mammography "Med. Phys. 34, 315-327

Ergun D L, Mistretta C A, Brown D E, Bystrianyk R T, Sze W K, Kelcz F and Naidich D P 1990 "Single exposure dual-energy computed radiography: improved detection and processing" Radiol. 174, 243-249

Fahrig R and Yaffe M J 1994 "Optimization of spectral shape in digital mammography: dependence on anode material, breast thickness, and lesion type" Med. Phys. 21, 1473-1481

Folkman J and Klagsbrun M 1987 "Angiogenic factors" Science 235, 442-447

Folkman J, Watson K and Hanahan D 1989 "Induction of angiogenesis during the transition from hyperplasia to neoplasia" Nature 339, 58-61

Fossum E R 1997 "CMOS Image Sensors: Electronic Camera-On-A-Chip" IEEE. Trans. Elect. Dev. 44, 1689-1698

Fowler B, Godfrey M D and Mims S 2006 "Noise reduction in capacitive sensors" IEEE Circ. and Syst. I 53, 1658-1669

Fujita H, Tsai D Y, Itoch T, Doi K, Morishita J, Ueba K, and Ohtsuka A 1992 "A simple method for determining the modulation transfer function in digital radiology" IEEE Trans. Med. Imag. 11, 34-39

Granfors P G and Aufrichting R 2000 "Perfromance of a 41X41–cm2 amorphous silicon flat panel x-ray detector for radiographic imaging applications" Med. Phys. 27, 1324-1331

Hamamatsu, 1996. "FOS (Fiber Optic Plate with scintillator) for Digital x-ray Imaging" Technical Information. http://www.hamamatsu.com

Holl I, Lorenz E and Mageras G 1988 "A measurement of the light yield of common inorganic scintillators" IEEE Trans. Nucl. Sci. 35, 108-109

Huda W, Sajewicz A M, Ogden K M and Dance D R 2003 "Experimental investigation of the dose and image quality characteristics of a digital mammography system" Med. Phys. 30, 442-448

Janesick J 2002 "Lux transfer: Complementary metal oxide semiconductors versus charge-coupled devices" J. Opt. Eng. 41, 1203-1215

Janesick J and Putnam G 2003 "Development and applications of high-performance CCD and CMOS imaging arrays" Ann. Rev. Nucl. Part. Sci. 53, 263-300

Janesick J, Andrews J T and Elliot T 2006 "Fundamental performance differences between CMOS and CCD imagers; part I" SPIE proc. 6276

Janesick J 2001 *Scientific Charge-Coupled Devices* (SPIE Press, Bellingham, Washington)

Jee K-W, Antonuk L A, El-Mohri Y and Zhao Q 2003 "System performance of a prototype flat-panel imager operated under mammographic conditions" Med. Phys. 30, 1874-1890

Jing T, Cho G, Drewery J, Fujieda I, Kaplan S N, Mireshghi A, Perez-Mendez V and Wildermuth D 1992 "Enhanced Columnar structure in CsI by substrate patterning" IEEE trans. Nucl Sci. 39, 1195-1198

Jing Z, Huda W and Walker J K 1998 "Scattered radiation in scanning slot mammography" Med. Phys. 25, 1111-1117

Johns H E and Canningham J R 1983 *The Physics of Radiology*, Charles C Thomas, Springfield, IL

Johns P C and Yaffe M J 1987 "X-ray characterisation of normal and neoplastic breast tissues" Phys. Med. Biol. 32, 675-695

Johns P C and Jaffe M J 1985 "Theoretical optimization of dual energy imaging with application to mammography" Med. Phys. 12, 289-296

Jong R A, Yaffe M J, Skarpathiotakis M, Shumak R S, Danjoux N M, Guanesekara A and Plewes D B 2003 "Contrast enhanced digital mammography: initial clinical experience" Radiology 228, 842-850

Kappadath S C and Show C C 2005 "Dual energy digital mammography for calcification imaging: scatter and nonuniformity corrections" Med. Phys. 32, 3395-3408

Kappadath S C and Show C C 2003 "Dual energy digital mammography: calibration and inverse-mapping techniques to estimate calcification thickness and glandular-tissue ratio" Med. Phys. 30, 1110-1117

Kappadath S C and Show C C 2004 "Quantitative evaluation of dual-energy digital mammography for calcification imaging" Phys. Med. Biol. 49, 2563-2576

Kelcz F M, Mistretta C A and Riederer S J 1977 "Spectral considerations for absorption edge fluoroscopy" Med. Phys. 4, 26-35

Kleinfelder S, Lim S, Liu X and El Gamal A 2001 "A 10000 frames/s CMOS digital pixel sensor," IEEE J. Solid-State Circ. 36, 2049–2060

Krymski A I, Bock N E, Tu N, Van Blerkom D and Fossum E R 2003 "A high speed, 240-framess 4.1-Mpixel CMOS sensor" IEEE. Trans. Elect. Dev. 50, 130-135

Kuhl C K and Schild H H 2000 "Dynamic image interpretation of MRI of the Brest" J. Magn Reson. Imag. 12, 965-974

Kuhl C K, Schmutzler R K, Leutner C C, Kempe A, Wardelmann E, Hocke A, Maringa M, Pfeifer U, Krebs D and Schild H H 2000 "Breast MR Imaging Screening in 192 Women Proved or Suspected to Be Carriers of a Breast Cancer Susceptibility Gene: Preliminary Results" Radiology 215, 267-279

Lehman L A, Alvarez R E, Mascovski A and Brody W R 1981 "Generalized image combinations in dual kVp digital radiography" Med. Phys. 29, 1739-1751

Lemacks M R, Kappadath S C, Show C C, Liu X and Whitman G J 2002 "A dual-energy subtraction technique for microcalcification imaging in digital mammography- A signal-to-noise analysis". Med. Phys. 29, 1739-1751

Lewin J M, D'Orsi C J, Hendrick R `E, Moss L J, Isaacs P K, Karellas A and Cutter G R 2002 "Clinical comparison of full field digital mammography and screen-mammography for detection of breast cancer" AJR 179, 671-677

Lewin J M, Isaacs P K, Vance V and Larke F J 2003 "Dual-energy contrast-enhanced digital subtraction mammography: feasibility" Radiology 229, 261-268,

Lulé T, Benthien S, Keller H, Mutze F, Rieve P, Seibel K, Sommer M and Bohn M 2000 "Sensitivity of CMOS Based Imagers and Scaling Perspectives" IEEE. Trans. Elect. Dev. 47, 2110-2122

Maidment A D, Fahrig R and Yaffe M J 1993 "Dynamic range requirements in digital mammography" Med. Phys. 20, 1621-1633

Marshall N W 2006 "A comparison between objective and subjective image quality measurements for a full field digital mammography system" " Phys. Med. Biol. 51, 2441-2463

Meyer P, Buffard E, Mertz L, Kennel C, Constantinesco A and Siffert P 2004 "Evaluation of the use of six diagnostic X-ray spectra computer codes" BJR, 77, 224-230

Meynants G, Dietrickx B, Alaerts A, Uwaerts D, Cos S, Scheffer D and Noble S 2003 "A 35 mm 13.89 million pixel CMOS active pixel image sensor" IEEE Workshop on CCD and AIS

Miles K A 2003 " Perfusion CT: a worthwhile enhancement? BJR 76, 220-231

Molloi S Y and Mistretta C A 1998 "Scatter-glare corrections in dual energy fluoroscopy" Med. Phys. 15, 289-297

Moszynsky M, Kapusta M, Mayhugh M, Wolski D and Flyckt S O 1997 "Absolute light output of scintillators" IEEE Trans. Nucl. Sc. 44, 1052-1061

Mulato M, Ready S, Van Schuylenbergh K, Lu J P and Street R A 2001 "Crosstalk and lateral conduction effects in continuous-sensor amorphous silicon imagers" J. Apl. Phys. 89, 8193-8201

Nagarkar V V, Gaysinskiy V,Ovechkina E E, Miller S R, Brecher C, Lempicki A and Squillante M R 2006 "Suppresion of afterglow in CsI (Tl) cy codoping with Eu2+:Fabrication of microcolumnar films for high-resolution high-speed imaging" presented at IEEE NSS-MIC conference

Nowotny . and Hvfer A 1985 "Ein Program fur die Berechung von diagnostischen Roentgnespektren. Fortschr Roentegenstr 142, 685-689

Nunes F L S, Schiabel H and Benattic R 2002 "Contrast enhancement in dense breast images using the modulation transfer function" Med. Phys. 29, 2925-2936

Omar W S, Eissa S and Moustafa H 1997 "Role of thalium-201 chloride and Tc 99m methoxyl-isobutyl-isonitrite (sesta MIBI) in evaluation of breast masses: correlation with the immunohistochemical; characteristic parameters (Ki-67, PCNA, Bcl and angiogenesis" Anticancer Res. 17, 1639-1644

Pain B, Yang G, Cunningham T J, Wrigley C and Hancock B 2003 "An Enhanced-Performance CMOS imager with a Flushed-Reset Photodiode Pixel" IEEE Trans. Elect. Dev. 50, 48-55

Pediconi F, Catalano C, Roseli A, Padula S, Altomari F., Moriconi E, Pronio A-M, Kirchin M A and Passarelio R 2007 "Contrast-Enhanced MR mammography for evaluation of the contralateral breast in patient diagnosed unilateral breast cancer of high-risk lesions" Radiology, 243, 670-680

Pisano E D, Gatsonis C, Hendrick E, Yaffe M J, Baum J K, Acharyya S, Conant E F, Fajardo L L, Bassett L, D'Orsi C, Jong R and Rebner M 2005 "Diagnostic Performance of Digital versus Film Mammography for Breast-Cancer Screening" N. Engl. J. Med. 353, 1773-1783

Pisano E T and Yaffe M J 2005 "Digital Mammography" Radiology 234, 353-362

Prydderch M L, Waltham N J, Turchetta R, French M J, Holt R, Marshall A, Burt D, Bell R, Pool P, Eyles C and Mapson-Menard H 2003 "A 512 x 512 CMOS monolithic active pixel sensor with integrated ADCs for space science" Nucl. Instrum. Meth. A 512, 358-367

Rabbani M, Shaw R and Van Metter R 1987 "Detective quantum efficiency of imaging systems with amplifying and scattering mechanisms" J. Opt. Soc. Am A 4, 895-901

Riederer S J, Kruger R A and Misetretta C A 1981 "Limitations to iodine isolation using a dual beam non k-edge approach" Med. Phys. 8, 54-61

Rose A 1953 "Quantum and noise limitations of the visual process" J. Opt. Soc. Am. 39, 327

Ruschin M, Timberg P, Bath M, Hemdal B, Svahn T, Saunders R S, Samei E, Andersson I, Mattsson S, Chakrborty D P and Tingberg A 2007 "Dose dependence of mass and microcalcification detection in digital mammography: free response human observer" Med. Phys. 34, 400-407

Sabel M, and Aichinger H 1996 "Review: Recent developments in breast imaging" Phys. Med. Biol. 41, 315-368

Said E S, Chan T Y, Fossum E R, Tsai R H, Spagnuolo R, Deily J, Byers Jr. W B and Peden J C 2001 "Design and characterization of ionizing radiation-tolerant CMOS

APS image sensors up to 30 Mrd (Si) total dose: Part 1" IEEE Trans. Nucl. Sci. 48, 1796-1806

Samei E 2003 "Image quality in two phosphor-based flat panel digital radiographic detectors" Med. Phys. 30, 1747-1757

Samei E and Flynn M J 2002 "An experimental comparison of detector performance for computed radiography" Med. Phys. 29, 447-459

Samei E, Flynn M J and Reinmann D A 1998 "A method for measuring the presampled MTF of digital radiographic systems using an edge test device" Med. Phys. 25, 102-113

Samei E, Ranger N, Dobbins J and Chen Y 2006 "Intercomparison of methods for image quality characterisation. I. Modulation transfer function," *Med. Phys.* 33, 1454–1465,

Saunders R S, Samei E, Jesneck J L and Lo J Y 2005 "Physical characterization of a prototype selenium-based full field digital mammography detector" Med. Phys. 32, 588-599

Scheffer D 2007 "Wafer scale active pixels CMOS image sensor for generic X-ray radiology" SPIE 65100

Schotanus P, Kamermans R and Dorenbos P 1990. "Scintillation characteristics of pure and T1-doped CsI crystals" IEEE Trans Nucl. Sci. 37, 177-182

Shaw C-G and Plewes D B 1987 "Effects of scatter radiation and veiling glare in dual-energy tissue-bone imaging: a theoretical analysis" Med. Phys. 14, 956-967

Shcherback I, Danov T and Yadid-Pecht O 2004 "A Comprehensive CMOS APS Crosstalk Study: Photoresponse Model, Technology, and Design Trends" IEEE. Trans. Electron Devices, 51, 2033-2041

Siewerdsen J H and Jaffray D A 1999 "A ghost story: spatio-temporal response characteristics of an indirect detection flat-panel imager" Med. Phys. 26, 1624-1641

Siewerdsen J H, Antonuk L A, El-Mohri Y, Huang W. Boudry J M and Cunningham I A 1997 "Empirical and theoretical investigation of the noise performance of indirect detection, active matrix flat-panel imagers (APFPIs) for diagnostic radiology" Med. Phys. 24, 71-89

Siewerdsen J H, Antonuk L E, El-Mohri Y, Yorkston J, Huang W and Cunningham I A 1998 "Signal, noise power spectrum, and detective quantum efficiency of indirect-detection flat-panel imagers for diagnostic radiology" Med. Phys. 25, 614-628

Skarpathiotakis M, Yaffe M J, Bloomquist A. K, Rico D, muller S, Rick A and Jeunehomme F 2002 "Development of contrast digital mammography" Med Phys. 29, 2419-2426

Snoeren P R and Karassemeijer D 2006 "Thickness correction of mammographic images by means of a global parameter model of the compressed breast" IEEE Trans. Med. Imag. 23, 799-806

Soo L J, Hornsey R I and Renshaw D 2003 "Analysis of CMOS Photodiodes—Part II: Lateral Photoresponse" IEEE. Trans. Electron Devices, 50, 1239-1245

Suryanarayanan S, Karellas A, Vedantham S and Onishi S K 2005 "High-resolution imager for digital mammography: physical characterization of a prototype sensor" Phys. Med. Biol. 50, 3957-3969

Swank R K 1973 "Absorption and noise in x-ray phosphors" J. Appl. Phys. 44, 4199-4203

Tang H, Zhuang T and Wu E X 2001 "Realizations of fast 2-D/3-D image filtering and enhancement" " IEEE Trans. Med. Imag. 20, 132-140

Tian H, Fowler B and El Gamal A 2001 "Analysis of Temporal Noise in CMOS Photodiode Active Pixel Sensor" IEEE Solid-State Circ. 36, 92-101

Trefilova L N, Kudin A M, Kovaleva L V, Zaslavsky B G, Zosim D I and Bondarenko S K 2002 "Concentration dependence of the light yield and energy resolution of NaI:Tl and CsI:Ti crystals excited by gamma, soft X-rays and alpha particles" Nucl. Inst. and Meth. A, 486, 474–481

Turchetta R, Berst J D, Casadei B, Claus G, Colledani C, Dulinski W, Hu Y, Husson D, Le Normand J P, Riester J L, Deptuch G, Goerlach U, Higueret S and Winter M 2001 "A monolithic active pixel sensor for charged particle tracking and imaging using standard VLSI CMOS technology," Nucl. Instrum. Meth. A 458, 677–689

Ullman G, Sandborg M, Dance D R Yaffe M J and Carlsson G A 2005 "A search for optimal X-ray spectra in iodine contrast media mammography" Phys Med. Biol. 50, 3143-3152

Van Eijk C W E 2003 "Inorganic scintillators in medical imaging detectors" Nucl. Inst. and Meth. A, 509, 17–25

Van Eijk C W E 2002 "Topical Review: Inorganic scintillators in medical imaging" Phys. Med. Biol. 47, 85-106

Vedantham S, Karellas A, Suryanarayanan S, Albagli D, Han S, Tkacyzk E J, Landberg C E, Granfors P R, Levis I, D'Orsi C.J and Hendrick R E 2000 "Full breast digital mammography with an amorphous silicon-based flat panel detector: Physical characteristics of a clinical prototype" Med. Phys. 27, 558-566

Velthuis J J, Allport P P, Casse G, Evans A, Turchetta R, Tyndel M and Villani G 2005 "Characterization of active pixel sensors in 0.25μm CMOS" IEEE Trans. Nucl. Sci. 52, 1887-1891

Wagner F C, Macovski A and Nishimura D G 1988 "Dual energy projection imaging: two sampling schemes for the correction of scattered radiation" Med Phys 15, 732-748

Watt C, Ackerman L. V, Shetty P, Burke M, Flynn M J, Grodsinsky C, Fine G and Wilderman S 1985 "Differentiation between benign and malignant disease of the breast using digital subtraction angiography of the breast," Cancer 56, 1287–1292

Weber M J 2002 "Inorganic scintillators: today and tomorrow" J. Lumin. 100, 35-45

Williams M B and Simoni P U 1999 "Analysis of the detective quantum efficiency of a developmental detector for digital mammography" Med. Phys. 26, 2273-2285

Williams M B, Mangiafico P A and Simoni P U 1999 "Noise power spectra of images from digital mammography detectors" Med. Phys. 26, 1279-1293

Wong H. 2000 "Technology and Device Scaling Considerations for CMOS Imagers" IEEE. Trans. Elect. Dev. 47, 2110-2122

Wu T, Stewart A, Stanton M, McCauley T, Phillips W, Kopans D B, Moore R H, Eberhard J W, Opsahl-Ong B, Niklason L and Williams M B 2003 "Tomographic mammography using a limited number of low-dose cone-beam projection images" Med. Phys. 30, 365-380

Yaffe M J and Rowlands J A 1997 "Review: X-ray detectors for digital radiography" Phys. Med. Biol. 42, 1-39

Yaffe M J 2000 "Digital Mammography" Volume 1 Physics and Psychophysics, Chapter 5, edited by J. Beutel, H. L. Kundel, and R. L. Van Metter (SPIE, Bellingham), pp. 79–159,

Yamada T, Ishibashi T, Sato A, Saito M, Saito H, Matsuhashi T and Takahashi S 2003 "Comparison of screen-film and full-field digital mammography: image contrast and lesion characterization" Radiat. Med. 21, 166-171

Yu. T, Sabol J M, Seibert J A, and Boone J 1997 "Scintillating fiber optic screens: A comparison of MTF, light conversion efficiency, and emission angle with Gd_2O_2S:Tb screens" Med. Phys. 24, 279-285

Zhao W and Rowlands J A 1997 "Digital radiology using active matrix readout of amorphous selenium: Theoretical analysis of detective quantum efficiency" Med. Phys. 24, 1819-1833

Zhao W, Ristic G and Rowlands J A 2004 "X-ray imaging performance of structured cesium iodide scintillators" Med. Phys. 31, 2594-2605